Material and Damping Characterization of Discretized Adhesive Tapes in Cantilever Beams undergoing Free and Forced Vibration

Nilma Rosa Barsallo Pacheco

Thesis submitted to the faculty of the Virginia Polytechnic Institute and State University in partial fulfillment of the requirements for the degree of

Master of Science
In
Engineering Mechanics

David A. Dillard Co-Chair
Muhammad R. Hajj Co-Chair
Saad A. Ragab

May 6, 2014
Blacksburg, VA

Keywords:

Damping tapes, Vibrations, Viscoelastic material, Damping ratio, Nonlinear damping

Material and Damping Characterization of Discretized Adhesive Tapes in Cantilever Beams undergoing Free and Forced Vibrations

By

Nilma Rosa Barsallo Pacheco

(ABSTRACT)

The work is focused in investigating the effectiveness of discretized damping tapes applied to a cantilever beam subjected to free and forced vibrations. The work is divided into three main sections. First, we performed material characterization of the viscoelastic (VE) pressure sensitive adhesive layer of the damping tapes. To do so, we designed a novel quad shear specimen to measure shear storage and loss moduli, and tan δ from dynamic mechanical analyzer measurements. Second, the optimal discretization length for different damping tapes was experimentally determined and analytically verified using linear viscoelasticity and basic strength of materials and vibrations principles. These results showed a mean to improve the damping of a structure without increasing the weight of the added damping layer. Third, a nonlinear analysis was performed for cantilever beams with damping layers subjected to parametric excitation. Comparison of the response amplitude of the parametrically excited beam was performed for different discretization lengths, and system identification of the nonlinear parameters was carried out. The effects of large deflections of a beam under parametric excitation were analyzed; large deflections were found to induce localized buckling of the stiff constraining layer of the damping tape that would invalidate some of the assumptions and analytical solutions that do not take such phenomena into account.

Acknowledgements

First, I would like to thank God for blessing me with the opportunity to pursue a Masters degree in such a prestigious university. Without His guidance I would never have been able to accomplish this work. Please keep giving me such challenges because I did not ask for an easy race but for a strong back and mind to handle everyday challenges. I want to extend my gratitude to my family of encouragement and love. Mom and Dad thank you for your advice. To my sisters, Gladys and Amaril, to my brother Alex that always make me laugh even across the hundreds of kilometers between us. To my Henry, who has been there for me during these two years, supporting me and reminding me to keep fighting for my dreams.

I want to thank my advisors, Dr. David Dillard, Dr. Muhammad Hajj and also committee member Dr. Saad Ragab for agreeing to advise my research. Dr. Dillard, your attention and patience during this time has helped me to accomplish this work. With your advice I have improved both my academic and engineering skills. Dr. Hajj, thank you for academic advice and your willingness to help me to improve every day. Dr. Ragab, thank for your advice in critical moments of this journey, and for your patience during classes that helped me to learn so much. I also thank Lisa Smith for being an awesome person to me in this department. You have helped many students to achieve their degrees by guiding us through the endless amounts of logistics and forms to accomplish our academic goals. Also, I would like to thank to my colleagues in the vibrations laboratory, Mohammad Haik and Chris Deny, who helped me during this year to successfully prepare experiments. Thanks to Bruce Orler and Shantanu Ranade for their help with material characterization. Lastly, I offer thanks to the National Secretariat of Science, Technology and Innovation of Panama for their sponsorship that enabled me to pursue this Masters degree and research, and 3M for providing the damping tapes used in this research. All photos by author, 2014.

"Dios, concédeme la serenidad para aceptar las cosas que no puedo cambiar, el valor para cambiar las cosas que puedo cambiar y la Sabiduría para conocer la diferencia."

Table of Contents

List of Figures

List of Tables

List of Symbols

Symbol	Meaning	Units
δ	loss tangent angle of the material	dimensionless or radians
G^*	complex shear modulus of the material	Pascals
G'	storage shear modulus of the material	Pascals
G''	loss shear modulus of the material	Pascals
a_T	thermal shift factor	dimensionless
f	frequency	Hertz
t	thickness of the acrylic layer of the tape	meters or millimeters
w	width of the DMA sample	meters or millimeters
P	load of the DMA	Newtons
Δ_{DMA}	displacement recorded with the DMA	meters or millimeters
n_{layers}	number of layers in the DMA sample	dimensionless
$\hat{\gamma} = \lvert\gamma^*\rvert$	amplitude of complex shear strain	dimensionless
$\hat{\tau} = \lvert\tau^*\rvert$	amplitude of complex shear stress	Pascals
E_2	modulus of elasticity of the constraining layer	Pascals

t_1	thickness of the PSA layer	meters or millimeters
t_2	thickness of the constraining layer	meters or millimeters
SL	characteristic shear lag distance	meters or millimeters
W_{dis}	work dissipated per cycle per unit width of geometry	Newtons meter cycle^{-1}
η_d	loss coefficient	nondimensional
η_S	loss coefficient of the beam with damping layers	nondimensional
η_B	loss coefficient of the bare beam	nondimensional
L_a	element length of the constraining layer	meters or millimeters
ε_0^*	uniform time varying axial strain at the interface	nondimensional
u_0^*	time varying displacement at the interface of the basic structure and the viscoelastic layer in the x direction.	meters
k	stiffness of the elastic foundation	Newtons meter^{-2}
N	axial load	Newtons
N_{cr}	critical axial buckling load	Newtons
Δ	logarithmic decrement	nondimensional
ζ	damping ratio	nondimensional
ω_n	undamped natural frequency	Hertz
μ_1	linear damping	Hertz
l	total length of beams	meters or millimeters

L	total length of surface treatments	meters or millimeters
t_b	thickness of beams	meters or millimeters
r	length ratio	nondimensional
Ω	excitation frequency	Hertz
a	response amplitude of parametric excitation	millistrain
f * in Chapter 6	forcing amplitude during parametric excitation	meters seconds^{-2}
μ_2	nonlinear damping	millistrain^{-1}
α_3	cubic nonlinearity	millistrain^{-2} seconds^{-2}
η_2	parametric forcing parameter	millistrain^{-1}

Chapter 1 Thesis Overview

A brief introduction is made about the basic concepts used in this work to study the energy dissipation of structural elements with equipped discretized damping layers. The chapter starts with an overview of the problem of vibration control in structural elements. This is followed by an introduction of the concept of damping tapes including, configuration, history, and applications, along with the concept of discretized constrained damping layers. The nonlinear vibrations of a cantilever beams and the buckling of a thin beam on an elastic foundation are also introduced.

1.1 Background

Vibration problems are of significant concern in many industrial systems nowadays. Often, vibrations are an undesirable problem and the goal is to reduce the amplitude of such vibrations to non-harmful levels. Failures due to excessive vibration are often expensive and can even be life threatening. The costs of preventive solutions are often less than the damage result, including the possibility of catastrophic failures. Therefore, an understanding of vibrations and mitigation strategies is very important for practicing engineers.

1.1.1 Damping tapes as vibration control solutions

Commonly used damping control mechanisms include viscoelastic (VE) pads/layers that help decrease harmful vibrations of critical components. The characteristic that makes these materials appropriate for such applications is the fact that VE materials under most loading conditions will dissipate energy through viscous dissipation and resulting heating of the viscoelastic material. This energy dissipation is important when the VE material undergoes steady state oscillations (Dillard, 2013). Therefore, VE materials are can be used as damping methods.

1.1.2 Damping tape configurations

Available forms of damping tapes are often composed of three main components, as shown in Figure 1.1:

1. Backing layer: a stiff constraining layer on the top of the adhesive layer to enhance the energy dissipation. Commercially available damping tapes often have a dead soft aluminum backing material to enable them to be conformed to nonplanar surfaces.
2. Pressure sensitive adhesive (PSA) layer: the viscoelastic material used as the dissipating layer.
3. Liner layer: a siliconized paper layer is often used to prevent blocking during storage, and it is always removed prior to application of the tape.

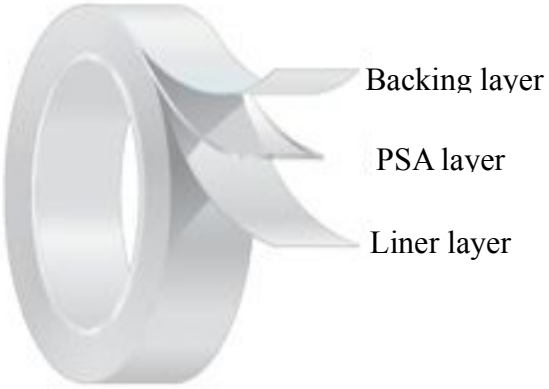

Figure 1.1: Damping tape configuration. Source: 3M. "3M Metal Foil Tapes". edited by 3M, 2012. URL: http://multimedia.3m.com/mws/mediawebserver?mwsId=66666UgxGCuNyXTtMxM_58TtEVtQEcuZgVs6EVs6E666666--&fn=70-0709-5390-9%20LR_R4.pdf Used under fair use, 2014.

1.1.3 Historical background of damping tapes.

One of the most typical solutions for vibration damping is to simply bond VE materials to the structure. This type of damping mechanism has been considered since the 1950s for the purpose of noise reduction in diverse industrial applications. Although the literature has included this

solution since the 1950s, the fact that covering metal sheets with rubberlike materials reduces the noise associated with common loads was recognized earlier (Ungar, 2000).

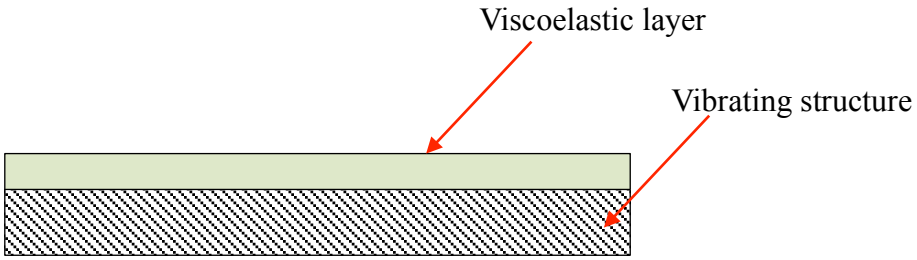

Figure 1.2: Free damping layer.

The idea of covering vibrating structures with VE materials to damp such vibrations to reduce noise and avoid dangerous oscillatory loads soon became popular, and so researchers tried to optimize such layers because of their relatively low cost and wide range of applications. To this end, one of the configurations considered was a constrained damping layer.

In 1959, Kerwin investigated the effectiveness of the constrained damping layers, and called this configuration a "damping tape" or passive constrained damping layer (PCDL). This configuration consisted of a VE layer sandwiched between a stiff elastic material and the vibrating structure, thereby increasing the energy dissipation of the damping treatment. This damping tape was observed to be more effective than the free damping layer because of the shear deformation induced within the VE layer (Kerwin, 1959). Ross, Ungar and Kerwin published analytical models to predict the damping of an infinite long sandwich configuration where the damping material was fully constrained (Ungar, Ross, & Kerwin, 1960). DiTaranto addressed a similar specimen but considering a finite length beam for different end conditions (DiTaranto, 1965). Figure 1.3 illustrates a "damping tape" bonded to the base structure.

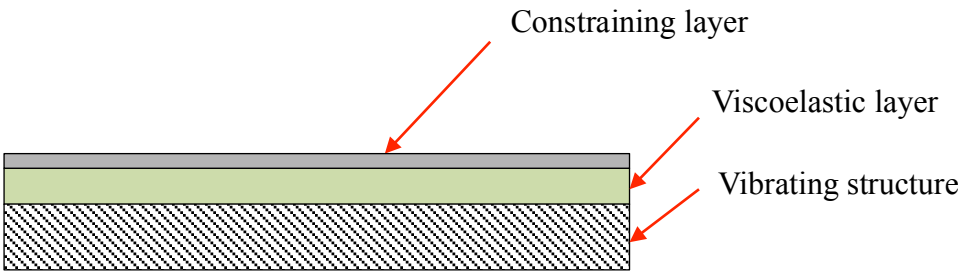

Figure 1.3: Constrained damping layer.

In 1960, Parfitt and Lambeth compared the performance of free and constrained VE damping layers. They showed that the performance of a constrained damping layer is better than a free VE layer. Yet, one of their most important findings was what they referred to as wrinkles in the damping tapes, which affected the energy dissipation. They expected that not having perfectly straight constraining layers would decrease the "extensional stiffness" of the backing layer, on which the enhanced damping depended. They observed instead that the presence of buckling actually improved the damping capabilities of the damping layer (Parfitt & Lambeth, 1960). In 1962, Parfitt found that by discretizing the constrained damping layer, the damping capabilities could be improved (Parfitt, 1962). This result was the beginning of a broad and significant field of research because it showed that discretized damping tapes might improve damping without adding more weight to the structure or any additional complicated mechanism.

Later, in 1970, Plunkett and Lee considered the case of finite-length surface treatment of a well-known engineering structure, a vibrating cantilever beam with cyclic loadings and showed the enhancement of the loss coefficient of a discretized constrained damping layer as shown in Figure 1.4 (Plunkett & Lee, 1970). In the current work, we have focused on studying the effectiveness of this discretized configuration.

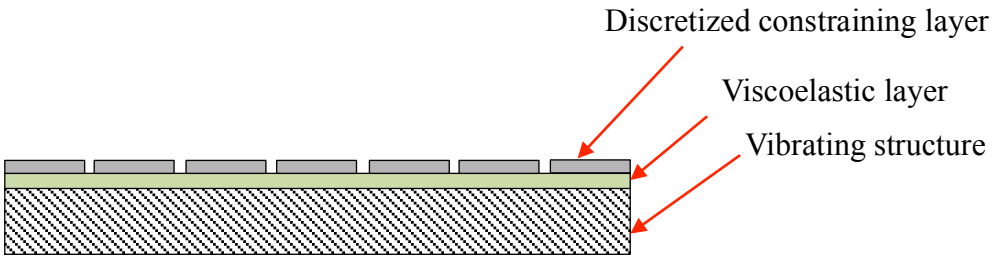

Figure 1.4: Discretized damping tape.

1.1.4 Applications of damping tapes

Nowadays, continuous damping layers are being used in several industries to reduce undesirable noise and vibrations of structural and mechanical elements. Examples of such applications are illustrated in Figure 1.5. Damping tapes can be used to damp undesirable noise of domestic appliances such a washing machines by bonding a continuous damping tape layer to appropriate structural elements. In the automotive industry damping tapes are used to reduce noise and vibrations of a cars' body. Damping tapes are also used to reduce vibrations in aeronautical structural elements.

(a)

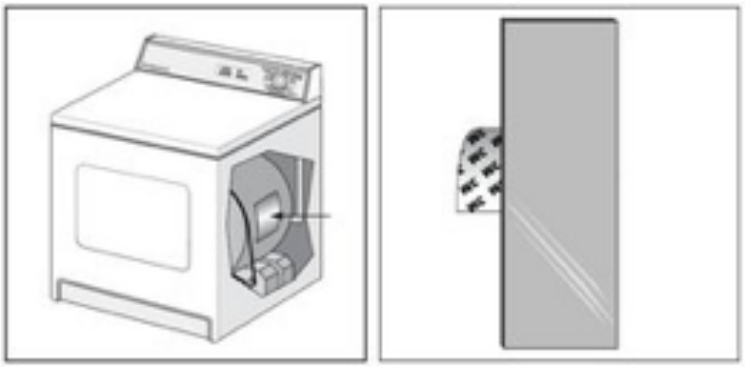

(b)

(c)

Figure 1.5: Applications of damping tapes on: a) domestic appliances. b) automotive industry. c) aeronautical industry. Source: 3M "Damping Tapes Applications" 3M catalog, 2012. URL: http://solutions.3m.com/wps/portal/3M/en_US/Adhesives/Tapes/Applications/~/Industrial-Adhesives-Tapes-Applications/Damping?N=5865944&rt=r3 Used under fair use, 2014.

1.2 Project overview

1.2.1 Motivation for the project

In spite of the well-known benefits of discretizing constrained layer damping tapes, current usage often involves the use of continuous damping layers applied to vibrating structures. This research is interested in reviewing the benefits of discretization and investigates other effects of alternative embodiments to enhance the performance of damping tapes.

1.2.2 Objectives of the project

The overall goal of the research is to verify the effectiveness of discretized damping layers compared to continuous damping layers applied to cantilever beams. With this method, our goal is to observe the reduction of vibration amplitudes in cantilever beams undergoing free and forced vibrations. To this end, we divided our goal into the following specific objectives:

1. To perform a dynamic mechanical analysis and determine material properties of viscoelastic layers of the damping tapes. This is to predict the performance of the damping material in effectively reducing vibration of the tested cantilever beams. The target properties of such material characterization are:
    a. Storage modulus.
    b. Loss modulus.
    c. tan δ.
2. To verify the effect of discretized damping layer on the damping ratio of cantilever beams considering:
    a. Different types of damping tapes.
    b. Different materials and thickness beams.
    c. Different surface treatments (fully vs. partially applied)
3. To investigate and compare the nonlinear response of cantilever beams with and without surface treatment as well as different discretization damping layer lengths by considering the following aspects:

a. Different driving amplitudes of the excitation to observe the damping of amplitude of the response in cantilever beams.
b. Identification of nonlinear parameters such as nonlinear damping, cubic nonlinearities and forcing parameters for the beams, considering different discretization lengths of the damping tapes applied to the beams.

Our aim is to observe any effect of the tape on nonlinear parameters that govern the response of cantilever beams undergoing parametric excitation. So far, the model used to perform the identification was for identifying nonlinear parameter of beams without surface treatments. In this work one of our objectives is to extend the use of the considered model to beams with thin surface treatments. Nonlinear parameters have shown to be necessary to model the motion of these beams when the amplitudes of the vibration are large enough. We will observe which of the identified parameters affect the dynamic of the beam the most when the damping layers are added to the system.

1.3 Methodology of the project

The methodology used to pursue the goals of this research is illustrated in Figure 1.6. This figure includes the sections and outcomes expected of each main component of the research methodology.

1.3.1 Material characterization

To characterize the VE layer we reviewed literature on VE experimental techniques in order to determine an appropriate experimental procedure to obtain shear properties of the polymer. Once an appropriate method was chosen, we designed experimental samples to fit the experimental procedure that was used in this research. To finish this section, experiments were conducted to obtain material properties such as: shear storage modulus, shear loss modulus, and tan δ, all as functions of temperature and frequency.

1.3.2 Linear analysis

For this component of the research the first step was to obtain analytical equations to predict the energy dissipation of discretized damping layers. To this end, the considered concepts were: shear lag model (Volkersen, 1938), viscoelasticity concepts (Dillard, 2013) (Brinson & Brinson, 2007), and vibrations concepts (Meirovitch, 2010). To complete the linear study an experimental part were included. With these experiments we obtained damping ratios for several beams with different discretization length. This section of the work relied heavily on the Plunkett and Lee analysis (Plunkett & Lee, 1970).

1.3.3 Nonlinear analysis

As a complementary section of this research, a nonlinear analysis was performed to analyze the performance of the damping tapes under high amplitudes of vibrations. To this end, we performed experiments in which cantilever beams were parametrically excited at different excitation amplitudes and data was recorded for each case. With the experimental measurements, nonlinear parametric identification was made. From this identification we obtained values for the nonlinear damping, geometric nonlinearity, and forcing parameter for different discretization lengths, and compared with identified values for the bare beam.

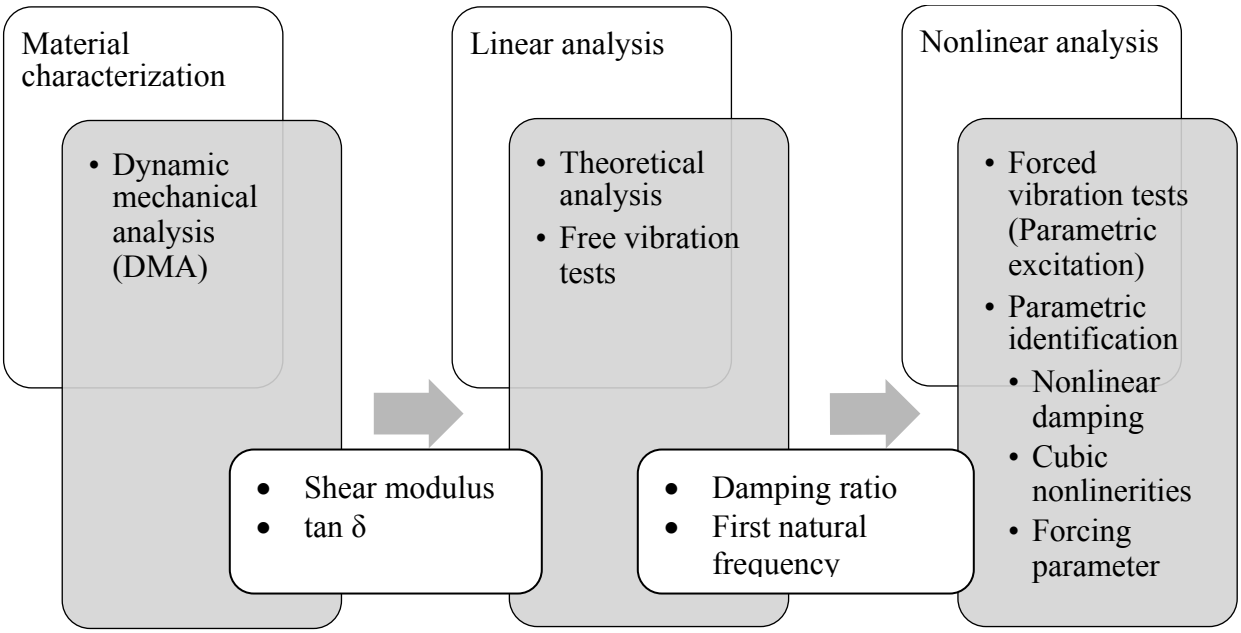

Figure 1.6: Schematic of the research methodology.

1.4 Thesis outline

Following the introduction presented in Chapter 1, the remainder of the thesis is organized as follows:

In Chapter 2, we present results from VE material characterization using dynamic mechanical analysis (DMA). Because the damping layers that were used for the analysis are commercial damping tapes, the characterization of the viscoelastic material is not straightforward because the VE PSA layer of the damping tapes is bonded to the backing material and cannot be separated. Hence, we designed specimens for testing in the DMA using multiple layers of the constrained damping tapes. This geometry allowed us to characterize the VE material within the damping tapes. Estimates of the storage and loss shear modulus, and tan δ were obtained from the DMA. Finally, we obtained master curves for shear storage and loss moduli as well as tan δ.

Chapter 3 presents a mechanics background for the energy dissipation mechanism within damping layers constrained by stiff backing materials. We based this analysis on a linear viscoelastic analysis and basic vibrations principles to set the theoretical pillars for comparing

the experimental results obtained in the following sections. This chapter also contains additional tools to analyze the buckling of the backing layer of the damping tape when the beam is subjected to large deflections.

In Chapter 4, we compiled results obtained from the linear analysis of the cantilever beams tested. We completed a study of the effect of the constraining layer length on damping ratio of the tested beams. Experimental data are shown and analyzed in this chapter. To collect the required data we used the available hardware configuration and software programing in LabVIEW. We used the experimental values of tan δ obtained from the DMA test performed in Chapter 2, and calculated theoretical values for the loss factor of the constrained viscoelastic layers. We then compared these results with those obtained from the experiments for several damping tapes and damping layer discretization lengths. Numerical integrations were run in Matlab® to compute the mode shapes of the structure and compare experimental results.

One of the issues that we wanted to investigate is any nonlinear damping effect of the constrained damping layer on cantilever beams undergoing large deflections. For this purpose we present in Chapter 5 a nonlinear analysis of cantilever beams. The samples were tested under parametric excitation, about twice their natural frequency, to estimate the system's nonlinearities. This was done for different discretization lengths of the constraining layers as in Chapter 4. In this section we analyzed the effect of the large deflection experienced by the beam due to the parametric excitation, including the buckling of the backing material. Again, we used the available hardware configuration and software programing in LabVIEW and ran numerical integrations in Matlab® to validate the nonlinear equation of motion.

Chapter 6, complements the nonlinear analysis by investigating the effect of large deflections to the damping tapes geometry. Here, the onset of buckling effects as a critical bending strain is reached was studied.

Finally, Chapter 7 includes our conclusions of the linear and nonlinear analysis of cantilever beams with discretized damping layers, and recommendations for future work.

Chapter 2 Experimental Characterization of Viscoelastic Material Properties

2.1 Methodology to characterize viscoelastic material properties

In this chapter, we present an overview of the viscoelastic material characteristics. This section contains basic considerations of mechanical properties and characterization techniques. The damping tapes used for this thesis were tested using multiple layered samples. We present details of such specimen including geometry, composition and construction. Dynamic Mechanical Analysis (DMA) settings used with this type of sample and the analytical equations used to derive the shear storage and loss moduli from the raw DMA data are listed. With this technique we were able accomplish the overall goal of this chapter: to complete an analysis and obtain master curves for the viscoelastic materials found in the damping tapes.

2.2 Properties of viscoelastic materials

To characterize the pressure sensitive adhesive present in the damping tapes, we will assume linear viscoelastic behavior. Figure 2.1 shows the response due to a harmonic stress of an elastic material, a viscous material and a viscoelastic material to illustrate the differences of each response. In Figure 2.1a, we observe the response of a perfectly elastic material. The angle δ represents the phase between the excitation and the response for the elastic linear material, $\delta = 0°$. Figure 2.1b, shows the response of a viscous material with the phase angle $\delta = 90°$ and Figure 2.1c represents a viscoelastic material and the phase angle δ may assume values between 0° and 90°. So we observe that there is a lag between the excitation stress and the strain response.

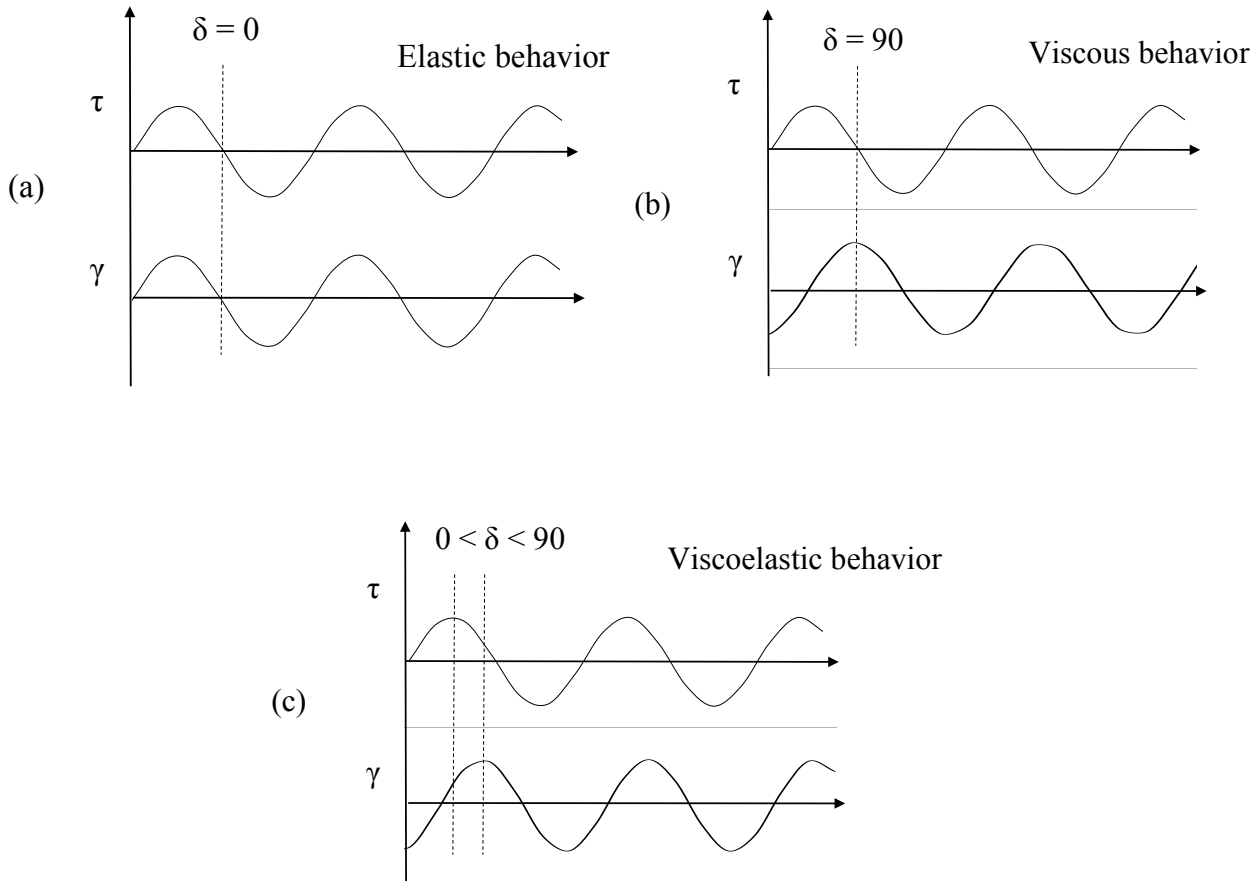

Figure 2.1: Response to harmonic excitation of: a) elastic material b) viscous material. c) viscoelastic material.

Following the analysis of material properties of damping layers, Figure 2.1 considers the analysis of viscoelastic materials undergoing a stress input resulting in a strain output. On the other hand, Figure 2.2a considers the response of linear viscoelastic materials under cyclic strain input resulting in stress output. Figure 2.2b shows the complex notation used to describe properties of this type of material. Linear viscoelastic behavior can be defined by the following shear properties (Dillard, 2013) (Brinson & Brinson, 2007):

1. Storage shear modulus: G', from Figure 2.2b. The amplitude of the storage shear modulus represents the stiffness which is in-phase with the strain, and is related to the energy stored and recovered per cycle:

$$G' = \frac{\hat{\tau}}{\hat{\gamma}} \cos\delta \tag{2.1}$$

2. Loss shear modulus: G'', from Figure 2.2b. The loss modulus represents the stiffness of the stress that leads the strain by 90°. G'' is related to the mechanical energy converted to heat through viscous frictional forces:

$$G'' = \frac{\hat{\tau}}{\hat{\gamma}} \sin\delta \tag{2.2}$$

3. Tan δ: Is the tangent of the loss angle of the material. Defined as the ratio of the loss modulus, G'' to the storage modulus, G':

$$\tan\delta = \frac{G''}{G'} \tag{2.3}$$

For the case of a Voigt element (spring and dashpot in parallel), these three properties can be related as follows:

$$\begin{aligned} G^*(i\omega) &= G + i\omega\eta \\ G' &= G \\ G'' &= \omega\eta \\ \tan\delta &= \frac{\omega\eta}{G} \end{aligned} \tag{2.4}$$

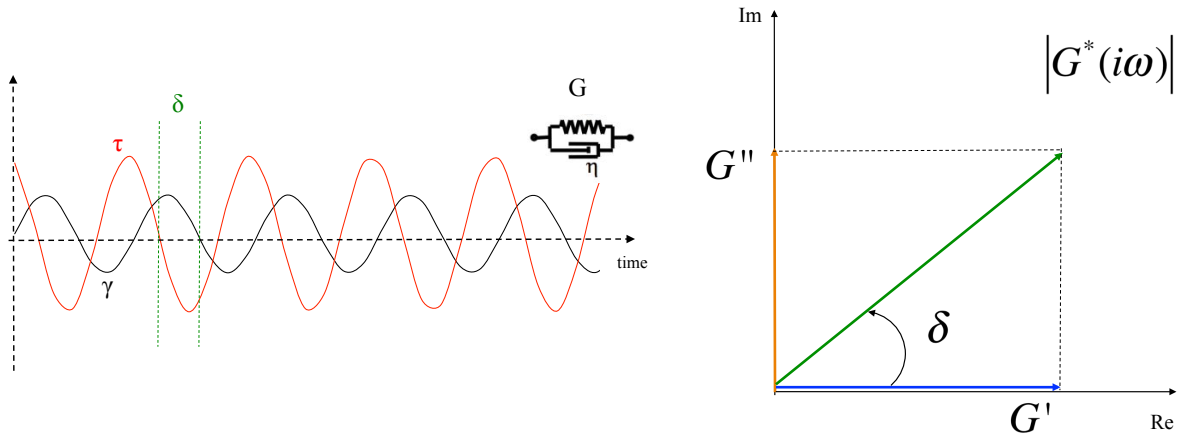

(a) (b)

Figure 2.2: Response of a viscoelastic material, complex notation results in: a) lagging strain response in time domain. b) decomposition of stress into in-phase and out-of-phase components.

2.2.1 Frequency and temperature dependence of linear viscoelastic materials

Although the response of perfectly elastic solids is independent of frequency, this is not the case for viscoelastic materials, where the viscoelastic properties in equation (2.4) are all strongly dependent on frequency. At a fixed temperature the behavior of the storage and loss moduli and tan δ at different frequencies is schematically illustrated in Figure 2.3. Notice that the frequency in Figure 2.3 is defined as:

$$f = \frac{\omega}{2\pi} \qquad (2.5)$$

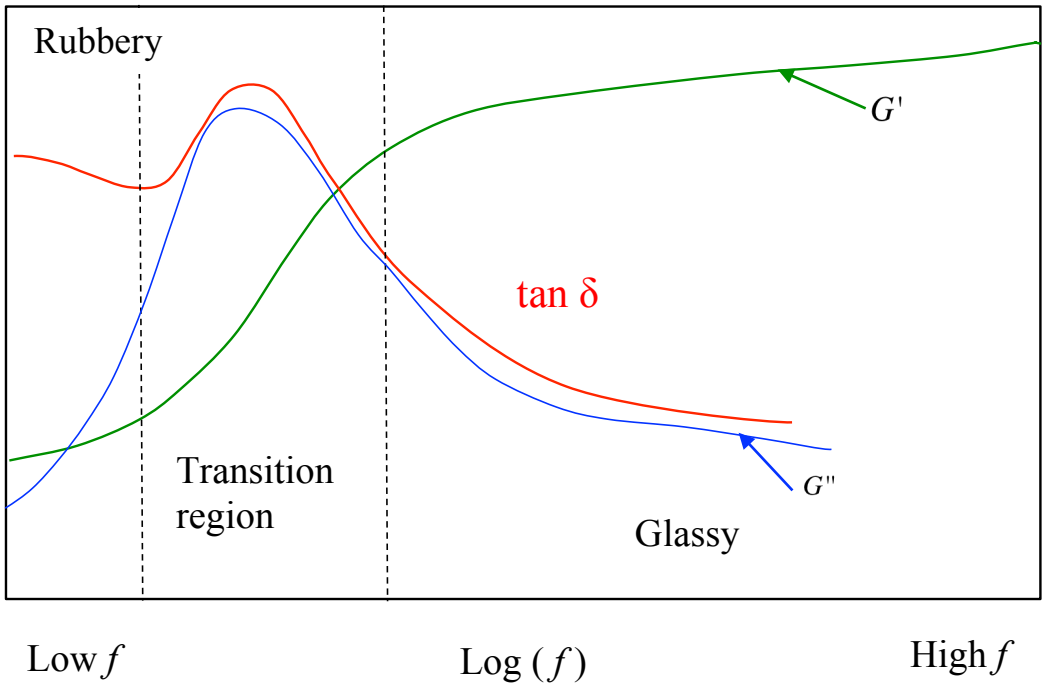

Figure 2.3: Schematic illustration of the effect of the frequency, f on the storage and loss moduli and tan δ behavior at constant temperature.

Temperature is another variable to take into account when characterizing VE materials. The behavior of G', G'' and tan δ changes with temperature in a similar manner to what happens at different excitation frequencies. This temperature and frequency dependency adds complexities to the characterization of viscoelastic materials and their applications to industrial design. One can observe from Figure 2.4 that for high temperatures, the behavior of the VE properties is similar to that observed when we excite the material at lower frequencies.

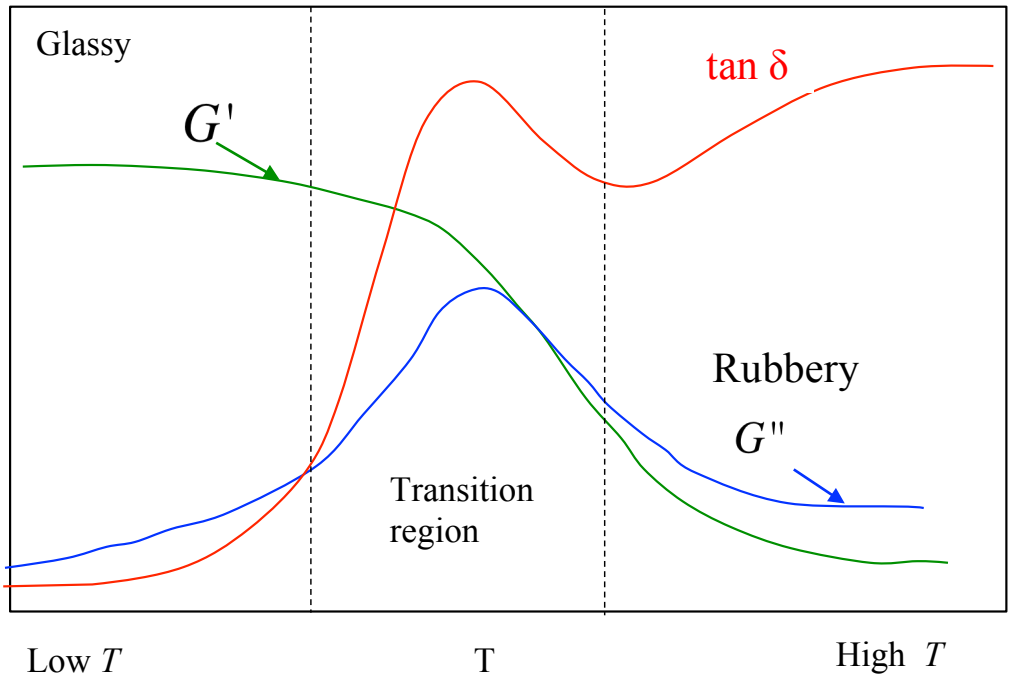

Figure 2.4: Schematic illustration of the effect of the temperature on the storage and loss moduli and tan δ behavior at constant frequency.

From Figure 2.3 and Figure 2.4, we can observe that the behavior of G', G'' and tan δ is distributed in three main regions:

1. Glassy Region: The polymer acts glassy at low temperatures or high frequencies. The storage modulus is high with respect to the loss modulus.
2. Transition Region: The primary transition region begins as the temperature approaches the glass transition temperature or its equivalent frequency. At this point, the molecules of the material are more mobile, resulting in larger deformations with substantial energy dissipation. This region is important for industrial applications such as vibration control so good damping properties can be obtained from the selected VE materials.
3. Rubbery Region: This region is associated with high temperatures or low frequencies. Because the polymer chains have more mobility and offer little resistance in this region, the loss modulus, G'' decreases.

2.2.2 Time-Temperature Superposition Principle (TTSP)

The Time-Temperature Superposition Principle (TTSP) is a useful tool when characterizing viscoelastic materials. As outlined above, the loss and storage moduli, and tan δ are all frequency and temperature dependent. With the TTSP, we are able to span the measured data collected at multiple temperatures over a broad time or frequency range. TTSP, in its simplest form, assumes that the complex modulus values at a given frequency and temperature are identical to those at any some other frequency and correspondingly different temperature (Sperling, 2005):

$$G^*(f_0, T_0) = G^*(f = a_T f_2, T) \tag{2.6}$$

where a_T is the thermal shift factor that needs to be determined. One can initially determine the values of a_T by selecting a reference temperature and shifting the measured data points to the left or to the right along the logarithmic frequency scale. Strictly speaking, due to entropic effects, the absolute temperature corresponding to each data point also affects the modulus in another way as well. For this reason, each data point should be multiplied by the ratio, $\rho T/\rho_0 T_0$, where T is the absolute temperature of a particular data point, T_0 is the absolute reference temperature, ρ is the density at the temperature T, and ρ_0 is the density at the reference temperature. But, this vertical shifting is typically small compared to the horizontal shift and is often neglected (Ferry, 1980).

In the relevant literature one can find different shift factor relationships; one commonly used is the *WLF* (Williams – Landel – Ferry) shift factor equation:

$$\log[a_T] = -C_1 \frac{T - T_0}{C_2 + T - T_0} \tag{2.7}$$

where C_1 and C_2 are constants that should be determined for each material at the chosen reference temperature. The WLF equation is often believed to be appropriate in the rubbery regime for $T_g < T < T_g + 100\,^{\circ}C$, which is the case for the adhesives studied in this thesis. Table 2.1 shows representative constants for different materials used with the WLF equation (2.7), where the universal values have been found to be approximately appropriate for a range of polymers, provided the reference temperature is taken to the be the respective glass transition temperature.

Table 2.1: WLF Parameters.

Polymer	T_0 [K]	C_1	C_2 [K]
Poly(ethyl methacrylate)	335	17.6	65.5
Hevea rubber	200	16.7	53.6
Universal Constants	$T_0 = T_g$	17.4	51.6

Source: (Sperling, 2005)

2.2.3 Experimental approach for characterizing viscoelastic materials

To obtain properties of viscoelastic materials one can consider different approaches to perform characterization. In this section we will introduce the experimental methodology used to evaluate the frequency and temperature effect on the properties of the viscoelastic layers in the tapes considered for this study. The temperature and frequency dependence of linear viscoelastic material properties means that a simple quasi-static tensile test is not sufficient to properly characterize such materials. In this work we used dynamic testing to characterize the damping tapes' PSA layer while undergoing harmonic loading at different frequencies and temperatures. A technique widely used in the polymer field to test viscoelastic materials under such conditions is dynamic mechanical analysis (DMA).

During a dynamic oscillatory test, sinusoidal stress or strain is applied to the material at a fixed frequency and temperature and the resultant sinusoidal strain or stress is measured. Additionally, the phase angle, δ, is recorded. Using the geometry of the sample, and the raw data of force and displacement, the DMA determines values of the storage and loss modulus. This test is repeated for different frequencies at a fixed temperature in what is called a frequency sweep. Also the DMA allows cooling and heating of the sample so that temperature can be controlled over a broad range of values, allowing for characterization of viscoelastic materials under different frequency and temperature conditions.

2.3 Dynamic mechanical analysis of damping tapes

The damping tapes were tested using a TA Instruments Q800 Dynamic Mechanical Analysis Instrument shown in Figure 2.5. Although, the complex shear modulus is the target property of

this analysis, we used the tension film clamp shown on Figure 2.6; the procedure used for this analysis will be explained in this section.

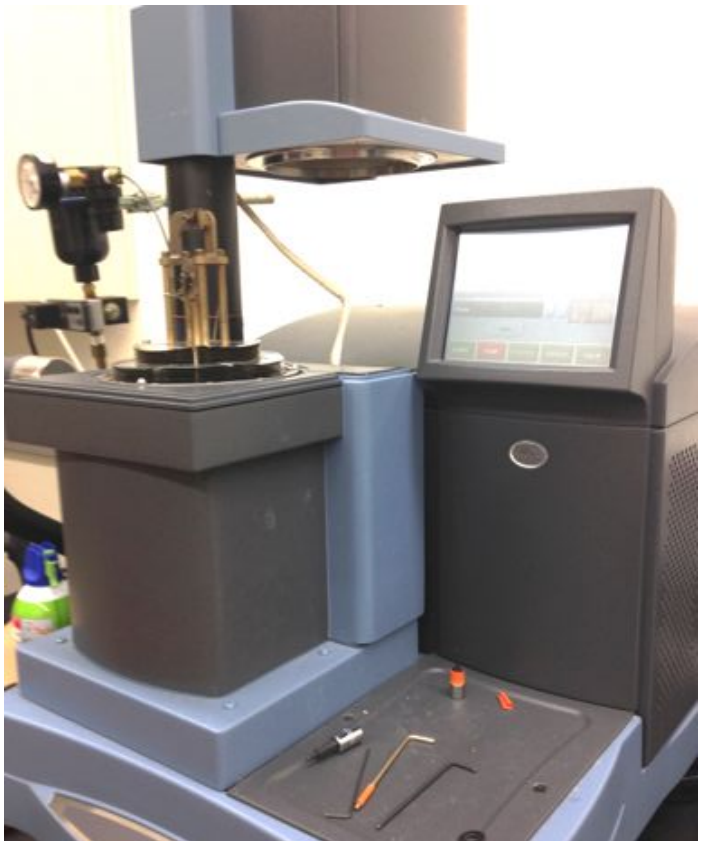

Figure 2.5: TA Q800 Dynamic Mechanical Analysis testing machine.

Figure 2.6: Tension film clamp for DMA Q800 TA Instruments. Source: TA Instruments. "TA Instruments Thermal Analysis" edited by TA Instruments, 2010. URL: http://www.tainstruments.com/pdf/brochure/dma.pdf Used under fair use, 2014.

2.3.1 Experimental sample design

In 2007, Yang et al. performed material characterization of PSA with a backing material using DMA. In their work they considered a multiple layer configuration, consisting of several layers of tape (PSA plus the backing material) laminated one on top of the other. Because the backing material was much stiffer than the PSA, the deformation of the sample recorded by the DMA was assumed to be only due to the deformation of the PSA layers (Yang, Zhang, Moffitt, Ward, & Dillard, 2007). In this work a similar strategy has been used but the geometry considered for our DMA test was different and it will be explained in this section.

The design used in this work is based on a multiple layer configuration as shown in Figure 2.7a. We called this configuration a quad shear sample because it has four active shear areas, each with 8 layers of the damping tape. The geometry used for this samples is shown in Figure 2.7b.

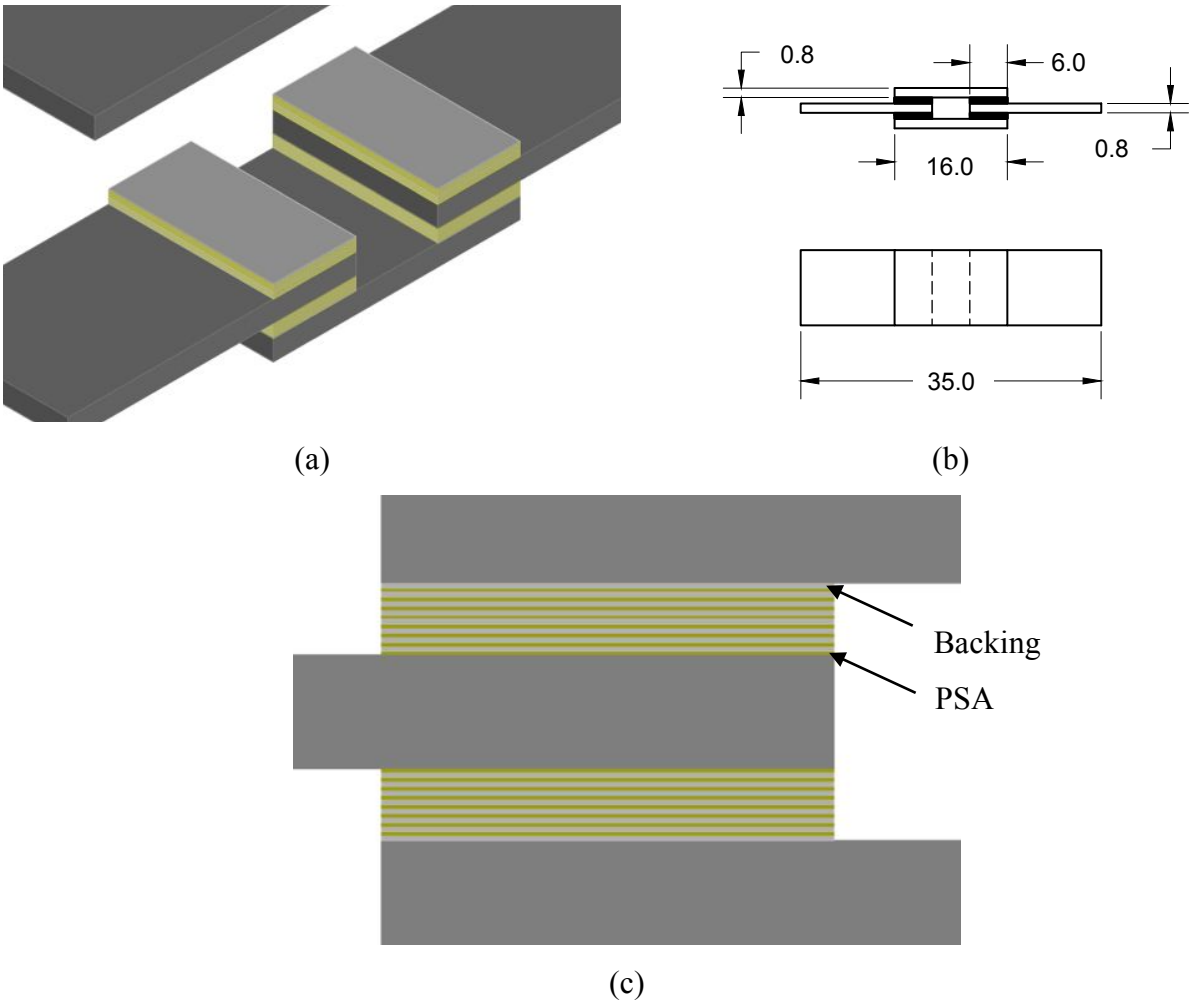

Figure 2.7: Geometry of quad shear samples using the 3M 425 Tape. a) basic geometry of the quad shear sample. b) schematic with geometric values for the quad shear sample. c) detail of two of the four shear areas of the quad shear sample showing the multiple layer configuration.

Figure 2.7c shows a detail of the multiple layer configuration considered in two of the four shear areas. The damping tape used to prepare these samples was the 3M 425 damping tape with an acrylic adhesive 0.05 mm thick and a 0.07 mm dead soft aluminum backing layer (dimensions are nominal values provided by 3M). To explain the construction of these samples, consider the two components showed in Figure 2.8. Part A has eight layers of the 3M 425 PSA tape laminated over a 6 mm length on both sides of small aluminum plates (0.8 mm thick, 16 mm long, and 10 mm wide). Part B of the samples is a similar aluminum plate with the same dimensions. Surface preparation is used to prepare part B for bonding with an auxiliary adhesive; the surface of the

plates were abraded using a 400 grit silicon carbide sandpaper and then cleaned with a water-based acidic surface cleaner. Finally, parts A and B are bonded using a thin layer of epoxy adhesive; C-clamps were used to provide pressure during the bonding of the epoxy adhesive as shown in Figure 2.9a-b.

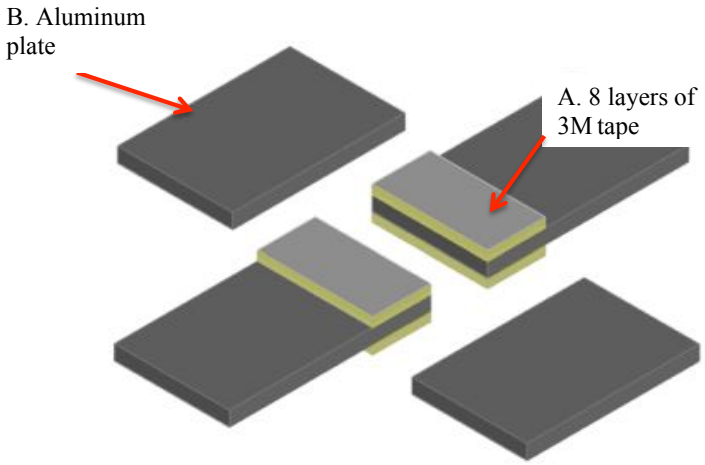

Figure 2.8: Part of the 8 layered quad shear sample with damping tape 3M 425.

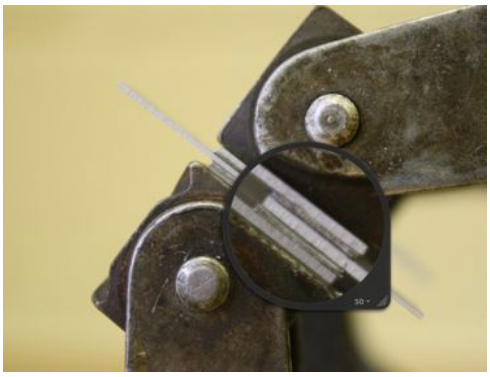

(a)

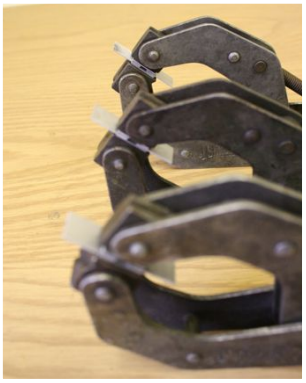

(b)

Figure 2.9: Quad shear samples for DMA testing using 3M 425 tape. a) detail of one of the quad shear samples during bonding of the thin epoxy layer. b) view of three of the tested quad shear samples during bonding.

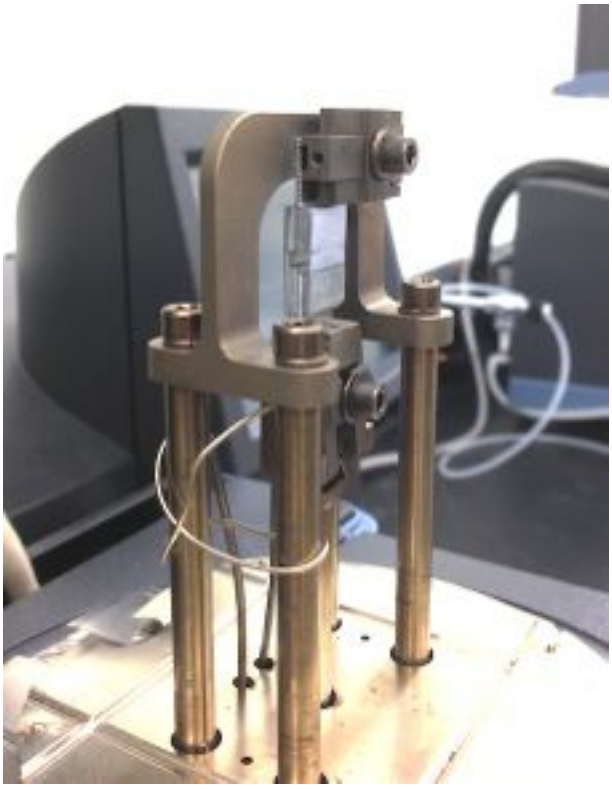

Figure 2.10: Quad shear samples with 3M 425 tape set in the tension film clamp

The tension clamp of the DMA was used and the samples were mounted as shown in Figure 2.10. In the DMA software we configured the system for a tension analysis. The software required input of specific geometric dimensions for this type of analysis. The geometry of a fictitious rectangular sample with the overall geometry of the samples was introduced as shown in Figure 2.11. The experimental sample was cooled to 0°C using liquid nitrogen (LN_2). From this point, data was recorded over a range of frequencies (10^{-1} to 10^{2} Hz) at temperatures of 0°C, 10°C, 20°C, 32°C, 40°C and 50°C.

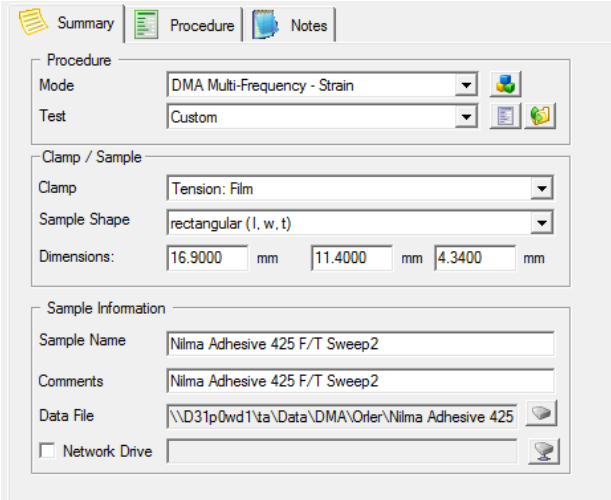

Figure 2.11: Software set up of the DMA test for a sample of adhesive 3M 425

2.3.2 Shear stress calculations from experimental data

From the frequency sweep/temperature step test performed, values of tan δ were obtained from the DMA software as they were calculated from the ratio, G''/G'. This ratio was obtained directly from the excitation and response waves and so it was not obtained from internal manipulation of the DMA software considering the overall fictitious rectangular geometry given to the software (TA-Instruments, 2010). On the other hand the shear properties of the material need to be calculated from the raw data of force and displacement recorded for the samples. These shear properties were computed from an analysis of the quad shear sample. Figure 2.12a shows a free body diagram of the upper part of the tested samples, the double shear force distribution can be observed. As the sample is loaded by the DMA at a given frequency and temperature, Figure 2.12b schematically illustrates the deformation of the damping tape layers in the sample. Figure 2.12c illustrates the deformation of the PSA layer as the deformation of the backing material was deemed to be negligible in the analysis.

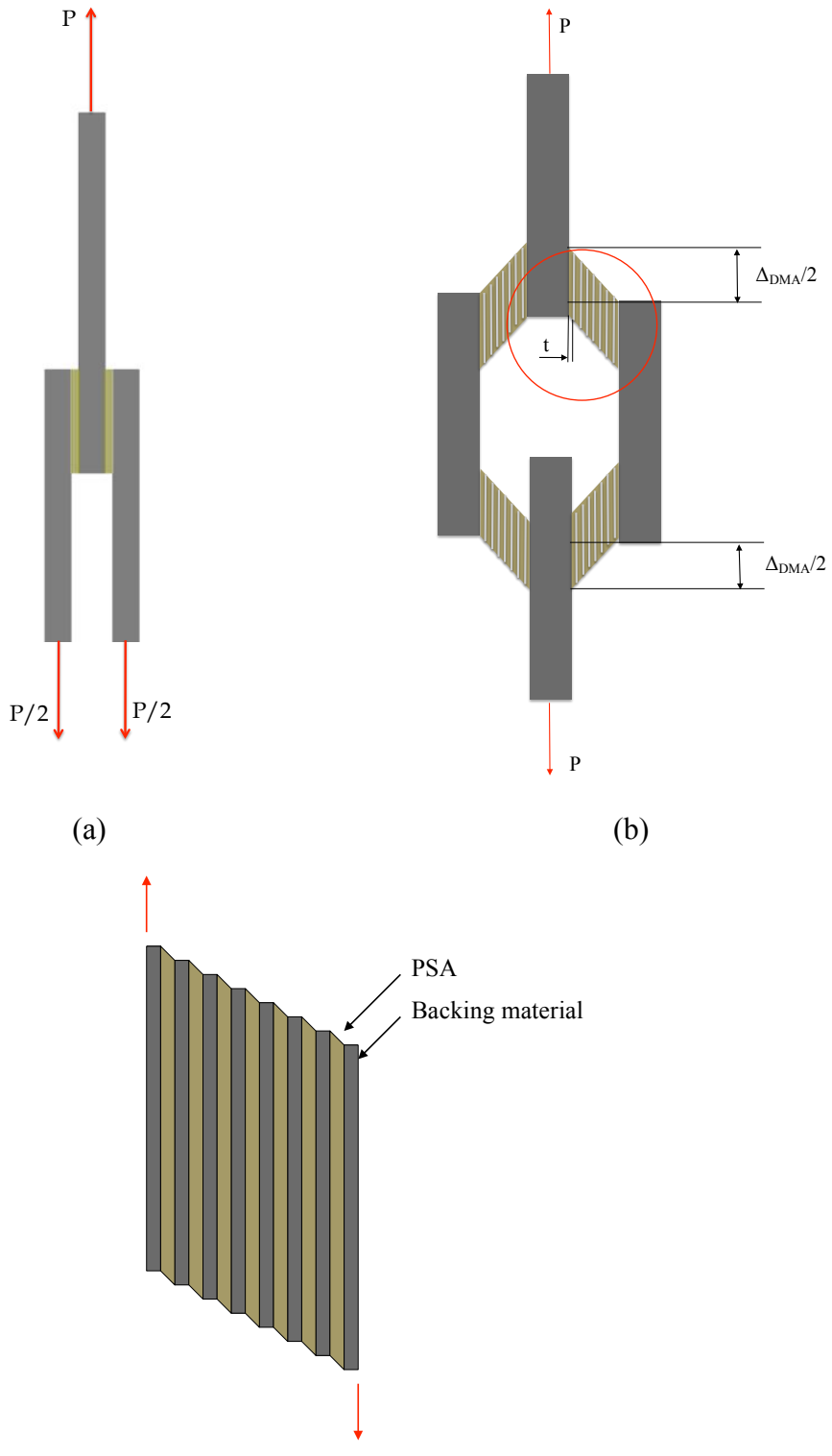

Figure 2.12: Free body diagram of the DMA samples. a) FBD of a tested sample. b) deformed FBD of a tested sample. c) detail of the 8-layered sample deformation.

We assume that as the DMA gives a displacement to one of the aluminum plates and the total displacement of the sample is equally split between the upper and the lower shear areas of the sample, as shown in Figure 2.12b. Therefore, the shear deformation in each active area is half of the total displacement recorded by the instrument over the thickness of the damping tape. This results in:

$$\gamma(t) = \frac{\Delta_{DMA}(t)/2}{n_{layers}t} \tag{2.8}$$

where $\Delta_{DMA}(t)$ is the total deformation of the sample, t is the thickness of a single layer of the PSA portion of the 3M 425 damping tape, and n_{layers} is the number of layers of tape used in the circled region of Figure 2.12b. The average shear stress is:

$$\tau(t) = \frac{P(t)/2}{A} \tag{2.9}$$

where $P(t)$ is the force measured directly from the specimen, and A is the shear area at one of the actives shear sections of the sample as shown in Figure 2.12b. This area is equal to:

$$A = lw \tag{2.10}$$

where l is the overlap length of the PSA tape and w is the width of the sample. The complex shear modulus of the viscoelastic material will be,

$$\begin{aligned} G^*(i\omega) &= \frac{\hat{\tau}}{\hat{\gamma}}\cos\delta + i\frac{\hat{\tau}}{\hat{\gamma}}\sin\delta \\ G^*(i\omega) &= G'(\omega) + iG''(\omega) \end{aligned} \tag{2.11}$$

where $G^*(i\omega)$ is the complex shear modulus, $\hat{\tau}$ is the amplitude of the shear stress, $\hat{\gamma}$ is the amplitude of the shear strain, and δ is the loss angle of the material. Furthermore the storage and loss moduli are $G'(\omega)$ and G'', respectively.

As a final consideration, these calculations assumed no tensile or shear deformation within the dead soft aluminum backing and the aluminum pieces used to construct the samples, because the aluminum is much stiffer than the PSA layer. To validate this assumption we used the recorded values of force to calculate the deformation of the aluminum foil and plates using the following equation:

$$\Delta_{alum} = \frac{PL}{EA_c} \qquad (2.12)$$

where P, L, E, A_c are the force exerted by the DMA, length of the dead soft aluminum backing and the aluminum pieces, Young's modulus, and A_c is the cross-sectional area of the aluminum parts, respectively. The maximum force measured from the DMA results was approximately 0.02 N. By using equation (2.12), the calculated deformation was shown to be in the order of the picometers (pm), six orders of magnitudes less than the deformation data recorded with the DMA. So we can reasonably neglect aluminum deformation and use the displacement data to calculate the shear deformation of the damping tape as described in the previous steps.

Also, note that the shear storage and loss moduli depend on the thickness of the PSA layer. We used the reported values from the 3M datasheet for the damping tape 3M 425 and confirmed experimentally these values using a micrometer. Note that changes in this thickness caused by storage conditions or manufacturing process variations might cause changes of the values of the shear complex modulus calculated with equations (2.11).

2.4 Results of the material characterization

2.4.1 Frequency sweep/isothermal test results

The shear properties from the frequency sweep/isothermal temperature test of the quad sample are shown in Figure 2.13 to Figure 2.15. In these plots the results were obtained from 0 to 50°C, within the frequency range of 10^{-1} to 10^{2} Hz.

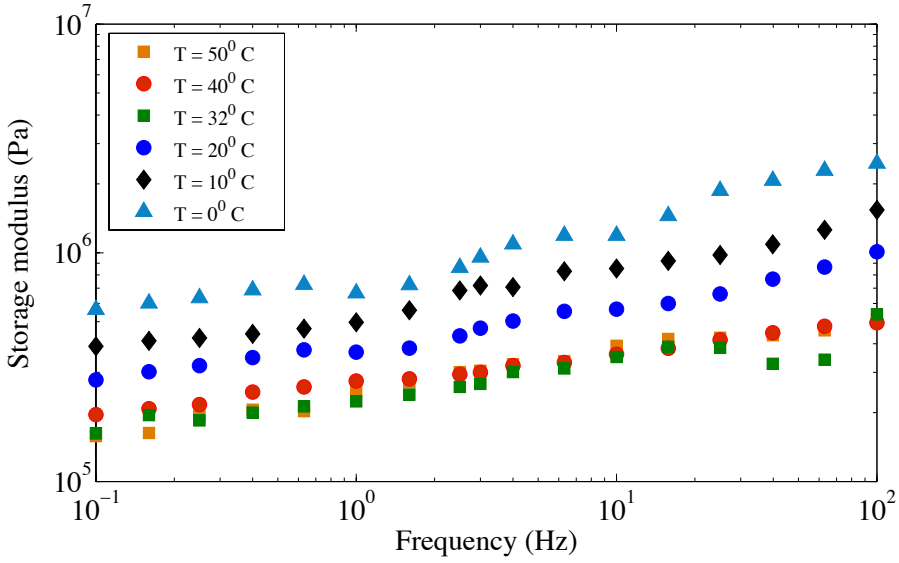

Figure 2.13: Measured storage modulus from the frequency sweep/isothermal temperature test at T=0°C, 10°C, 20°C, 32°C, 40°C, and 50°C for a sample prepared with 3M 425 damping tape.

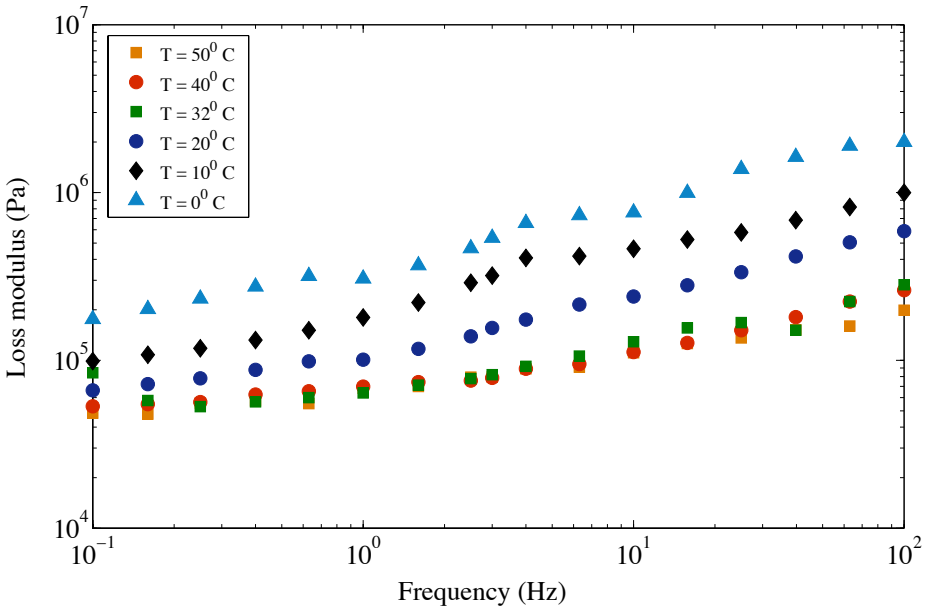

Figure 2.14: Measured loss modulus from the frequency sweep/isothermal temperature test at T=0°C, 10°C, 20°C, 32°C, 40°C, and 50°C for a sample prepared with 3M 425 damping tape.

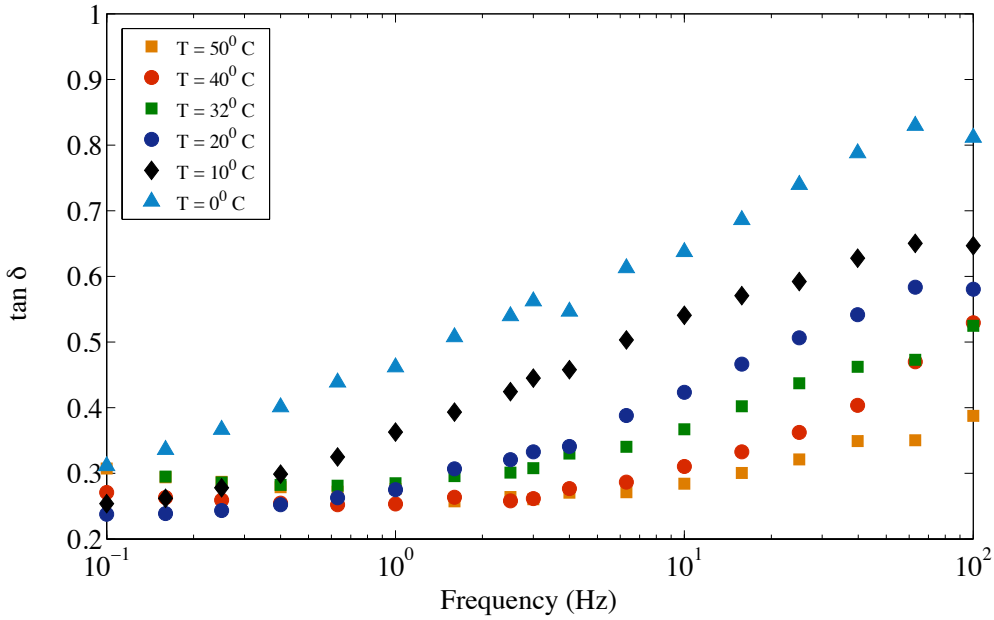

Figure 2.15: Measured $\tan\delta$ from the frequency sweep/isothermal temperature test at T=0°C, 10°C, 20°C, 32°C, 40°C, and 50°C for a sample prepared with 3M 425 damping tape.

2.4.2 Time-Temperature Superposition master curves

The master curves obtained by the Time-Temperature Superposition Principle for the 8-layers of PSA tape sample were generated by shifting the curves in Figure 2.13-Figure 2.15 to the chosen reference temperature of 20°C. This temperature was chosen because the temperature in the laboratory where the vibrations tests were subsequently performed was recorded to be near 20°C. We followed the procedure explained in section 2.4.2 and the results are shown in Figure 2.16 to Figure 2.19. The narrow range of the temperature steps used only allowed the frequency of the master curves to cover from 10^{-3} to 10^{3} Hz approximately. These plots could be used to predict the damping performance of the PSA on the tested 3M 425 damping tape over this range of the frequencies.

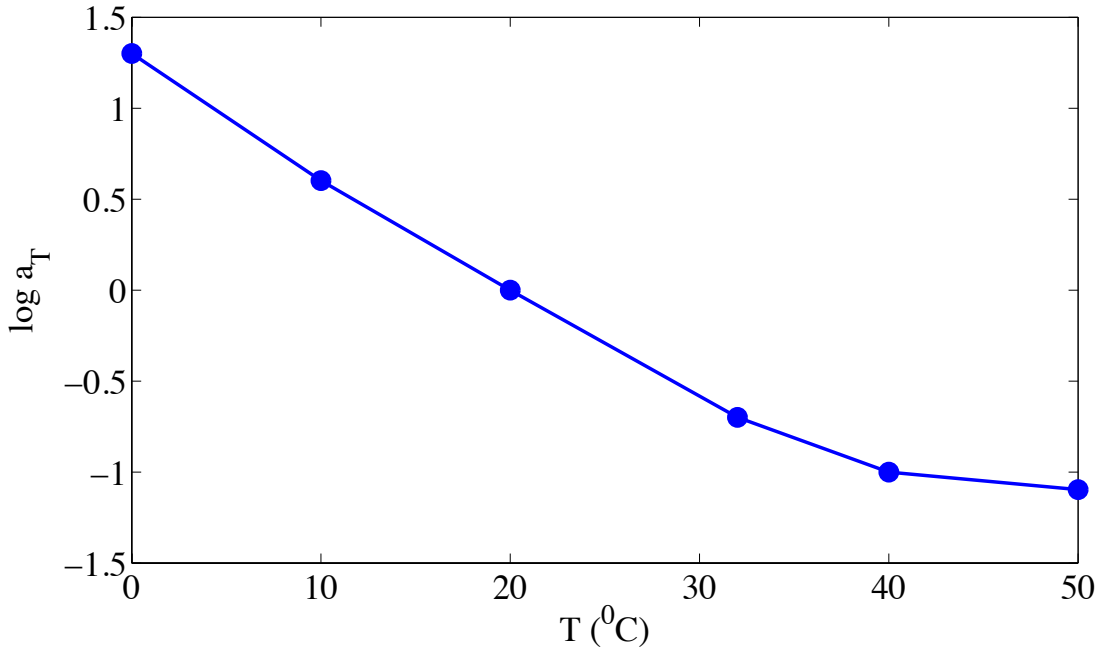

Figure 2.16: Shift factor obtained for the TTSP for T_{ref} = 20°C.

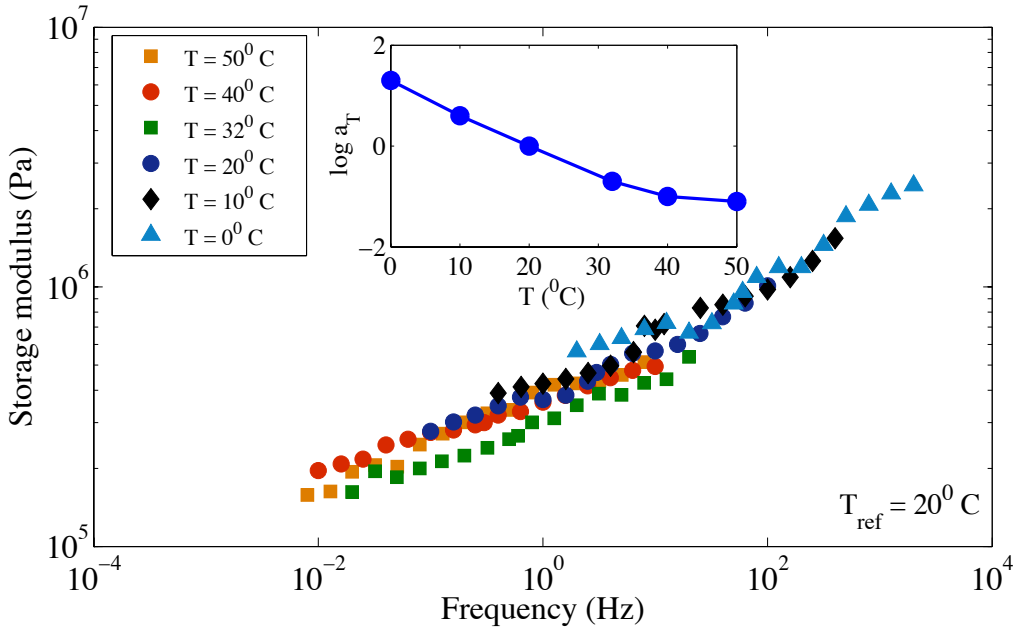

Figure 2.17: The TTSP master curve for storage modulus vs. frequency for a sample prepared with 3M 425 damping tape; T_{ref}=20°C.

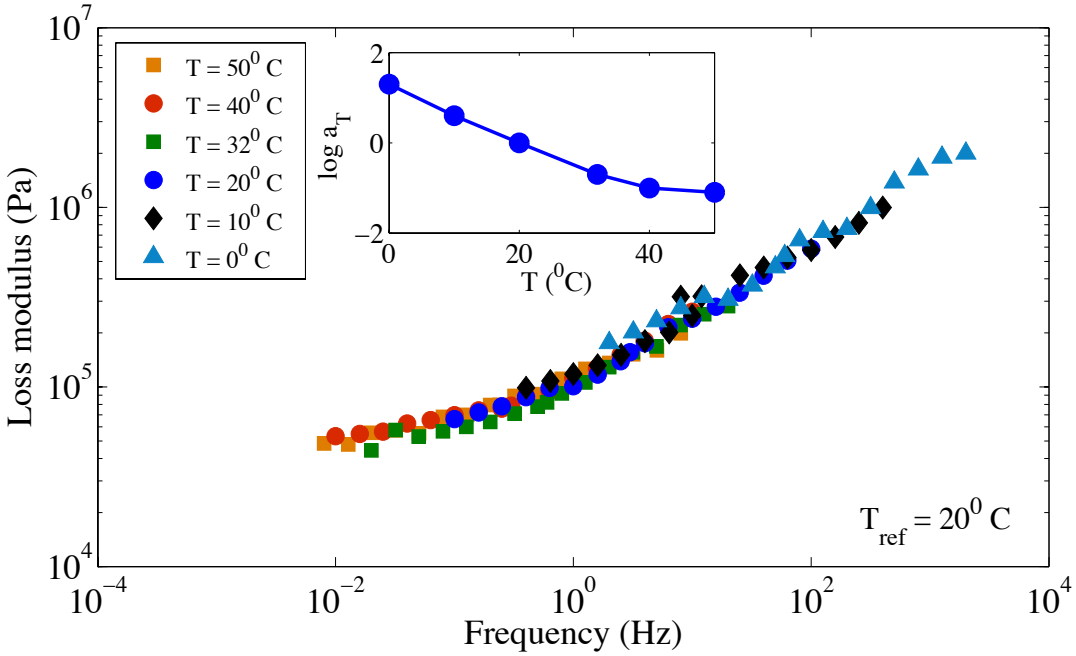

Figure 2.18: The TTSP master curve for loss modulus vs. frequency for a sample prepared with 3M 425 damping tape; T_{ref}=20°C.

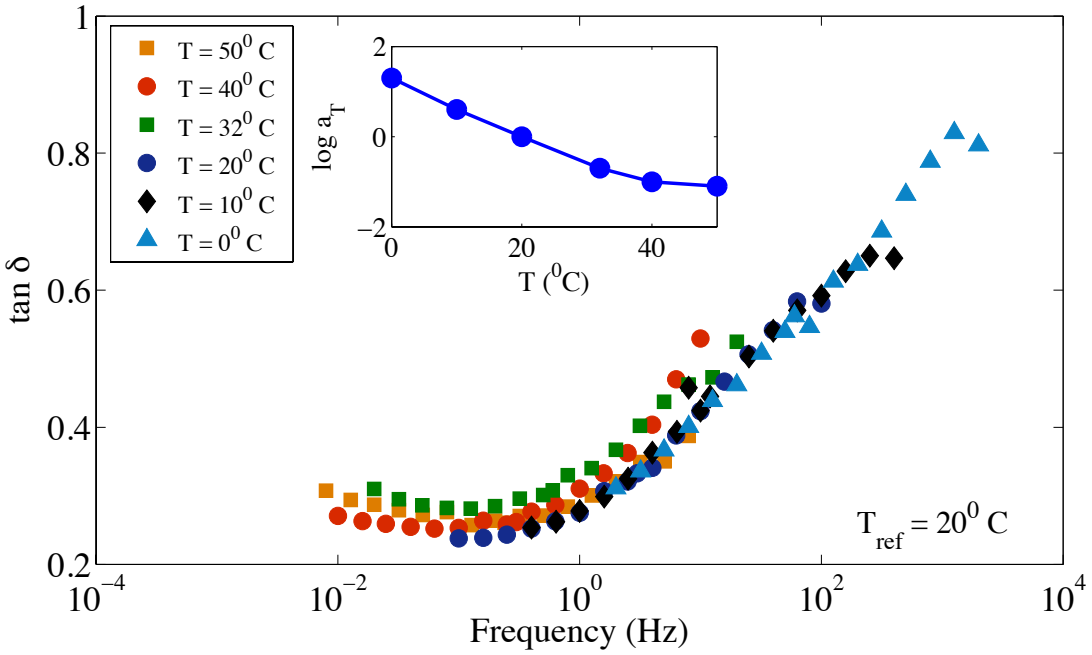

Figure 2.19: The TTSP master curve for tan δ vs. frequency for a sample prepared with 3M 425 damping tape; T_{ref}=20°.

The master curves show reasonable shapes, though curves are not as smooth as would be desired. The small thicknesses of the PSA layers and stiff behavior of the geometry used may have contributed to the greater variation. Nonetheless, the results were deemed adequate for the present study, in part because modulus appears to the one half power in the resulting stress distributions, thereby reducing sensitivity to PSA shear modulus.

2.5 Summary

The quad shear specimen designed for this section has been used to characterize the properties of the acrylic pressure sensitive adhesive (PSA) of the 3M 425 damping tape. A series of experiments was conducted using a dynamic mechanical analyzer (DMA). The samples were setup in the tensile film clamp of the DMA; frequency sweeps at several temperature steps were carried out. The shear storage and loss moduli were calculated by analyzing the free body diagram of Figure 2.12 and the raw force and displacement data recorded by the DMA, with results obtained from equations (2.11). Values of tan δ, were obtained directly from the DMA,

because they were not affected by the fictitious geometrical data given to the DMA software. Master curves were produced by using the time-temperature superposition principle (TTSP) at room temperature from the temperature step/frequency sweep tests. These master curves can be used to estimate mechanical properties of the PSA over a broad range of frequencies at different temperatures.

Chapter 3 Mechanical Analysis of Discretized Constrained Damping Layers and their Effects on a Structure's Damping

3.1 Methodology to the theoretical analysis of discretized damping layers

In this chapter, the theoretical foundations for discretized constrained damping layers are given. Our analysis is based on a linear viscoelasticity analysis using the material characterization performed in Chapter 2, and basic vibrations principles to set the theoretical pillars to understand the physical parameters governing energy dissipation for basic structural elements such as cantilever beams. We considered different geometries of commercially available damping tapes and obtained theoretical loss coefficients from our analysis. In this chapter, based on the previous work of Plunkett and Lee, we repeat the derivation of an expression to calculate the optimal discretization length required to maximize the loss coefficient of the structure for a given amount of damping material.

3.2 Mechanics of constrained damping layers

In 1960, Parfitt and Lambeth made a comprehensive study about free and constrained damping layers. They experimentally compared free and constrained damping layers and called the latter "damping tape". During experiments, they noticed that buckling of the constraining layer, induced during storage or loading, caused an improvement of the damping properties. Later, Parfitt published one of the first papers in the field and analyzed the effect of discretizing cuts on the damping tapes instead of buckling, and concluded that the discretized constraining layer effectively improved the damping (Parfitt & Lambeth, 1960). In this work, we will consider vibrating cantilever beams with discretized damping layers; analytical and experimental results are compared in the next chapters, concluding that this technique of discretizing the constrained layer enhances damping of beams. This chapter also provides a mechanics background using

viscoelasticity, along with fundamental vibrations and strength of materials concepts to estimate the loss coefficient of cantilever beams with discretized damping layer. Additionally, a beam on an elastic foundation approach is included to estimate the critical load at which the backing material of the damping tape will buckle. These equations will be used later in Chapter 6 to compare and interpret experimental observations.

3.3 Optimization of discretized damping tape segment length

In this section we will follow the procedure published by Plunkett and Lee in order to present an expression for the optimal discretization length in order to maximize the loss coefficient of the structure without adding additional damping tape (Plunkett & Lee, 1970). To this end, we will assume that the analysis is performed over a symmetric cross section; this means that the damping tape is bonded at each side of the beam as shown in Figure 3.1

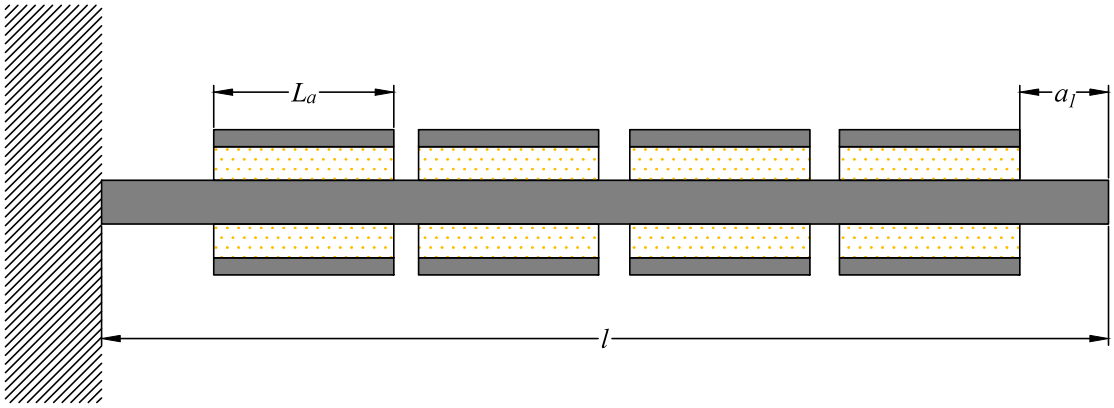

Figure 3.1: Schematic illustration of discretized damping layers bonded to a cantilever beam.

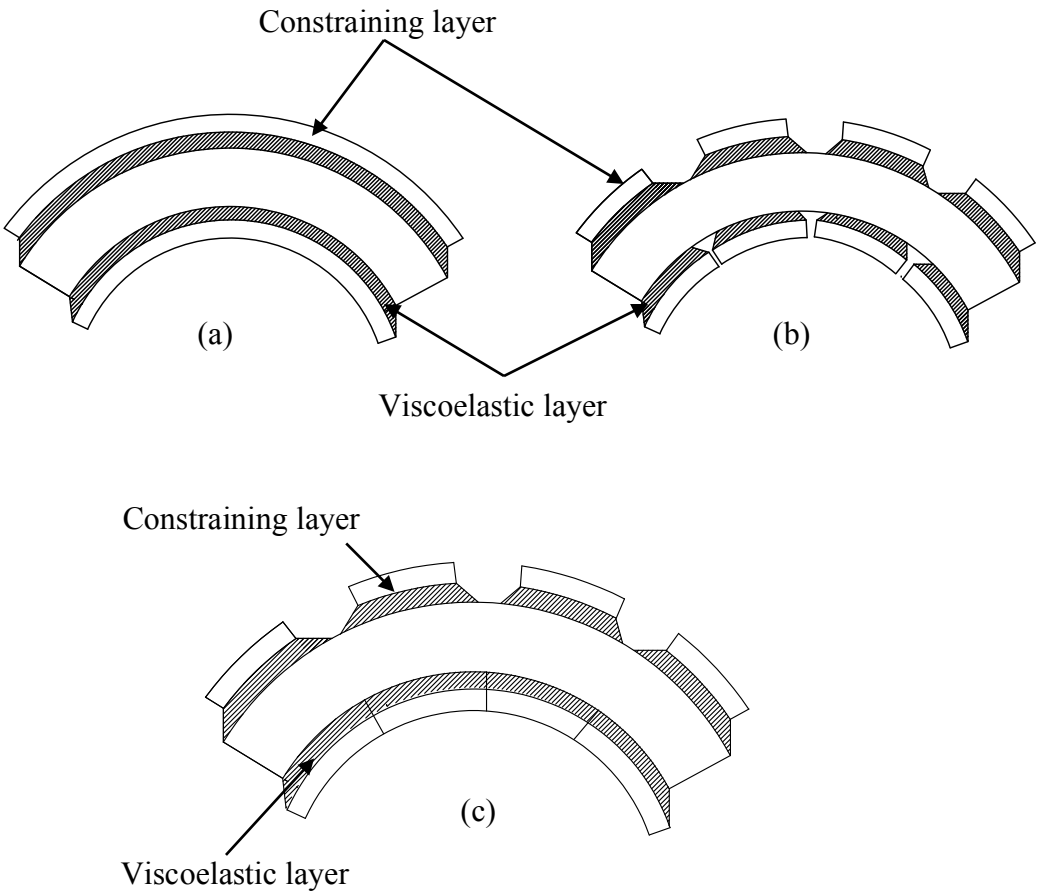

Figure 3.2: Highly exaggerated shear deformations of a: a) continuous constrained damping layer. b) discretized constrained damping layer. c) upper discretized constraining damping layer and lower layer with small spacing between the discretized segments allowing contact.

As an assumption from the literature review given in section 1.1.3, the dominant damping mechanism in damping tapes is the shear deformation of the VE layer induced by the stiffer constraining layer. Figure 3.2a shows a continuous constrained damping layer; notice that the shear deformation due to the stiff backing is localized at the ends of the constraining layer. Figure 3.2b shows a discretized damping layer bonded to a deformed beam in this case. Notice that additional sections of the viscoelastic material are subjected to shear deformation compared to Figure 3.2a. The shear deformation produced at the ends of the stiff backing is now present at the ends of each segment of the discretized damping layer. As an additional configuration,

consider Figure 3.2c showing in the upper damping layer the effect of the constraining layer as explained for Figure 3.2b, but for the lower section since there is no sufficient gap between each segment and we will not obtain the enhancement of the damping due to the discretization of the damping layer, similarly to what happens in Figure 3.2a. In this work we considered the case illustrated in Figure 3.2b.

3.3.1 Volkersen's shear lag analysis and Plunkett and Lee methodology

In 1938, Volkersen proposed a shear lag model in which the adherend was modeled as a member undergoing axial or longitudinal deformation only and the adhesive as a continuous shear spring (da Silva, 2011). In this section, the equation for the shear strain deformation of the constrained viscoelastic layer is obtained applying the shear lag model as used by Plunkett and Lee. The following assumptions were made in the analysis, which follows (Plunkett & Lee, 1970):

1. The thicknesses of the constraining layer and of the viscoelastic layer are very small compared to the thickness of the base structure, for this study a cantilever beam.
2. The constraining layer segments extend but do not deform in shear.
3. The VE layer deforms in shear and offers no axial stiffness
4. The VE layer behaves as a linear VE material. Complex notation can be used to define the complex shear modulus: $G^*(i\omega) = G'(\omega) + iG''(\omega) = \left|G^*\right|(\cos\delta + i\sin\delta)$.
5. The constraining material is elastic and does not dissipate energy.
6. The effects of Poisson ratio are negligible on the one-dimensional problem.
7. The axial strains at the interface of the base structure and the VE layer are compatible.
8. The shear strain is uniform through the thickness of the VE layer.
9. The normal stress is approximated as being uniform through the thickness of the constraining layer.
10. The elastic modulus of VE layers is small compared to those of the base structure and the constraining layer.

To obtain the expressions for the shear modulus, Plunkett and Lee carried out the following analysis: locating the origin of the coordinate system at the center of the constraining layer, as shown in Figure 3.3a.

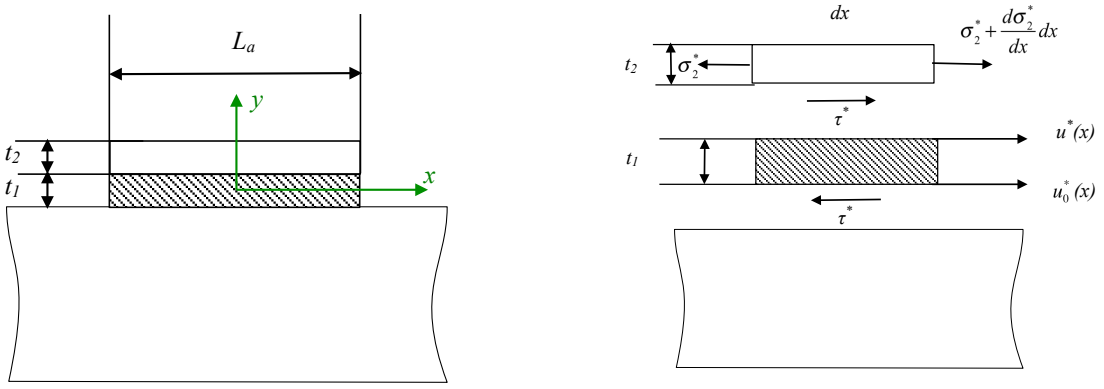

(a) (b)

Figure 3.3: a. Coordinate system as located for the Plunkett and Lee analysis. b. Schematic illustration of axial stress and shear stress on the constraining and viscoelastic layer, respectively. Source: Plunkett, R. and C. T. Lee. "Length Optimization for Constrained Viscoelastic Layer Damping." *The Journal of the Acoustical Society of America* 48, no. 1B (1970): 150-161. Used under fair use, 2014.

From Figure 3.3b, the equilibrium equations for the constraining layer and the constitutive equations are:

$$\left(\frac{d\sigma_2^*}{dx}\right)t_2 = \tau^*$$
$$\sigma_2^* = E_2\varepsilon^* = E_2\frac{du^*}{dx} \qquad (3.1)$$

where E_2 is the Young's modulus of the constraining layer, and t_2 is the thickness of the constraining layer. The adhesive complex shear stress is defined as:

$$\tau^* = G^*\gamma^* = \frac{G^*}{t_1}(u^* - u_0^*) \qquad (3.2)$$

where, G^* is the complex shear modulus of the viscoelastic material; γ^* is the complex shear strain; t_1 is the thickness of the viscoelastic layer; u^* is the displacement at the upper interface

(constraining layer/viscoelastic material); and u_0^* is the displacement at the interface of the basic structure and the viscoelastic material. Assuming a uniform shear strain through the thickness of the viscoelastic layer:

$$u_0^* = \varepsilon_0^* x \tag{3.3}$$

where ε_0^* is the strain in the beam. Substituting equations (3.3) and (3.2) into (3.1), and considering the magnitude of the shear modulus of the adhesive we obtain the governing differential equation:

$$\frac{d^2u^*}{dx^2} = \frac{\left|G^*(i\omega)\right|}{E_2 t_1 t_2}(u^* - \varepsilon_0^* x) \tag{3.4}$$

The term $\sqrt{\left|G^*(i\omega)\right| / E_2 t_1 t_2}$ from equation (3.4) can be recognized as the shear lag parameter from Volkersen's original shear lag model derivation. The inverse of this parameter is called the "shear lag distance". The shear lag distance represents the characteristic distance associated with the transfer of axial load from one adherend to the other, meaning that there is a spatial lag before the axial stress reaches equilibrium. (Dillard D. , 2013) (da Silva, Ochsner, & Adams, 2011). Volkersen's shear lag parameter is defined as:

$$SL = \sqrt{\frac{t_1}{\left|G^*(i\omega)\right|} \frac{E_b t_b E_2 t_2}{E_b t_b + E_2 t_2}} \tag{3.5}$$

where E_b and t_b are the Young's modulus and thickness of the base structure, respectively. Notice that from assumption (1) given earlier in this section, the ratio of the damping tape to the beam thickness was very small, so equation (3.5) can be written as:

$$\frac{1}{SL} = \sqrt{\frac{\left|G^*(i\omega)\right|}{E_2 t_1 t_2}}$$

Finally, equation (3.4) can be expressed as:

$$\frac{d^2u^*}{dx^2} = \frac{1}{SL^2}(u^* - \varepsilon_0^* x) \tag{3.6}$$

Boundary conditions for equation (3.6) considering a single element of the constraining layer are:

$$\frac{du^*}{dx} = 0 \quad \text{at } x = \pm\frac{L_a}{2} \tag{3.7}$$

The general solution of equation (3.6) satisfying the boundary conditions is:

$$u^*(x) = \varepsilon_0^*\left(x - SL\frac{\sinh(x/SL)}{\cosh(L_a/2SL)} \right) \tag{3.8}$$

Equation (3.8) governs the shear deformation of the viscoelastic layer used in the damping treatment. In the next section we relate the shear deformation of the viscoelastic layer to the loss coefficient of the system.

3.3.2 Energy dissipation within the viscoelastic layer

An analytical model was needed to use the equation for the shear deformation of the viscoelastic layer obtained in section 3.3.1 and find the corresponding loss coefficient for cantilever beams to which the damping treatment was applied. From classical viscoelastic concepts and following the procedure given by Plunkett and Lee, the energy dissipated per cycle per volume unit of a linear viscoelastic material subjected to uniform shear is the area within the stress-strain hysteresis loop, and is given by (Brinson & Brinson, 2007) (Dillard, 2013):

$$\frac{\text{Work dissipated}}{\text{cycle}} = \pi\hat{\gamma}^2 G''(\omega) \tag{3.9}$$

where, $\hat{\gamma} = \left|\gamma^*\right|$ as in (3.2), and $G''(\omega)$ is the shear loss modulus of the viscoelastic material. Using the result of equation (3.8) to obtain the complex shear strain and substituting the results into equation (3.9) and multiplying by the beam's width gives the work dissipated per cycle per unit width:

$$\frac{\text{Work dissipated}}{\text{cycle}} = \pi G''(\omega)\left(\varepsilon_0^*\right)^2 \frac{1}{t_1} SL\left(\frac{\sinh(x/SL)}{\cosh(L_a/2SL)}\right)^2 \qquad (3.10)$$

Note that Equation (3.10) is in terms of the axial strain of the base rather than explicitly in terms of the viscoelastic layer shear strain; this was assumed in (7) in section 3.3.1. Equation (3.10) can also be written in terms of $G'' = \left|G^*\right|\sin\delta$, where the loss shear modulus is expressed in terms of the magnitude of the shear stress and tan δ of the viscoelastic material. The resulting energy dissipation of the viscoelastic layer was determined by integrating over the length of one damping tape element of the assumed discretized surface treatment:

$$W_{dis} = 2\pi\left(\varepsilon_0^*\right)^2 t_2 E_2 L_a \frac{1}{r}\left[\frac{\sinh(r\cos\delta/2)\sin\delta/2 - \sin(r\sin\delta/2)\cos\delta/2}{\cosh(r\cos\delta/2) + \cos(r\sin\delta/2)}\right] \qquad (3.11)$$

where r is the ratio of the adhesive layer length, L_a to the shear lag distance, SL. From equation (3.11), the loss coefficient of an element of the discretized damping layer was obtained:

$$\eta_d = \frac{W_{dis}}{W_{nom}} \qquad (3.12)$$

where η_d is the nondimensional loss coefficient, and W_{nom} the nominal energy stored by the constraining layer of the damping tape. This would be the energy stored by an element of the discretized damping layer if the whole layer were strained by an amount of ε_0. The nominal energy stored, W_{nom} is given by:

$$W_{nom} = \frac{1}{2}\left(\varepsilon_0^*\right)^2 E_2 t_2 L_a \tag{3.13}$$

Applying equations (3.11) and (3.13) into equations (3.12), the loss coefficient is provided by (3.14):

$$\eta_d = 4\pi \frac{1}{r}\left[\frac{\sinh(A)\sin\delta/2 - \sin(B)\cos\delta/2}{\cosh(A)+\cos(B)}\right] \tag{3.14}$$
$$A = r\cos\delta/2$$
$$B = r\sin\delta/2$$

Notice, equation (3.12) is different from the specific damping defined for viscoelastic dissipation given by:

$$\psi = \frac{\text{Energy dissipation/cycle}}{\text{Max. energy stored}} \tag{3.15}$$
$$\psi = 2\pi\tan\delta$$

Notice that equation (3.14) gives values of the loss coefficient of an element of the discretized damping layer and it only depends on the ratio *r* and the loss tangent, tan δ of the viscoelastic material. Figure 3.4 shows loss coefficient plots for different viscoelastic material loss tangent values, tan δ. It can be observed that when tan δ < 1, the loss coefficient is more dependent on the loss tangent, but when tan δ > 1 this dependence decreases. One important observation from Figure 3.4 is that for all values of tan δ, the maximum loss coefficient is found when, $r = 3.28$.

Hence, it has been confirmed that for a given viscoelastic material for which its loss tangent is available, the maximum damping is obtained when the length of the discretize segments is 3.28 times the shear lag distance, *SL* (Parfitt, 1962) (Plunkett & Lee, 1970).

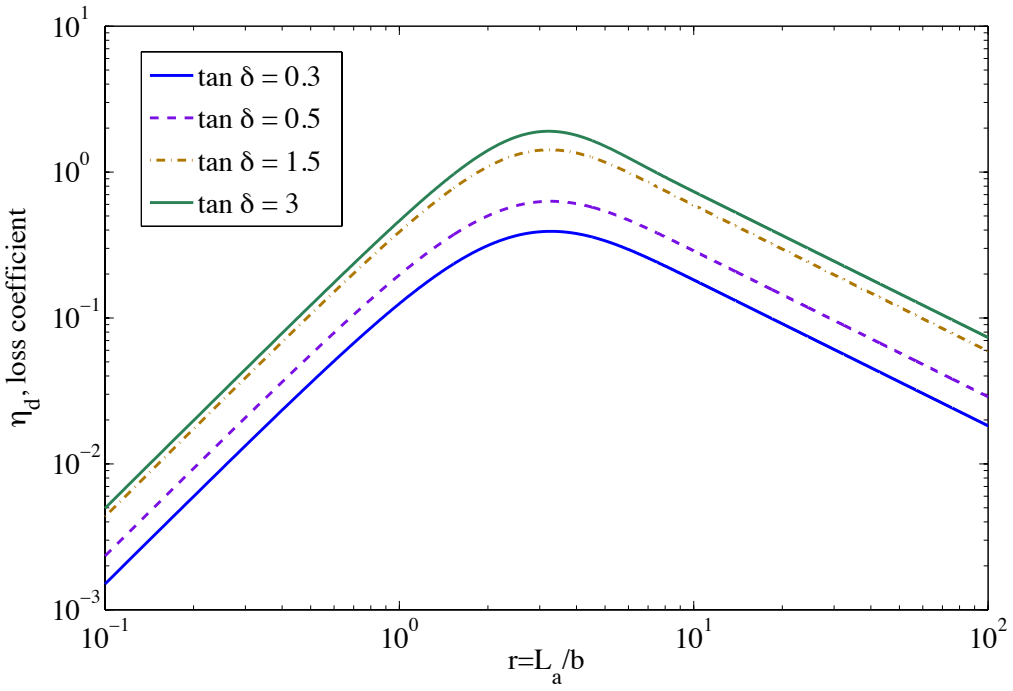

Figure 3.4: Loss coefficient versus $r = L_a / SL$ for a single constraining layer, plots with different values of tan δ.

From Figure 3.4, we can observe the frequency dependence of the loss coefficient for different values of tan δ. Therefore, a proper characterization of the viscoelastic material used as the damping layer is important. In this research, the DMA allowed us to obtain these material properties over a considerably wide range of frequencies and temperatures. This discretization method with the proper damping material can be relevant for industrial applications for which the weight cannot be dramatically increased.

3.4 Discussion of the theoretical results.

3.4.1 Uniform strain distribution analysis

It has been demonstrated that discretizing damping tapes can increase damping, and that there is an optimal segment length to obtain the maximum loss coefficient. This length depends on the mechanical properties of the viscoelastic damping polymer. In this section we will address the end effect that provides the increase in the loss coefficient. To this end, we write the shear stress in the viscoelastic layer from equation (3.2) and (3.8):

$$\tau^* = G^* \frac{\varepsilon_0^* SL}{t_1} \frac{\sinh(x/SL)}{\cos(L_a/2SL)} \tag{3.16}$$

The dimensionless shear stress, $\bar{\tau}$, in the viscoelastic material can be calculated by dividing equations (3.16) by $G^* \frac{\varepsilon_0^* SL}{t_1}$. This yields:

$$\bar{\tau} = \frac{\sinh(x/SL)}{\cos(L_a/2SL)} \tag{3.17}$$

Figure 3.5 shows how the dimensionless shear stress changes along the length of the surface treatment considering uniform strain in the underlying substrate. For a large L_a (orange line), there is no shear stress away from the ends of the segment, so the damping is small. On the other hand, if the L_a is very small as shown in Figure 3.5 (red line), the constraining layer does not exert sufficient constraint on the adhesive material. This means that the shear strain due to the stiff constraining layer is reduced so the energy dissipation also decreases, and the damping is small. For values near the optimal length ratio obtained by Plunkett and Lee and confirmed in section 3.3.2, *r = 3.28*, the shear-strain energy integrated over the length of the damping tape section, L_a, reaches maximum values as shown in Figure 3.5 (blue and green lines). We observe that more regions of the damping tape are actively being sheared if the discretization length is near the optimal value.

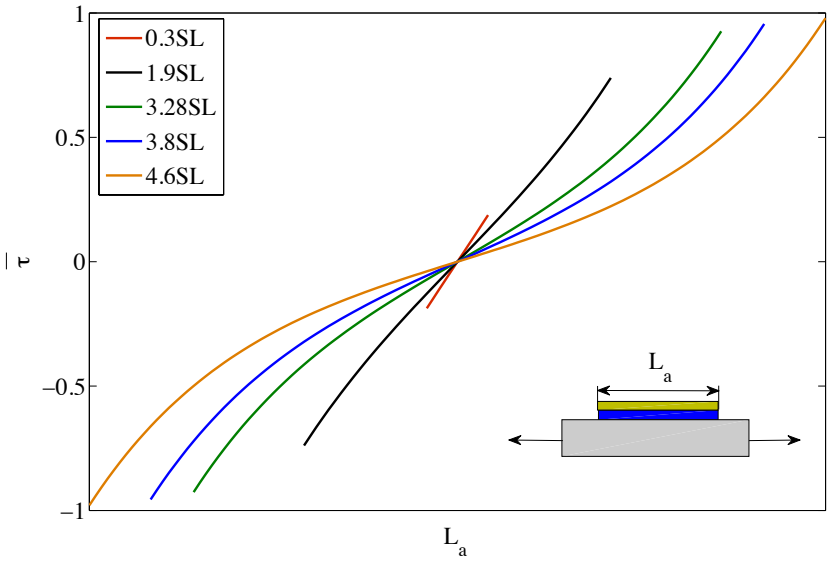

Figure 3.5: Nondimensional shear stress undergoing uniform strain for different lengths of surface treatment.

3.4.2 Cantilever beam strain distribution

The dimensionless analysis permitted us to understand the physical phenomena behind the increase damping obtained with the discretized damping layer. Now, we will extend this analysis considering the strain distribution for a structural element. The shear stress distribution along the length of the segment can be obtained from equation (3.16). Again, from assumption (7) in section 3.3.1 the strain distribution will be taken as the strain to which the surface of the structural element is subjected. So ε_0^* in equation (3.16) will be replaced by:

$$\varepsilon_0^* = -\frac{t_b}{2}\frac{d^2y(x,t)}{dx^2} \tag{3.18}$$

where $t_b/2$ is the distance from the neutral axis to the top fiber of the structure's cross section, and $d^2y(x,t)/dx^2$ is the curvature of the structure. In this case we analyzed a cantilever beam

with uniform cross section so the curvature of a cantilever beam can be determined from the mode shapes for a cantilever beam vibrating at the fundamental mode. If we set $l = L$ (See Figure 3.1), the shear stress distribution for the cantilever beam with a continuous damping layer is shown in Figure 3.6.

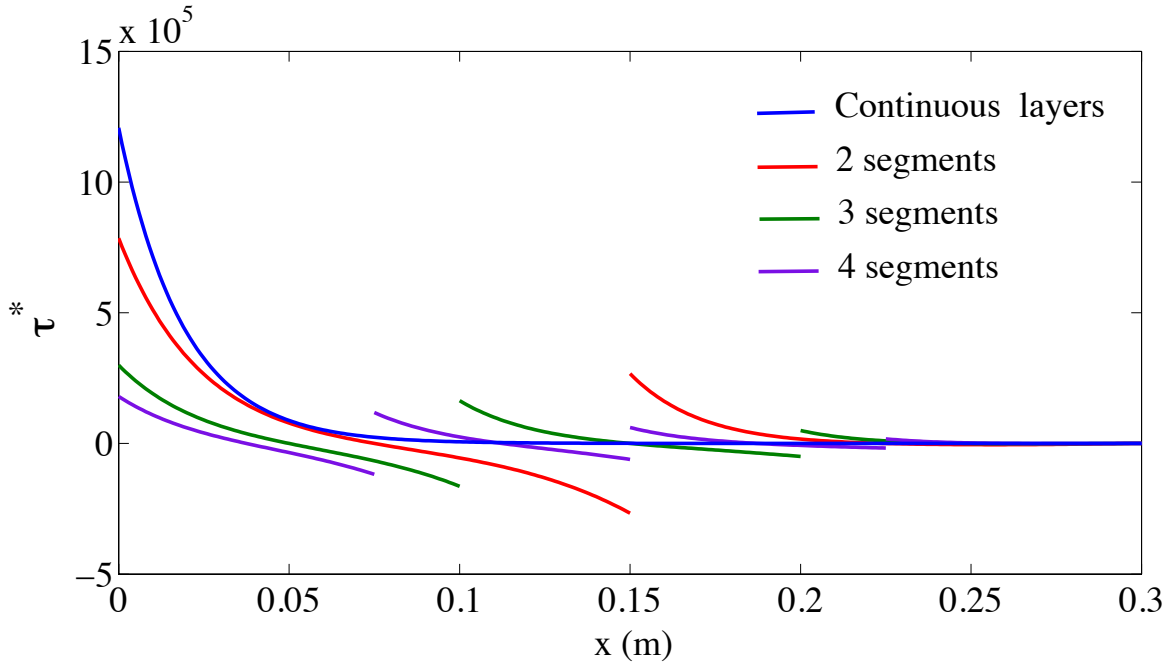

Figure 3.6: Shear stress along the length x of a cantilever beam vibrating at the fundamental mode.

Figure 3.6 shows the shear stress distribution for a discretized damping layer, taking into account the strain distribution of the cantilever beam vibrating at the fundamental mode. The x-axis of Figure 3.6 represents the total length of the analyzed structural element. As we can observe, the largest amount of strain is near the base of the structure, where the axial bending strains in the beam are also largest. In Figure 3.6 the blue line corresponds to a continuous damping layer. Notice how the portion near the base sustains most of the shear stresses and therefore only this region is successfully dissipating energy. On the other hand red, green, and purple lines in Figure 3.6 show the shear stress distributions as we discretized the damping layer. With these configurations we observe that regions that were not undergoing shear stress in the continuous-damping layer configuration start participating in the energy dissipation of the structure, thereby leading to the enhanced damping. This figure could be a bit misleading since dissipation is

proportional to the square of the stress amplitude, so it is appropriate to show energy dissipation as a function of position along the beam.

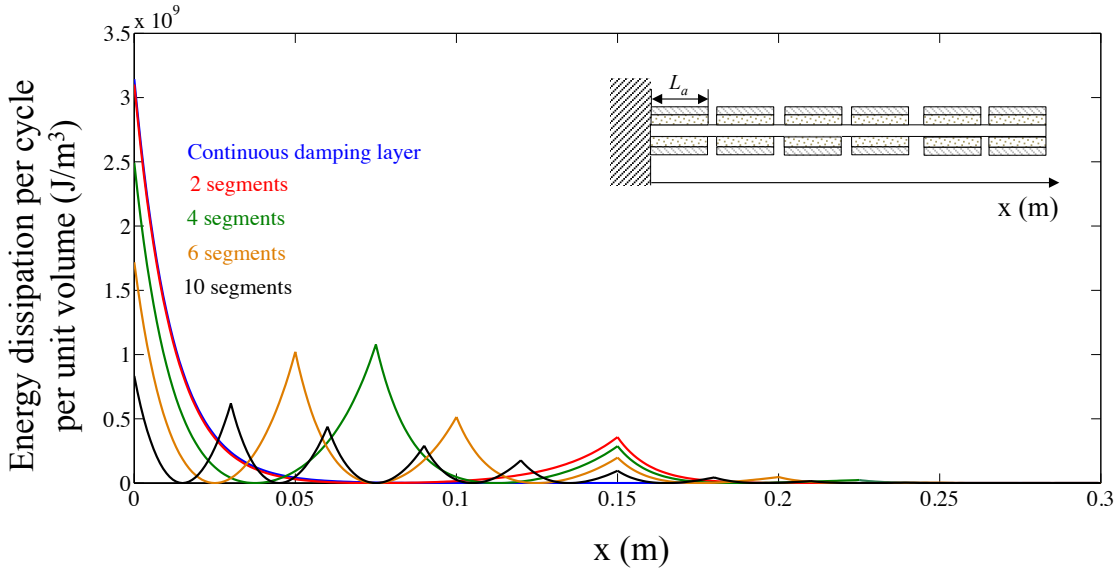

Figure 3.7: Energy dissipation per cycle per unit volume of a cantilever beam in its first vibration mode with damping tapes on both sides for different number of damping layer segments.

Figure 3.7 shows the energy dissipation per cycle per unit volume of a continuous and discretized damping layer applied to a cantilever beam on its first vibration mode. Observe that for the continuous damping layer, most of the energy dissipation occurs during the first 50 mm of the beam; the remaining length of the damping layer is not undergoing shear deformation and therefore the energy dissipation at this section of the beam is near zero. (In fact, as will be demonstrated later in the thesis, removing much of this inactive material can reduce added mass and cost and actually improve the damping.) On the other hand, for discretized configurations consisting of 2 to 6 segments, more regions of the damping tape are contributing to the energy dissipation of the system. Conversely, when the damping layer is discretized into too many segments, the energy dissipation decreased compared to the optimal value of the ratio, *r*. Hence, having a discretized damping layer increases the damping of the structure compared to the

continuous damping layer, but as we increased the number of segments, the benefits of discretizing the damping layers decreased.

3.5 Beam on elastic foundation approach applied to damping tapes.

The damping tapes considered in the analysis have two basic components, a stiff backing material, in this case a dead soft aluminum layer, and an acrylic pressure sensitive adhesive (PSA). (Note that dead soft indicates a very low yield strength; the modulus of the aluminum is still about 70 GPa.) During deflection to which the beam is subjected, axial forces are induced in the backing material as shown in Figure 3.8. As the response amplitude increases, the backing material of the damping tapes is subjected to increasingly higher axial forces that might cause buckling of the stiff backing layer. (See Figure 6.1a) At this point, the energy dissipation by means of shear deformation and the theoretical formulation described in sections 3.3 and 3.4 will no longer be sufficient to describe the behavior, as an additional deformation mode and associated dissipation are introduced.

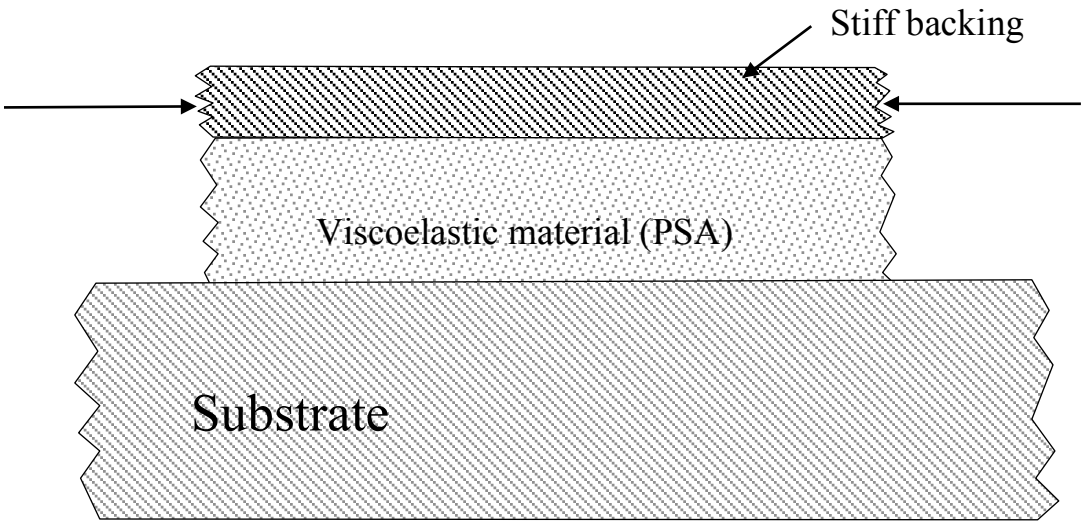

Figure 3.8: Schematic of the damping tape configuration.

The stiff backing layer of the damping tape over the viscoelastic layer can be modeled as a beam on an elastic foundation (BoEF) or Winkler foundation. The Winkler foundation assumes that the force required to deflect a foundation is linearly proportional to the deflection of the beam:

$$q=ky \tag{3.19}$$

where k is the stiffness of the foundation and y the deflection of the beam (Winkler, 1872). In 1946, Hetenyi, addressed the problem of the elastic stability of a straight beam on an elastic foundation (Winkler foundation). If a straight beam undergoes purely axial compressive force of increasing amplitude, at some critical value of the load, a sudden lateral deflection (buckling) of the beam will occur, as shown in Figure 3.9.

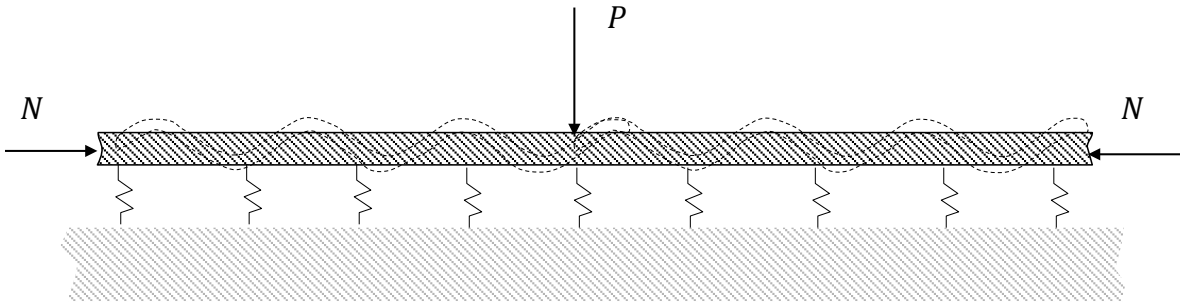

Figure 3.9: Schematic illustration of a beam on elastic foundation undergoing critical buckling load.

The critical values of the axial compressive force can be derived from the deflection equation for a beam on an elastic foundation, assuming that the structural element is under simultaneous axial and transverse forces (Hetényi, 1971). The equation of the deflection line of an infinitely long beam undergoing axial compressive force N and a transverse force P is:

$$y = \frac{P}{2k}\frac{\lambda^2}{ab}e^{-ab}(a\cos ax + b\sin ax)$$
$$a = \sqrt{\sqrt{\frac{k}{4EI} + \frac{N}{4EI}}} \quad , \quad b = \sqrt{\sqrt{\frac{k}{4EI} - \frac{N}{4EI}}} \tag{3.20}$$
$$\lambda^2 = \sqrt{\frac{k}{4EI}}$$

where k is the stiffness of the elastic foundation, E and I are the Young's modulus and the second moment of area of the backing material of the damping tapes. From equation (3.20) as we set $ab=0$ we obtain the critical buckling load of unlimited length and axially loaded beams (Hetényi, 1971):

$$\sqrt{\frac{k}{4EI} - \left(\frac{N_{cr}}{4EI}\right)^2} = 0$$
$$N_{cr} = 2\sqrt{kEI} \tag{3.21}$$

and the frequency of the buckling is given by:

$$n = \frac{1}{\pi}\sqrt{\frac{k}{EI}} \tag{3.22}$$

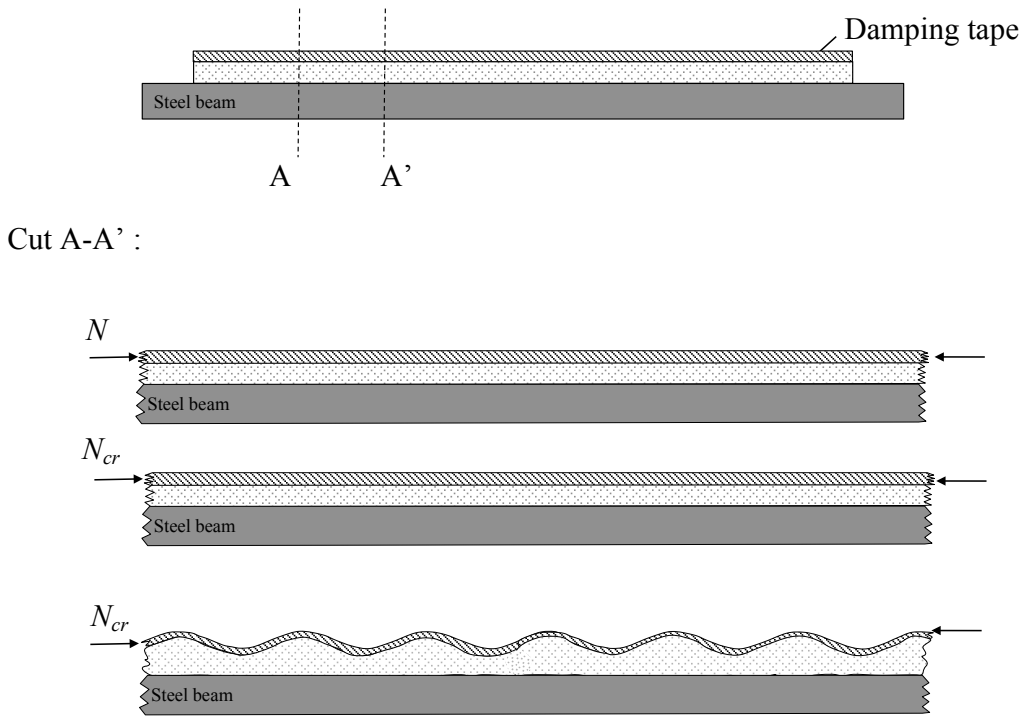

Figure 3.10: Schematic of buckled configuration of the damping tape with transverse load and normal critical load.

The BoEF formulation and Hetenyi approach allows for estimating the critical load or deformation to which the beam has to be subjected in order to induce buckling of the constraining layer of the damping tape, as shown in Figure 3.10. From equation (3.21) we obtain the critical buckling load, N_{cr}, and the corresponding axial stress over the cross section of the damping tape as:

$$\sigma_c = \frac{N_{cr}}{A_c} \tag{3.23}$$

where A_c is the area of the cross section of the backing layer of the damping tape. Equation (3.23) can be related to the normal stress imposed on the beam, and to the strain to which the

beam is subjected. This is necessary since the available experimental resources will only allow measuring strain at the outer fibers of the beam and not directly from the backing material. Experimental details will be covered in the following chapters.

Based on strength of materials concepts, we consider the cross sections of a cantilever beam with damping tapes on each side, as shown in Figure 3.11. Notice that, to obtain the stress to which the beam is subjected, it is necessary to consider the distance of the backing layer to the neutral axis.

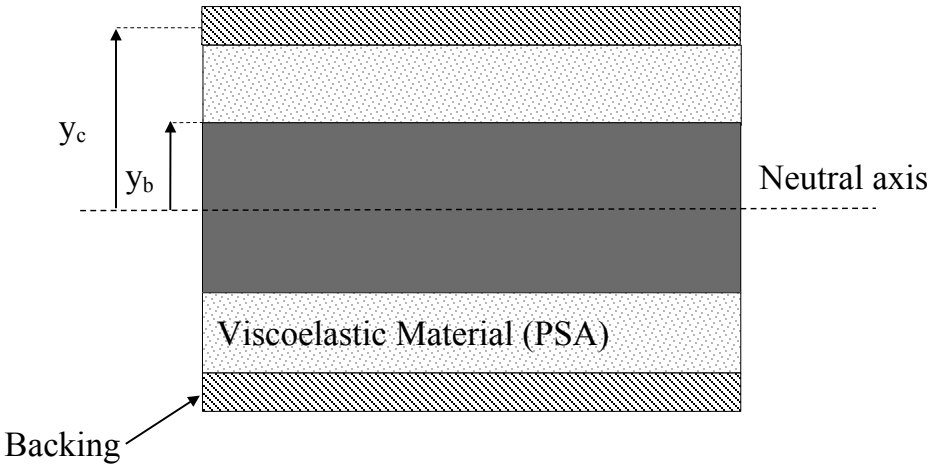

Figure 3.11: Symmetric cross section of a cantilever beam with damping tape applied to both sides.

Under bending loads, longitudinal elements of the beam are subjected to axial tension or compression loads, so we can use the stress-strain relation for the material to determine the stress from the strain or *vice versa*. The stress acting over the beam and damping tapes varies in intensity depending upon the moduli of the materials and the dimensions of the cross section.

The most common stress-strain relationship in engineering is the equation for a linearly elastic material. For such materials, Hooke's law for uniaxial stress is (Gere & Goodno, 2009):

$$\sigma = E\varepsilon = -E\kappa y \tag{3.24}$$

where, E, is the Young's modulus of the considered cross section, κ is the curvature of the beam, and y is the distance from the neutral axis. Equation (3.24) shows that the normal stress acting on the cross section of the beam varies linearly with the distance y from the neutral axis. The stress distribution is illustrated in Figure 3.12.

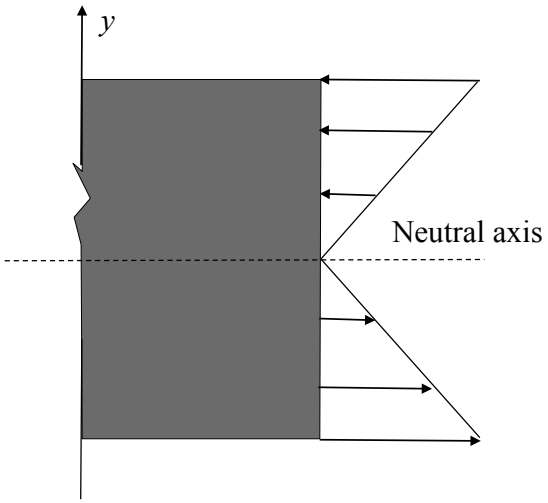

Figure 3.12: Side view of beam showing distribution normal stresses.

The critical strain, ε_{cr}, is calculated from equation (3.24):

$$\varepsilon_{cr} = \frac{N_{cr} y_b}{A_c E_b y_c} \tag{3.25}$$

This strain is at a distance x_1 from the clamped end of the beam. On experimental beams with surface treatments, the strain will be measured at another x_2 distance, as shown in Figure 3.13.

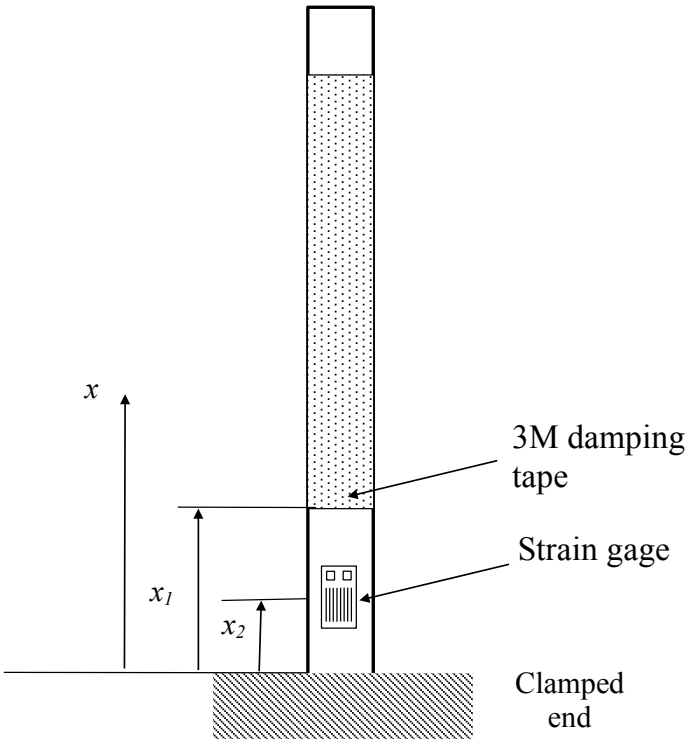

Figure 3.13: Strain measurement distance of a cantilever beam.

To obtain the value of the critical strain detected by the strain gage located at a distance x_2 consider a cantilever beam undergoing harmonic motion at its first vibration mode and the strain distribution along the length of the beam as shown in Figure 3.14.

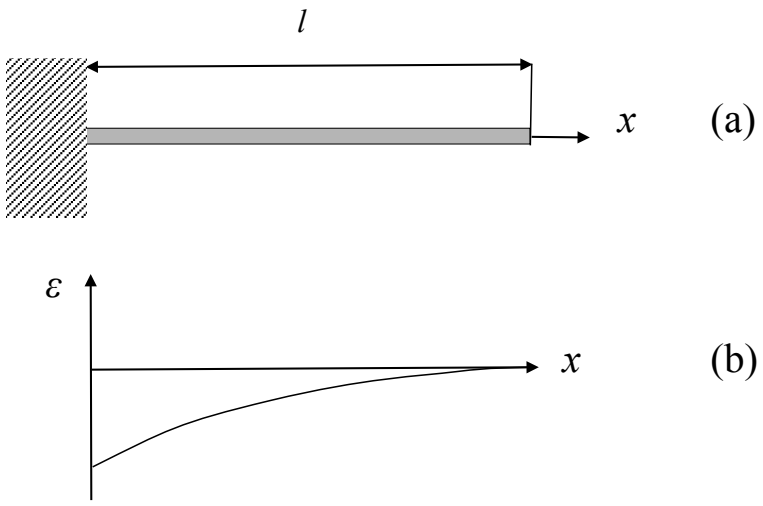

Figure 3.14: Schematic of cantilever beam: a) length of the cantilever beam. b) strain distributions of cantilever beam at its first vibration mode.

The axial strain distribution along the *x* direction of a beam is given by:

$$\varepsilon = -\frac{y}{2}\frac{d^2y(x,t)}{dx^2} \tag{3.26}$$

where, $\frac{d^2y(x,t)}{dx^2}$ is the curvature of the beam. We can replace the curvature of the beam by the mode shape, $\phi_1(x)$, at the fundamental mode:

$$\phi_1(x) = A_r\left(\sin\beta_1 x - \sinh\beta_1 x - \frac{\sin\beta_1 L + \sinh\beta_1 L}{\cos\beta_1 L + \cosh\beta_1 L}\left(\cos\beta_1 x - \cosh\beta_1 x\right)\right) \tag{3.27}$$

$$\beta_1 = 1.875$$

Taking derivatives twice of equation (3.27) to obtain an expression for the curvature of the cantilever beam:

$$\phi_1''(x) = -\beta_1^2 A_r \left(\sin\beta_1 x + \sinh\beta_1 x + \frac{\sin\beta_1 L + \sinh\beta_1 L}{\cos\beta_1 L + \cosh\beta_1 L}\left(\cos\beta_1 x + \cosh\beta_1 x\right) \right) \tag{3.28}$$

From equation (3.26) and the critical value of the strain from equation (3.25), the strain is:

$$\varepsilon = \frac{y}{2}\left(\beta_1^2 A_r \left(\sin\beta_1 x + \sinh\beta_1 x + \frac{\sin\beta_1 L + \sinh\beta_1 L}{\cos\beta_1 L + \cosh\beta_1 L}\left(\cos\beta_1 x + \cosh\beta_1 x\right) \right) \right) \tag{3.29}$$

and, A_r can be obtained evaluating equation (3.29), with the critical value of the strain at x_1:

$$A_r = \frac{2\varepsilon_{cr}}{y} \frac{1}{\left(\beta_1^2 \left(\sin\beta_1 x_1 + \sinh\beta_1 x_1 + \frac{\sin\beta_1 L + \sinh\beta_1 L}{\cos\beta_1 L + \cosh\beta_1 L}\left(\cos\beta_1 x_1 + \cosh\beta_1 x_1\right) \right) \right)} \tag{3.30}$$

Once A_r is obtained, equation (3.29) can be used to determine the critical strain measured at the position of the strain gages on the experimental beam. This approach will be used in Chapter 6 to obtain numerical values of the critical strain values, as for the experimentally parametrically excited cantilever beams considered in Chapter 5. The numerical values will be shown in Chapter 6 and compared to visual data gathered during the parametric excitation experiment of Chapter 5.

3.6 Summary

We presented analytical tools to analyze the end effect responsible for increased damping of the system with a discretized damping layer compared to the continuous damping layer considered by Kerwin in 1959. To achieve this, the approach followed was based on the Plunkett and Lee analysis (Plunkett & Lee, 1970). The nondimensional shear stress of an element of the discretized layer was plotted in Figure 3.5. As the length of the element decreased, the element undergoes more shear stress and therefore more shear deformation, increasing the damping of the system. But as the element becomes shorter, the constraining layer does not offer enough constraint to the VE layer so the total damping of the system decreases. The case of a cantilever beam vibrating in its first mode was studied and plots of shear stress distribution and energy

dissipation along the length of the beam were shown in Figure 3.6 and Figure 3.7, respectively. It was shown by Plunkett and Lee that the discretized damping layer enhanced the energy dissipation compared to a continuous damping layer when the discretization length was near the optimal value, but as the length of the segments decreases, the end effect caused by the shear deformation becomes less important, resulting again in lower damping. The relation of this phenomenon to the shear lag distance from Volkersen's analysis was investigated obtaining that the optimal values of the length of segments were 3.28 times the shear lag distance (Parfitt, 1962) (Plunkett & Lee, 1970). Additionally, we presented the BoEF analysis to predict the critical bending strain at which the backing material of the damping tape might suffer sudden lateral deflection (buckling) that will be considered in the analysis performed in Chapter 6 (Hetényi, 1971).

Chapter 4 Effect of Discretization Length of Constraining Tape on Damping Ratio of a Cantilever Beam

The effects of the length of the constraining tape on the damping ratio of cantilever beams are determined. The experimental setup and a description of the used cantilever beams and damping tapes are presented. Variations in the damping ratio with the discretized damping layer are determined. The Plunkett and Lee approach (Plunkett & Lee, 1970) and concepts of vibrations and strength of materials are used to compare experimental results with analytical predictions.

4.1 Methodology for experimental calculation of damping ratio of cantilever beams

In Chapter 3, the end effect that allows the constrained damping layer to dissipate more energy by means of additional shear deformation and the optimal discretization length to obtain maximum damping without adding extra damping layers were determined. This was done based on the analytical analysis of Plunkett and Lee (Plunkett & Lee, 1970). In this chapter we include an experimental comparison of this theory applied to several cantilever beams and different damping tapes geometries. In order to determine the damping ratio of cantilever beams, shown in Figure 4.1a, we use the logarithmic decrement of the free response as shown in Figure 4.1b.

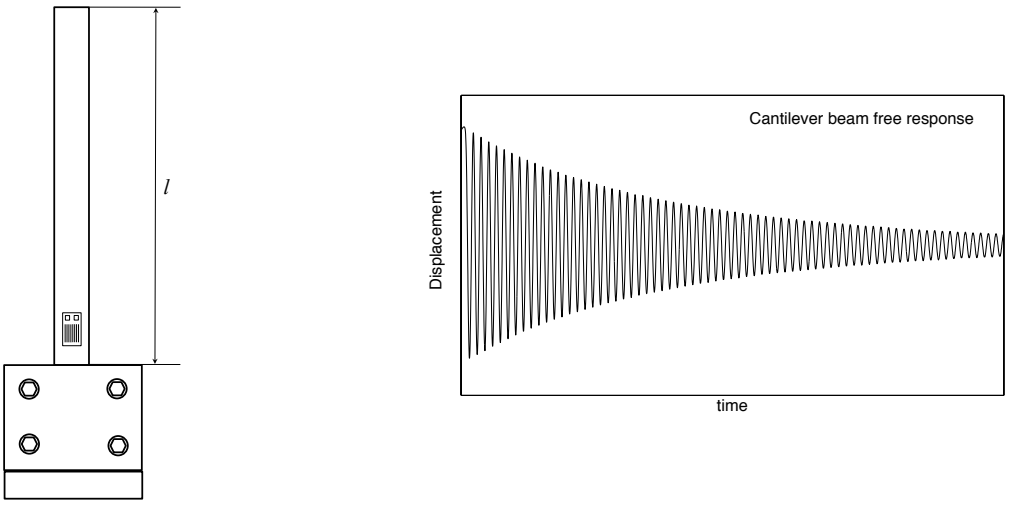

(a) (b)

Figure 4.1: a) Cantilever beam diagram. b) Free response of a cantilever beam.

4.1.1 Logarithmic decrement method

The logarithmic decrement method is used to measure damping in the time domain. In this method, the free vibration displacement amplitude history of a system subjected to an initial displacement is measured and recorded. A typical decay curve is shown in Figure 4.1b. The larger the damping, the greater the rate of decay is. The underdamped free response for the initial condition $x(0) = x_0$ is given by:

$$x = Xe^{-\zeta\omega_n t}\sin(\sqrt{1-\zeta^2}\,\omega_n t + \phi) \tag{4.1}$$

where, X is the amplitude of the response, ω_n is the natural frequency at the *n-mode*, and ζ is the damping ratio. The damping ratio ζ is defined as:

$$\zeta = \frac{c}{c_{cr}} \tag{4.2}$$

where, c is the viscous damping coefficient and c_{cr} is the critical damping coefficient. And the phase angle, ϕ is defined as:

$$\phi = \tan^{-1}\left[\frac{x_0 \omega_d}{\omega_n \zeta x_0}\right] \tag{4.3}$$

From this formulation, the logarithmic decrement is determined. It is defined as the natural logarithm of the ratio of any two successive amplitudes. The expression for the logarithmic decrement is:

$$\Delta = \ln\frac{x(t_i)}{x(t_i + T_d)} = \ln\frac{x_i}{x_{i+1}} = \frac{e^{-\zeta\omega_n t_1}\sin(\sqrt{1-\zeta^2}\,\omega_n t_1 + \phi)}{e^{-\zeta\omega_n t_1 + T_d}\sin(\sqrt{1-\zeta^2}\,\omega_n (t_1 + T_d) + \phi)} \tag{4.4}$$

where T_d is the damped period of the oscillation; and x(ti) = xi is the peak of the oscillation at a time ti as shown in Figure 4.2. Because the values of the sine are equal when time is increase by the same period Td, the preceding relation reduces to (Thomson, 1996):

$$\Delta = \frac{2\pi\zeta}{\sqrt{1-\zeta^2}} \tag{4.5}$$

Also, using the first undamped natural frequency of the system, ω_1, we calculate the linear damping for the first mode, which is given by:

$$\mu_1 = \zeta\omega_1 \tag{4.6}$$

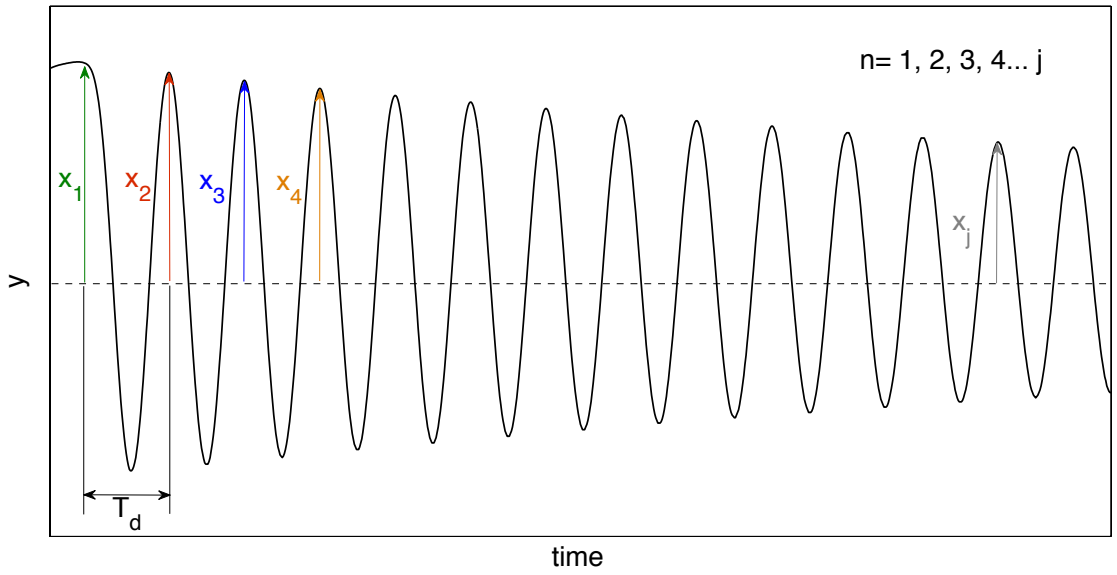

Figure 4.2: Logarithmic decrement diagram of the current methodology.

4.1.2 Experimental beams and damping tapes

The damping tapes used in the thesis are commercial damping tapes produced by 3M. A summary of the geometry and composition of the tapes used in the samples is presented in Table 4.1. All of these damping tapes reportedly have the same adhesive formula. Therefore, the following calculations considered the properties of 3M 425 damping tapes as obtained in Chapter 2.

Table 4.1: Characteristics of the damping tapes

	3M 425	*3M 431*	*3M 3369*
Backing	Dead soft aluminum	Dead soft aluminum	Dead soft aluminum
Adhesive	Acrylic	Acrylic	Acrylic
Backing thickness [mm]	0.07	0.05	0.028
Adhesive thickness [mm]	0.05	0.03	0.033
Total thickness [mm]	0.012 ± 0.001*	0.08 ± 0.008*	0.061 ± 0.004*

Source: (3M, 2012a), * Experimentally measured with micrometer.

We used several different geometries of the beams and damping tapes. These included different material, thicknesses, widths and materials of beams in order to have data over a broad range of damping layer lengths and beams' frequencies. The geometric characteristics of the samples are presented in Table 4.2

Table 4.2: Geometric and material properties of beams used for testing the damping tapes

	Material	*Density* [kg/m^3]	*Young's modulus* [GPa]	*Total length* [mm]	*Adhesive length* [mm]	*Thickness* [mm]	*Width* [mm]
Beam 1	6061 Aluminum	2700	69	207	180	1.5	13
Beam 2	6061 Aluminum	2700	69	450	383	3.0	19
Beam 3	1095 Carbon steel	7850	200	450	383	3.0	13
Beam 4	1095 Carbon steel	7850	200	270	200	0.85	13

4.1.3 Experiment test configuration

The experimental setup is presented in Figure 4.3. Two strain gages mounted on both sides were used in order to measure the strain at the base of the beam. Once experimental data was taken from the beam without surface treatment, two constrained damping layers were bonded in place, one on each side of the beam. After testing with continuous length treatments these layers were then discretized into regular intervals in order to compare the damping ratio of different segment lengths.

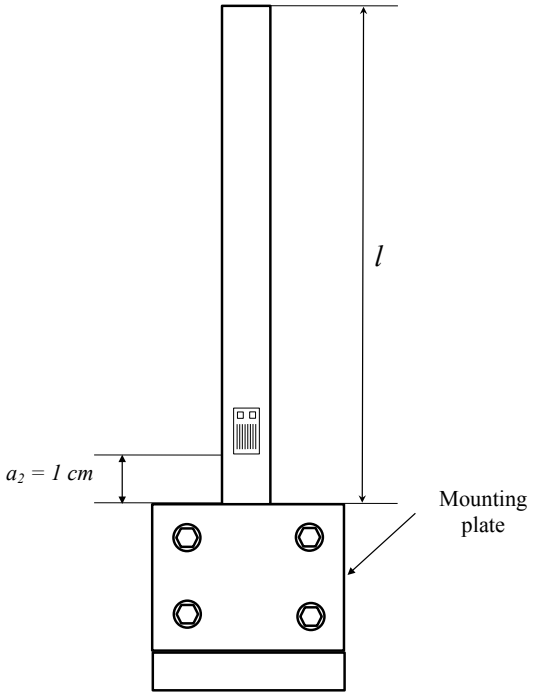

Figure 4.3: Schematic of the position where the strain gages were bonded to the experimental cantilever beams.

To measure the amplitude decay of beam's vibration, we recorded the strain which is defined as the fractional change in length:

$$\varepsilon = \frac{L - L_0}{L_0}$$

Figure 4.4 shows the concept of a strain gage: when the beam deforms, the foil of the gage experiences a change in resistance, which can be detected by the Wheatstone bridge. Then, using the gage factor (GF) of the strain gage and the differential voltage due to the change of resistance, we determine the strain of the beam. The gage factor, GF, is the dimensionless ratio of the fractional change in resistance to the fractional change in length along the axis of the strain gage. For our experimental samples, the magnitudes of the strains were very small; therefore, strain is expressed as microstrain (με) or millistrain (me). We bonded the strain gages near the

clamped end in order to maximize sensitivity during the free vibrations tests (Hannah & Reed, 1992).

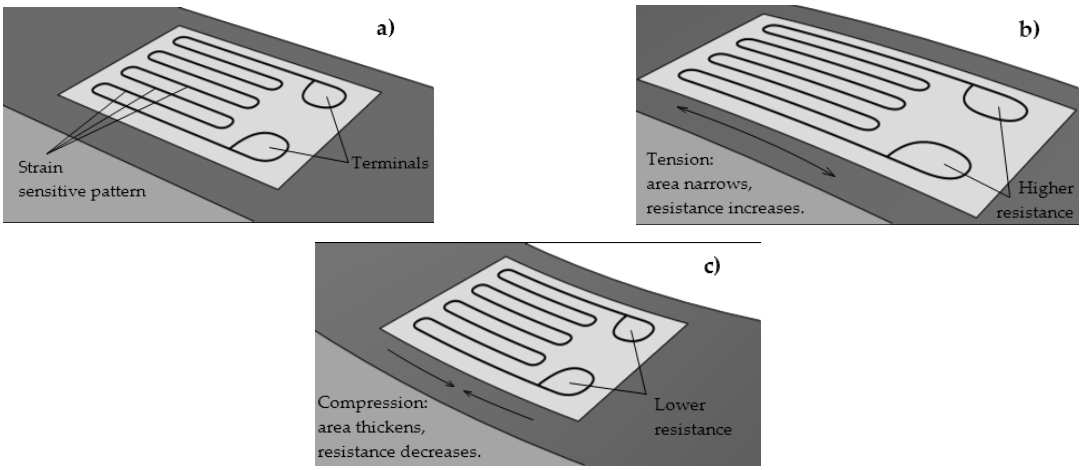

Figure 4.4: Representation of the working concept of a strain gage on a beam under bending. Source: Diagram by Izantux/CC0 1.0 URL: http://upload.wikimedia.org/wikipedia/en/4/40/StrainGaugeVisualization.png Used under fair use, 2014.

Table 4.3: Strain gages used in the beams to record the strain amplitude decay.

Model		*Gage Factor*	*Resistance*	*Sample**
EA-06-250AE-350	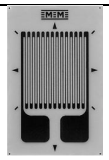	2.095	350 Ω	1, 2, 3
WK-06-125AD-350	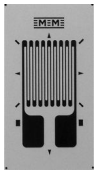	2.02	350 Ω	4, 5

*See Table 4.2. Source: Micro-Measurements. "Precision Strain Gages and Sensors." edited by Vishay Precision Group, 2010. URL: http://www.vishaypg.com/docs/50003/precsg.pdf Used under fair use, 2014.

To bond the strain gages we used the M-Bond kit from Micro Measurements at the position showed in Figure 4.3. The procedure for gage application is given by the manufacturer (Micro-Measurements, 2011) and includes the following steps:

1. Thoroughly degrease the gaging area with the solvent, CSM-1 Degreaser.
2. Proceed with dry abrading using a 320 grit silicon carbide paper, followed by wet abrading using a 400 grit silicon carbide paper wetted with M-Prep Conditioner A.
3. Mark with a pencil the area where the strain gage will be placed and clean with more M-Prep Conditioner A and M-Prep Neutralizer. The final chemical should be removed by a single wiping motion to avoid redepositing contaminants.
4. Use tweezers to remove the gage from the mylar envelope and place the gage on the gage box surface with the bonding side down.
5. Place 4 to 6 in of Micro measurements No. PCT-2A cellophane tape over the gage area and position the strain gage following the marks of step 3.
6. Finally, carefully remove the tape with the strain gage and apply M-Bond 200 catalyst to the bonding surface and add a drop of the M-Bond 200 adhesive one centimeter from the edge of the bonding area.
7. Apply pressure for 1 to 2 minutes until the M-Bond 200 adhesive cures.
8. Remove the cellophane tape.

Front Back

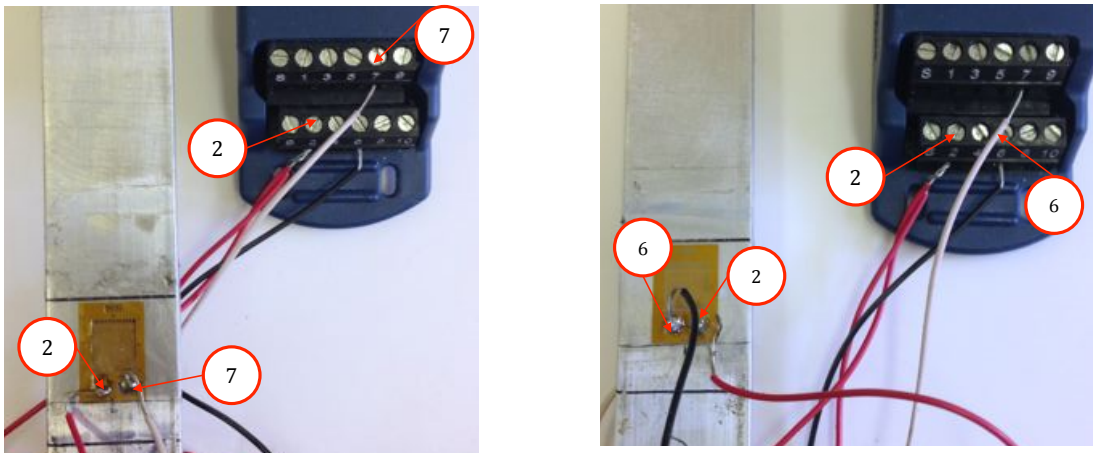

(a) (b)

Figure 4.5: Wiring configuration for the half bridge circuit on the beam type 2 with no constrained damping tapes applied.

After the strain gage is bonded to the sample, the corresponding wires are connected to the data acquisition system (DAQ) to complete a half bridge circuit. As such, we are able to convert the analog signal obtained from the strain gages into digital values. The connection between the DAQ and the strain gages is shown in Figure 4.5. The numbers in Figure 4.5 correspond to the channel used in the DAQ and the LabVIEW software. For the half bridge circuit, two active strain gages are required, one is positioned in the direction of the bending strain on one side of the sample (front) and the other is positioned in the direction of the bending strain on the opposite side of the sample (back); the strain gages are expected to experience equal and opposite strains, which are effectively added when used in adjacent arms of the Wheatstone bridge. We calculate the strain from strain gage using the gage coefficient and the equation for a half bridge circuit,

$$\varepsilon = \frac{-2V_r}{GF}\left(1+\frac{R_L}{R_S}\right)$$

where R_L is the lead resistance; R_g is the resistance of the strain gages; GF is the gage coefficient, V_r is the relation between the excitation and measured voltage given by:

$$V_r = \left[\left(V_{CH} / V_{EX} \right)_{strained} - \left(V_{CH} / V_{EX} \right)_{unstrained} \right]$$

where, V_{CH} is the differential voltage detected due to the elongation of compression of the strain gage and V_{EX} is the exaction voltage. Both are shown in Figure 4.6.

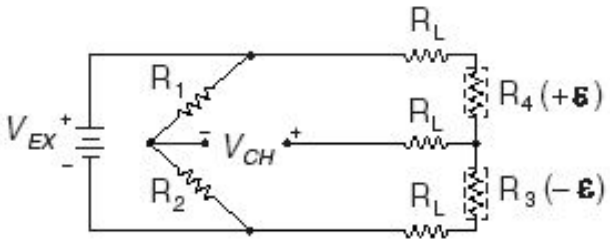

Figure 4.6: Wire diagram of the half bridge circuit used to detect the strain from the tested samples. (National-Instruments, 2006)

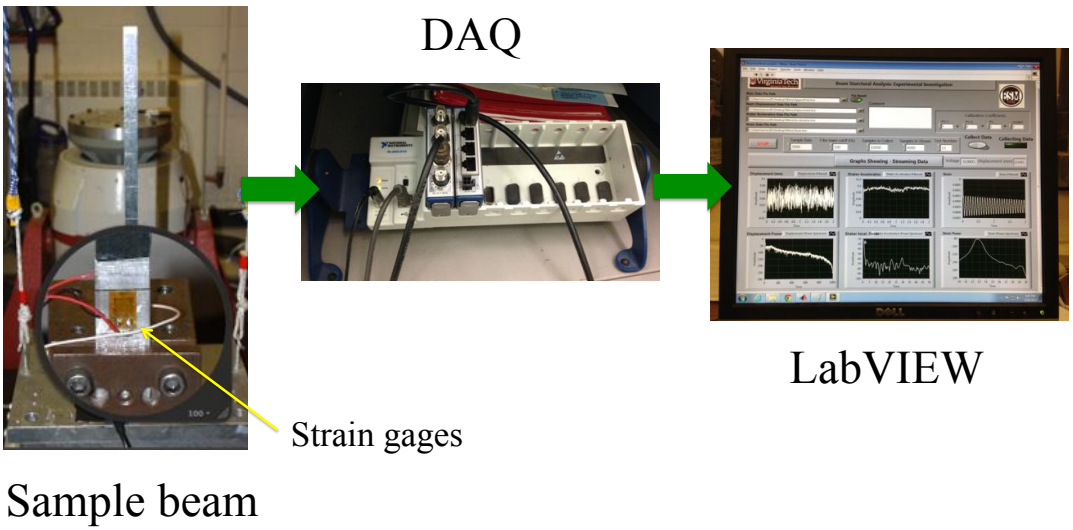

Figure 4.7: DAQ set up for recording the strain amplitude decay of the samples

4.1.4 Experimental procedure for the cantilever beams

This section includes the procedure for conducting free vibrations testing of the cantilever beams with and without the surface treatments. The first step was to mount the beam without the damping layers at the clamped end, as shown in Figure 4.8. We used a mounting plate with four screws to secure the beam.

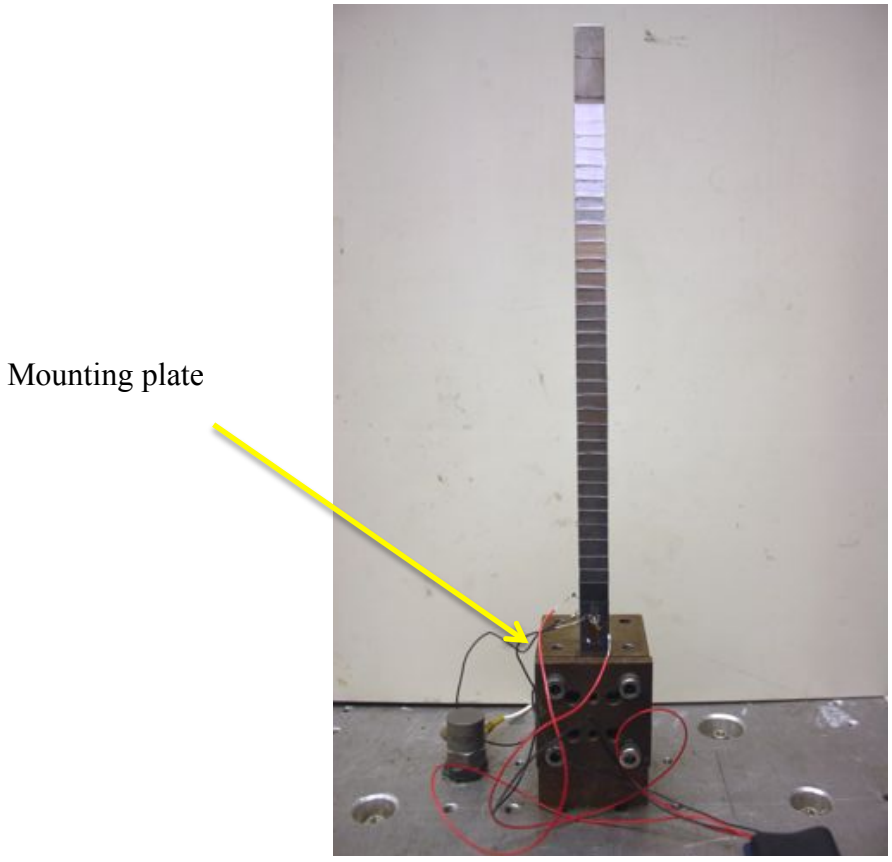

Figure 4.8: Beam 3 on the mounting plate ready for free vibration testing to measure the damping ratio.

To carry out the free response tests of the beams, we applied an initial displacement of 0.5 cm at the tip of the beam and recorded the strain amplitude decay. Then, using equations (4.4) and (4.5) we calculated the damping ratio of the cantilever beams tested. After bare beams were tested, continuous layers of damping tapes were adhered to both sides of the beams, as shown in Figure 4.9a. Then, we discretized (cut) the damping tapes at regular intervals, as shown in Figure 4.9. All discretization was performed such that the constrained damping tapes were symmetric

on both sides of the beams. With the free response recorded, the damping ratios for each discretized configuration were calculated. The results are shown in section 4.2.

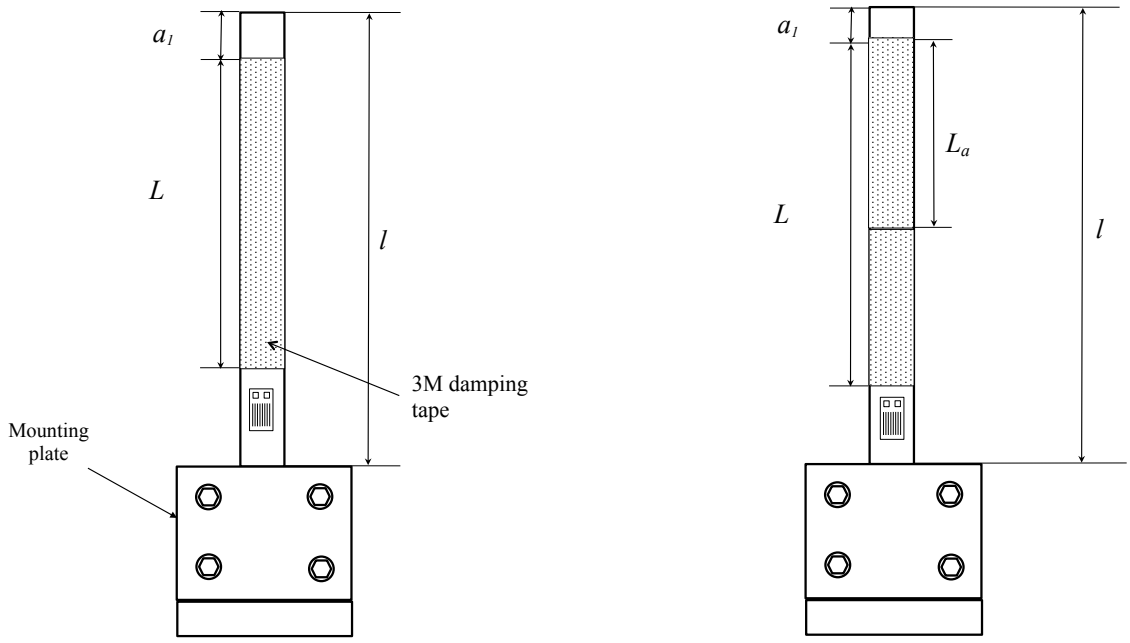

(a) (b)

Figure 4.9: Schematic illustration of a cantilever beam with a: a) Continuous-damping layers. b) Discretized damping layers (2 segments are shown).

4.2 Results of damping ratio measurements for different beams and damping tape configurations

Typical results obtained for cantilever beams during free vibration tests are shown in Figure 4.10, showing that the log decrement stabilizes quickly to a consistent value. Then, from the experimentally determined log decrement values, we calculated values of damping ratio for the tested beams using equation (4.5). The results of the damping ratio for each configuration are shown in Figure 4.11 to Figure 4.14.

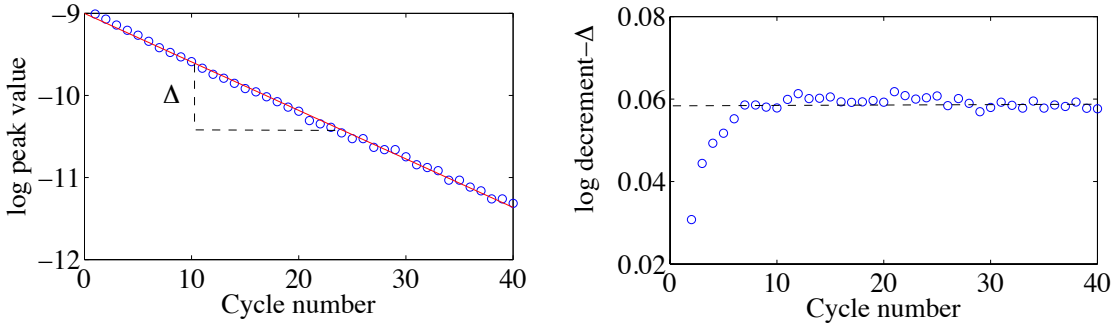

(a) (b)

Figure 4.10: Typical results obtained from free vibration tests of a cantilever beam with the damping layers. a) logarithm of the peak value vs. cycle number. b) logarithmic decrement vs. cycle number.

(a)

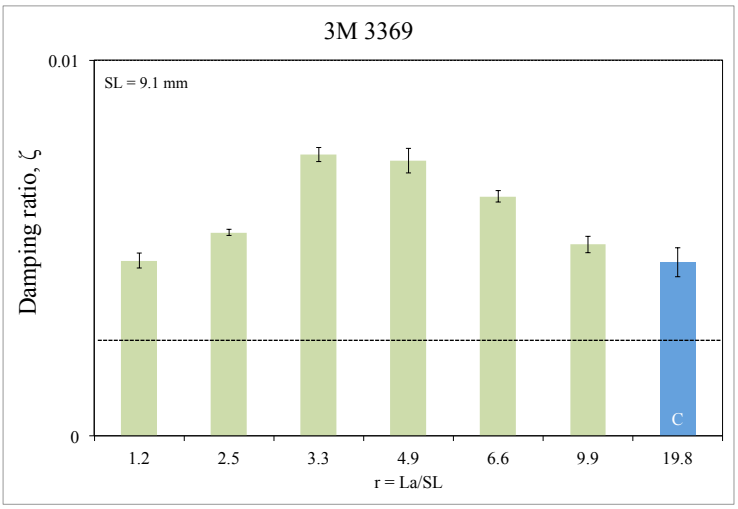

(b)

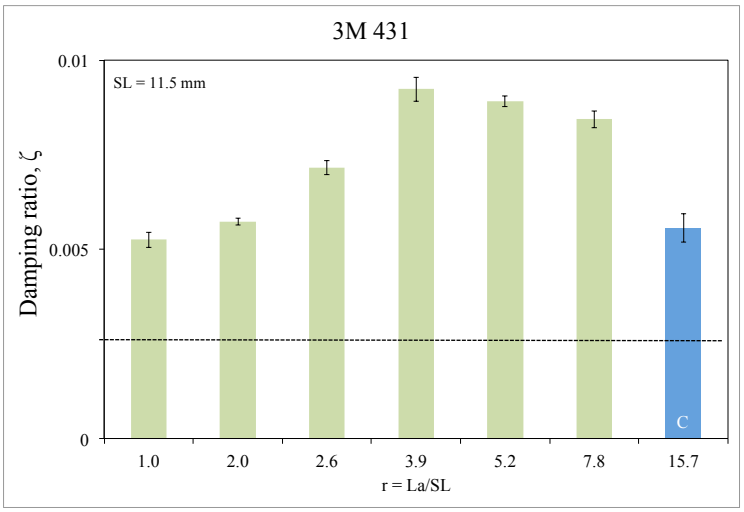

(c)

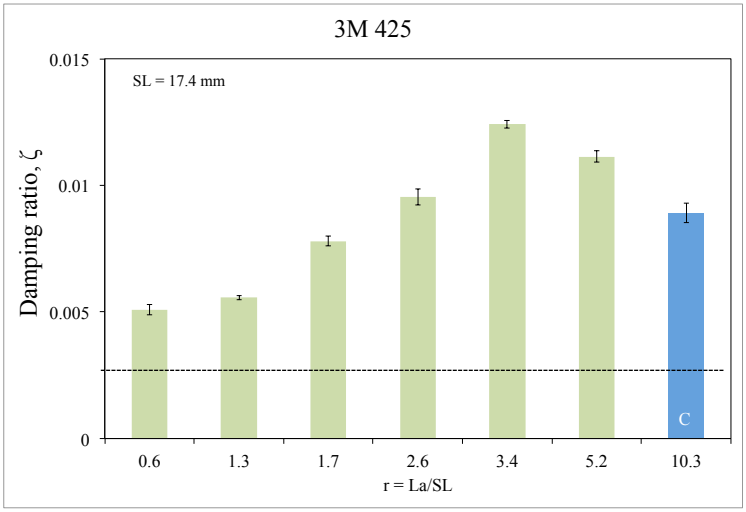

Figure 4.11: Experimental damping ratio for beam 1 with: a) 3M 3369 damping tape b) 3M 431 damping tape c) 3M 425 damping tape. Note: Dashed lines represent the damping ratio of the bare beam 1 without damping tapes and blue bars correspond to ζ measured for the continuous surface treatment.

(a)

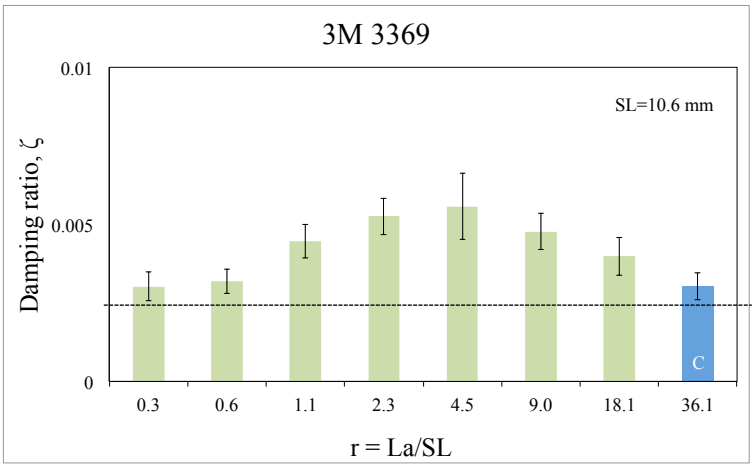

(b)

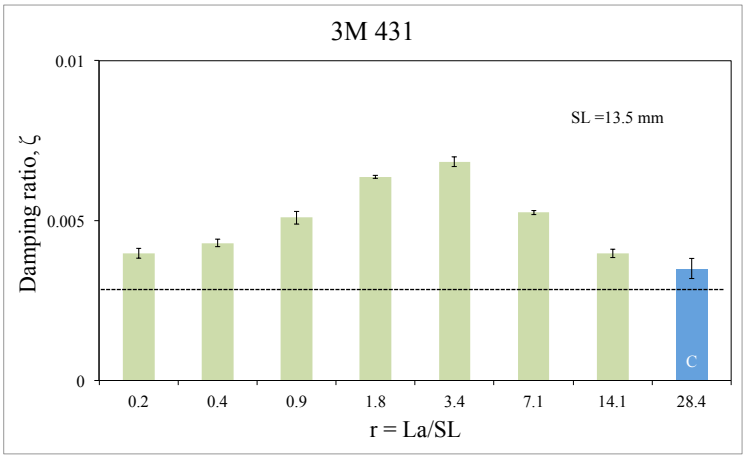

(c)

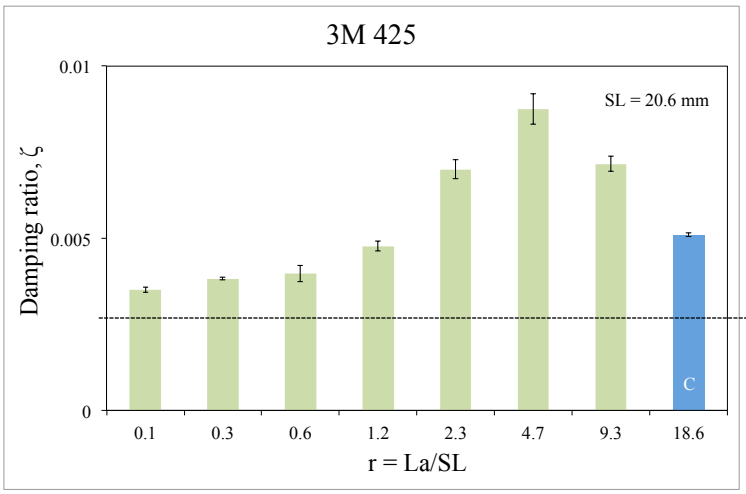

Figure 4.12: Experimental damping ratio for beam 2 with: a) 3M 3369 damping tape b) 3M 431 damping tape c) 3M 425 damping tape. Note: Dashed lines represent the damping ratio beam 2 without damping tapes and blue bars correspond to ζ measured for the continuous surface treatment.

(a)

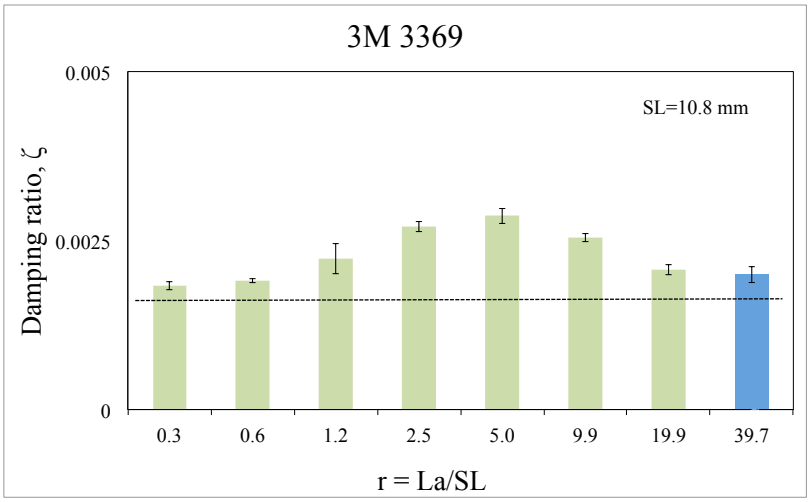

(b)

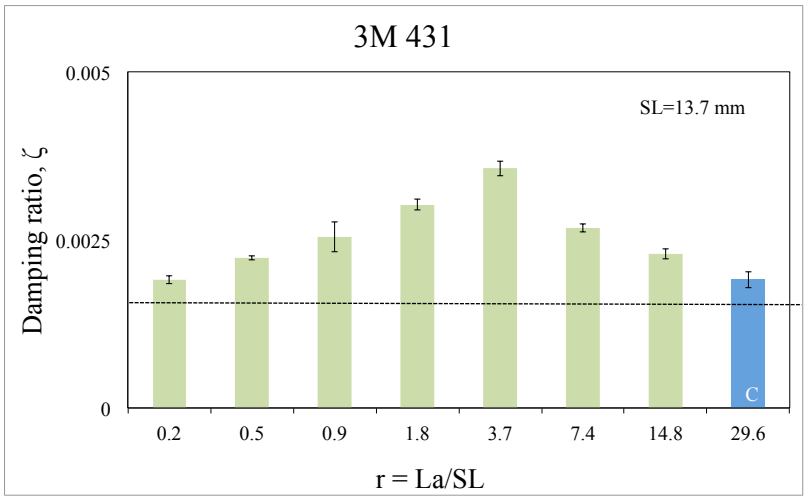

(c)

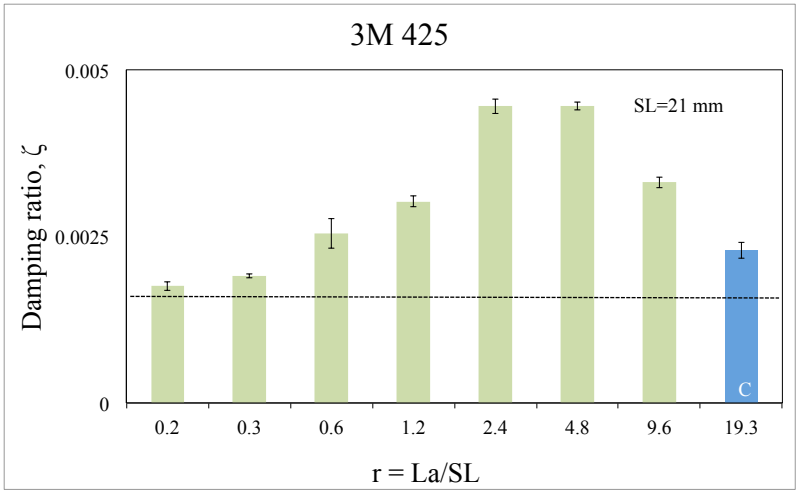

Figure 4.13: Experimental damping ratio for beam 3 with: a) 3M 3369 damping tape b) 3M 431 damping tape c) 3M 425 damping tape. Note: Dashed lines represent the damping ratio beam 3 without damping tapes and blue bars correspond to ζ measured for the continuous surface treatment.

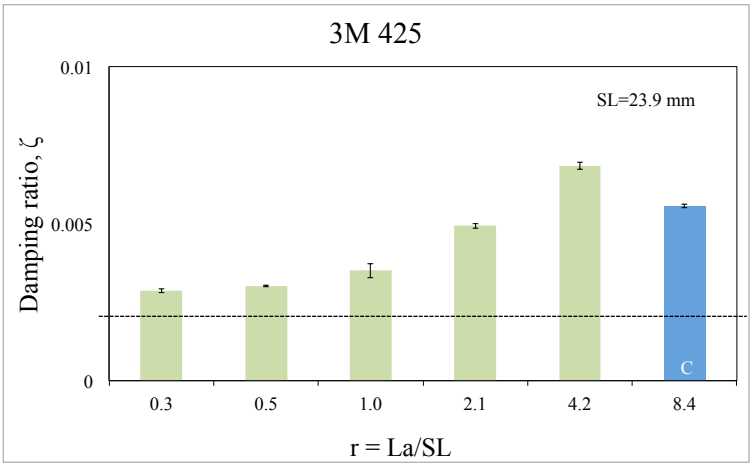

Figure 4.14: Experimental damping ratio for beam 4 with 3M 425 damping tape. Note: Dashed line represents the damping ratio beam 4 without damping tapes and blue bar correspond to ζ measured for the continuous surface treatment.

4.2.1 Percentage increase of the logarithmic decrement of discretized damping layers

The experimental results presented in the previous section showed that discretized damping layers could increase the damping of the tested structures more effectively that the continuous configuration if the discretization length was near the optimal value predicted by Plunkett and Lee (Plunkett & Lee, 1970). Table 4.4 shows the percentage increase in log decrement for the tested samples and damping tapes. We obtained this percentage increment as:

$$\%\Delta = \frac{\Delta_D - \Delta_C}{\Delta_C} \tag{4.7}$$

where, Δ_D is the logarithmic decrement experimentally determined for the discretization length corresponding to the highest measured damping for each beam, and Δ_C is the logarithmic decrement experimentally determined for the continuous damping layer. We calculated the percentage increase of the logarithmic decrement for this discretization length for the different experimental samples using equation (4.7).

Table 4.4: Percentage increase of the logarithmic decrement of discretized damping layer.

Damping tape		*Sample 1* t = 1.5 mm	*Sample 2* t = 3 mm	*Sample 3* t = 3 mm	*Sample 4* t = 0.85 mm
3M 3369	t_a =0.033 t_b =0.028	62%	50%	41%	-
3M 431	t_a =0.03 t_b =0.05	45%	95%	94%	-
3M 425	t_a =0.05 t_b =0.07	40%	88%	81%	23%

t= thickness of the sample, t_a = thickness of the adhesive layer, t_b = thickness of the backing layer.

The results presented in Table 4.4 show that the 3M 431 and 3M 425 damping tapes have the highest percentage of increase with respect to the continuous configuration. We would expect this because the energy dissipated per cycle is a function of the backing material thickness, as found from equation (3.11). For both, 3M 431 and 3M 425 damping tape, the backing material thickness is about two times greater that the thickness of the backing material of 3M 3369 damping tape.

Other material properties also influence the energy dissipated; the viscoelastic material tan δ for different beams changed as shown in Table 4.5. We would expect a significant change in the energy dissipation within different experimental specimens. Beam 4 had the lowest tan δ value, and therefore the percentage increase in log decrement recorded for this beam is the lowest. But, beam 1 had the highest tan δ value and showed a relatively smaller increase than beams 2 and 3. This can be explained because of the length of the initial continuous layer. For beam 1 the initial adhesive layer of adhesive 3M 425 was 183 mm compared to the 383 mm used initially on beams 2 and 3. Calculating the ratio *r* for samples 1 and 2 for 3M 425 damping tape yields:

$r_1 = 10.3$

$r_2 = 18.3$

Both ratios are well above the theoretically determined optimal value of 3.28, so an increase of the damping ratio was expected. But, the ratio r_1 of beam 1 is smaller and closer to the 3.28 value than r_2, we would expect that the increment for beam 2 would be slightly higher. These observations help us to explain the enhancement of the discretized damping layer in comparison of the continuous layer for the experimental samples.

4.3 Comparison of experimental results and the analytical model to calculate damping ratio

The dissipation in the constrained viscoelastic layer cannot be measured directly. We must find it by comparing the energy dissipation of the bare specimen without surface treatment and the energy dissipation of the beam with damping tapes. The energy dissipation of the VE layer is given by:

$$\Delta W_L = \Delta W_s - \Delta W_B \tag{4.8}$$

where ΔW_s is the energy dissipation on the specimen with the damping tapes and ΔW_B is the energy dissipation of the bare beam. For a uniform cantilever beam undergoing steady state or decaying vibration, the damping of the structure can be related to the loss coefficient of the system, η_s by:

$$\eta_S = \frac{\Delta W_L}{2\pi W_S} \tag{4.9}$$

where W_S is the maximum energy stored of the structure, and ΔW_L is the energy dissipated per cycle within the VE layers. To relate the loss coefficient of the experimental beam and equation (3.14), Plunkett and Lee integrated the energy of the system over the length of a segment of the surface treatment (Plunkett & Lee, 1970):

$$
\begin{aligned}
W_L &= 2\int_a^{a+L} \frac{W}{L_a} dx \\
W_L &= 2\int_a^{a+L} \eta_d \frac{W_n}{L_a} dx \\
W_L &= \eta_d \frac{t_b}{4} E_2 t_2 \int_a^{a+L} \left(\frac{d^2 y}{dx^2} \right)^2 dx
\end{aligned}
\tag{4.10}
$$

Additionally, the maximum strain energy per cycle in the system is given by:

$$
W_S = \frac{E_b t_b^3}{24} \int_0^l \left(\frac{d^2 y}{dx^2} \right)^2 dx \tag{4.11}
$$

We consider the case of a cantilever beam subjected to sinusoidal flexural vibration with small deformations, so the strain at the surface of the beam structure is given by:

$$
\varepsilon_0 = -\frac{t_b}{2} \left(\frac{d^2 y}{dx^2} \right) \tag{4.12}
$$

where t_b is the thickness of the beam and d^2y/dx^2 is the curvature of the beam. The loss coefficient of the system is defined by the ratio of equations (4.10) to (4.11)

$$
\eta_S = \eta_d \frac{3E_2 t_2}{\pi E_b t_b} \int_a^{a+L} \left(\frac{d^2 y}{dx^2} \right)^2 \Bigg/ \int_0^l \left(\frac{d^2 y}{dx^2} \right)^2 dx \tag{4.13}
$$

where η_d is the loss coefficient of the damping treatment, as defined in Chapter 3, E_2 and t_2 are the Young's modulus and the thickness of the backing material of the damping tape, E_b and t_b are the Young's modulus and the thickness of the beam, d^2y/dx^2 is the curvature of the beam, and the values of a and L were defined in Figure 4.9a. Replacing the curvature of the beam by the fundamental mode shape and solving equation (4.13) for η_d,

$$\eta = (\eta_S - \eta_B)\frac{\pi E_b t_b}{3E_2 t_2}\int_0^l \left(\frac{d^2y}{dx^2}\right)^2 dx \Big/ \int_a^{a+L}\left(\frac{d^2y}{dx^2}\right)^2 dx \qquad (4.14)$$

where, η_B is the loss coefficient for the beam without damping layers.

4.3.1 Viscoelastic material properties at the experimental frequency and temperature.

The theoretical values of the loss factor for each damping tape configuration and discretization length were determined from equation (3.14) using the master curve, Figure 2.19, of the loss tangent, tan δ. These values are listed in Table 4.5 for the damped natural frequency of the experimental beams from Table 4.2. Table 4.5 also contains the shear modulus of the PSA adhesive, also obtained from the master curve, Figure 2.17. We used these values to predict the shear lag distance (*SL*) and the optimal discretization length from equation (3.5). The room temperature was measured before each test.

Table 4.5: Viscoelastic properties of the PSA tapes at the frequencies of the experimental samples, at the experimental temperature of 22 ± 2 ^{o}C.

			Shear lag distance, SL [mm]			*Optimum length* [mm]		
f [Hz]	$\lvert G^* \rvert$ [MPa]	tan δ	*3M 3369*	*3M 425*	*3M 431*	*3M 3369*	*3M 425*	*3M 431*
29.25	0.76	0.513	9.1	17.4	11.5	29.8	57.2	37.7
12.25	0.56	0.430	10.6	20.6	13.5	34.9	67.6	44.0
13.00	0.54	0.434	10.8	21.0	13.7	35.5	68.9	45.5
9.79	0.45	0.416	12.4	23.9	15.7	40.5	78.4	51.5

4.3.2 Experimental and theoretical loss coefficient values.

Using equation (4.14) we obtained experimental values for the loss coefficient of the system. The values of ηb, were obtained for each beam without the damping treatment, and ηs was calculated for the beam with damping tapes from the damping ratio for several discretization length used in this chapter. Finally, we used the material data from the characterization performed in Chapter 2 for the damping tape 3M 425 and equation (3.14) to plot the theoretical values of the loss coefficient. A list of the properties used for the different beams is presented on Table 4.5. The red dashed lines in Figure 4.15 and Figure 4.16 represent the limit established by the values of the loss coefficients for the beams without damping tapes, and the blue dashed lines represent the theoretically determined loss coefficient below the bare beams' loss coefficients.

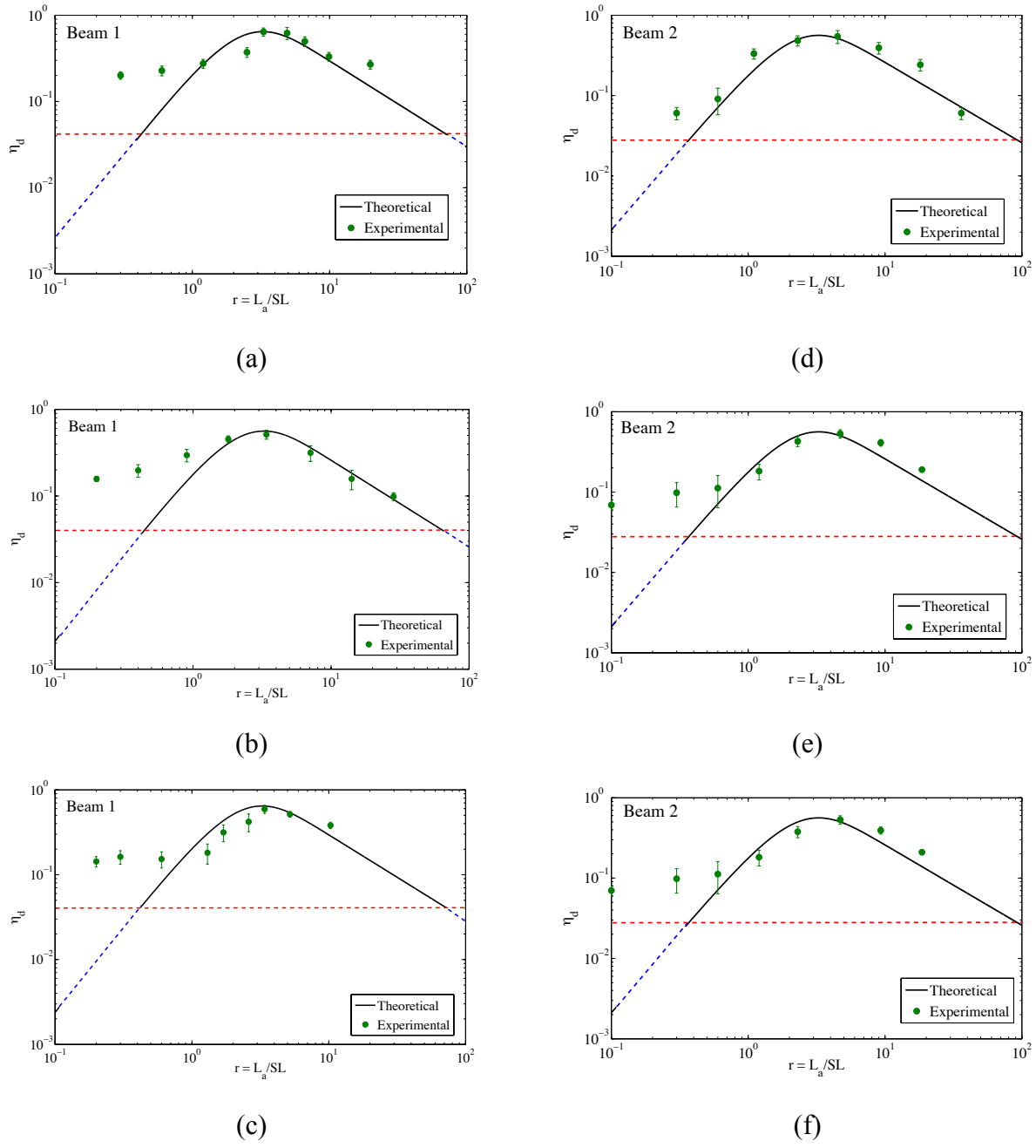

Figure 4.15: Comparison of theoretical and experimental loss coefficient for: a) Beam 1 Tape 3M 3369. b) Beam 1 Tape 3M 431. c) Beam 1 Tape 3M 425. d) Beam 2 Tape 3M 3369. b) Beam 2 Tape 3M 431. c) Beam 2 Tape 3M 425. Note: Values below the red dashed line correspond to the loss coefficient below the loss coefficient the beam without damping tapes.

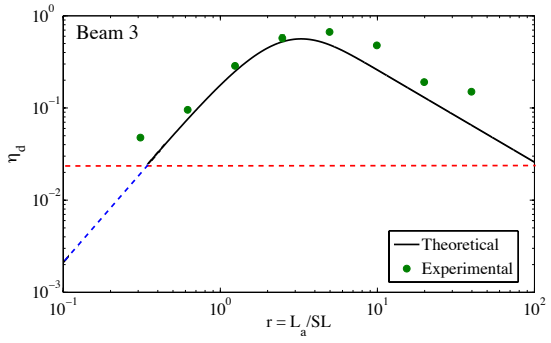

(a)

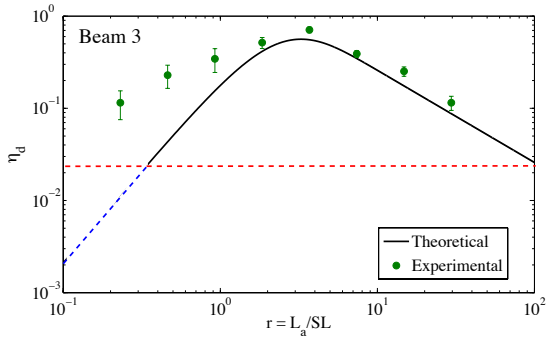

(b)

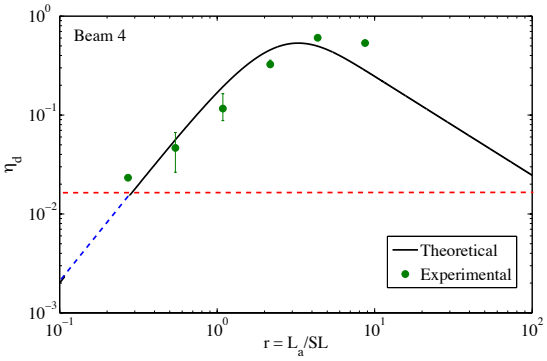

(d)

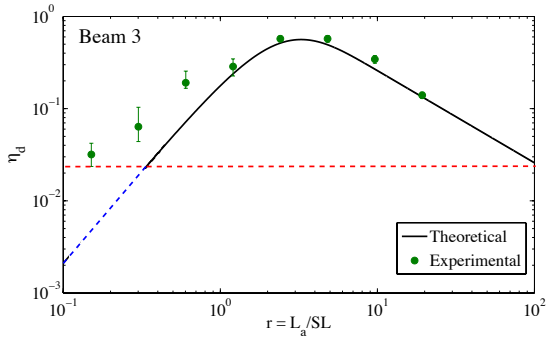

(c)

Figure 4.16: Comparison of theoretical and experimental loss coefficient for: a) Beam 3 Tape 3M 3369. b) Beam 3 Tape 3M 431. c) Beam 3 Tape 3M 425. d) Beam 4 Tape 3M 425. Note: Values below the red dashed line correspond to the loss coefficient below the loss coefficient the beam without damping tapes.

Figure 4.15 and Figure 4.16 show that the experimental results are in agreement with theoretical predictions and with respect to the optimal length of the discretization segments. Notice that as the segment length is decreased, the loss coefficient values increase until this optimal length is reached. For beam 1, beam 2 and beam 3, the theoretical comparison shows a plateau as the length of the segments decreased away from the optimal length. We included in Figure 4.15 and Figure 4.16 values of the loss coefficient of the bare beam and observed that there is a gap between the plateau of the loss coefficients and the bare beams values. This gap may be attributed to the loss coefficient resulting from different experimental factors such as the air drag and structural damping of the beam, and that the expected dissipation is a combination of these mechanisms. Additionally, we explained in Chapter 3 that as the discretization length is decreased, the capability of the constraining layer to induce shear deformation to the viscoelastic layer decreased. Therefore, the damping treatment would be expected to act as an unconstrained viscoelastic layer and the above combination of damping mechanism will be more important as the effectiveness of the constraining layers decreased as shown in Figure 4.17. Unfortunately, the configuration available to test the damping tape with the cantilever beams does not allow us to measure the loss coefficient of the unconstrained damping layer to add this values as comparison.

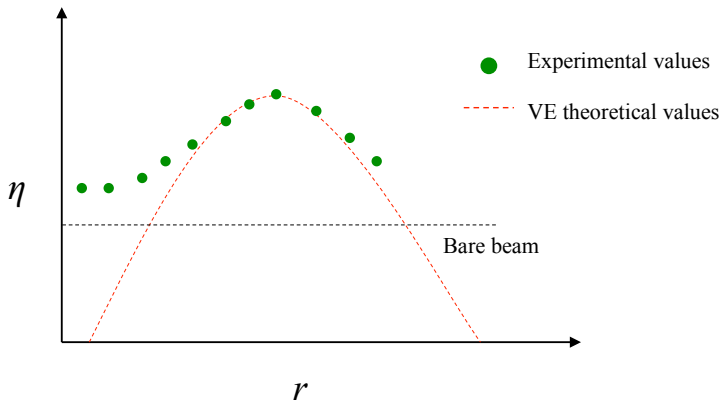

Figure 4.17: Expected experimental system's energy dissipation and VE theoretical energy dissipation.

It is observed that the plateau's behavior is different for each damping tape. For example, Figure 4.15a and Figure 4.15b show different points of separation between the theoretical and experimental values. We observed that the only difference between the damping layers used for these plots is the thickness of the adhesive but the difference it is not as significant, so we cannot attribute this behavior only to this characteristic; therefore, we were unable to analytically predict the separation point at which each damping tape will start varying from the theoretical values. This phenomenon needs to be analyzed more deeply in order to fully understand what causes the separation between the experimental and theoretical but we could observe that this combined effect is limited by the loss coefficient determined for the bare beam case.

Additionally, we observed good agreement between the experimental and the theoretical values in Figure 4.15 and Figure 4.16. The properties used to validate the experimental values (shear modulus), were calculated from equation (2.11), and these properties are functions of the thickness of the damping tape. Many times due to storage conditions or manufacturing procedure variations, thickness may vary, thereby directly affecting the obtained values of damping tapes' properties. The ratio r and the optimal discretization length could thus be affected, causing a shift between the experimental and theoretical values. With the aim to take this into account, in this work we used the manufacturer's thickness specification for each damping tape but these values were also measured with a micrometer and compared to the manufacturer's values.

From Table 4.5, notice that properties of the viscoelastic material are frequency dependent and so, each data set of Figure 4.15 and Figure 4.16 was obtained using the data at the first natural frequency of the beam without damping tape. This was not considered when comparing theoretical and experimental data because of the small shift in the damped frequency recorded, so the error observed on Figure 4.15 and Figure 4.16 could be somehow attributed to this small frequency shift. Later, in section 4.4, we will comment on the effects of the damping tape to the first natural frequency of the beam with damping layers.

We can conclude from this section that the Plunkett and Lee approach offered an accurate method to predict damping of a given beam with discretized damping layers. Also, the Plunkett and Lee approach offered accurate theoretical tools regarding the optimal length at which the damping tapes should be discretized in order to optimize the damping.

4.3.3 Optimization of damping layer length

From results given in section 4.3.2 and considering the good agreement obtained from the Plunkett and Lee approach, the analysis of the discretized constrained damping layers was extended in this section. A theoretical analysis was carried out in order to consider optimization of the damping layer length and reduce the needed length, potentially obtaining an improved damping ratio compared to a continuous damping layer configuration, and with reduced added mass and cost.

In this section our aim is to compare the case of a fully covered cantilever beam and a partially covered cantilever beam as shown in Figure 4.18a and Figure 4.18b, respectively. Notice from Figure 4.18a that the energy dissipated along the length of the beam is concentrated near the clamped end where the bending strains are largest. This was discussed earlier in Chapter 3. Knowing that most of the energy dissipation is happening near the clamped end, consider Figure 4.18b with a shorter length of damping tape. Notice that the effect of the added end within the region of maximum strain could cause a higher damping than the obtained with a fully covered beam. Furthermore, if the selected length of is greater than the optimal discretization length, and this treatment is discretized as shown in Figure 4.18c, we could further increase the damping of the structure with less added mass than required for continuous treatment.

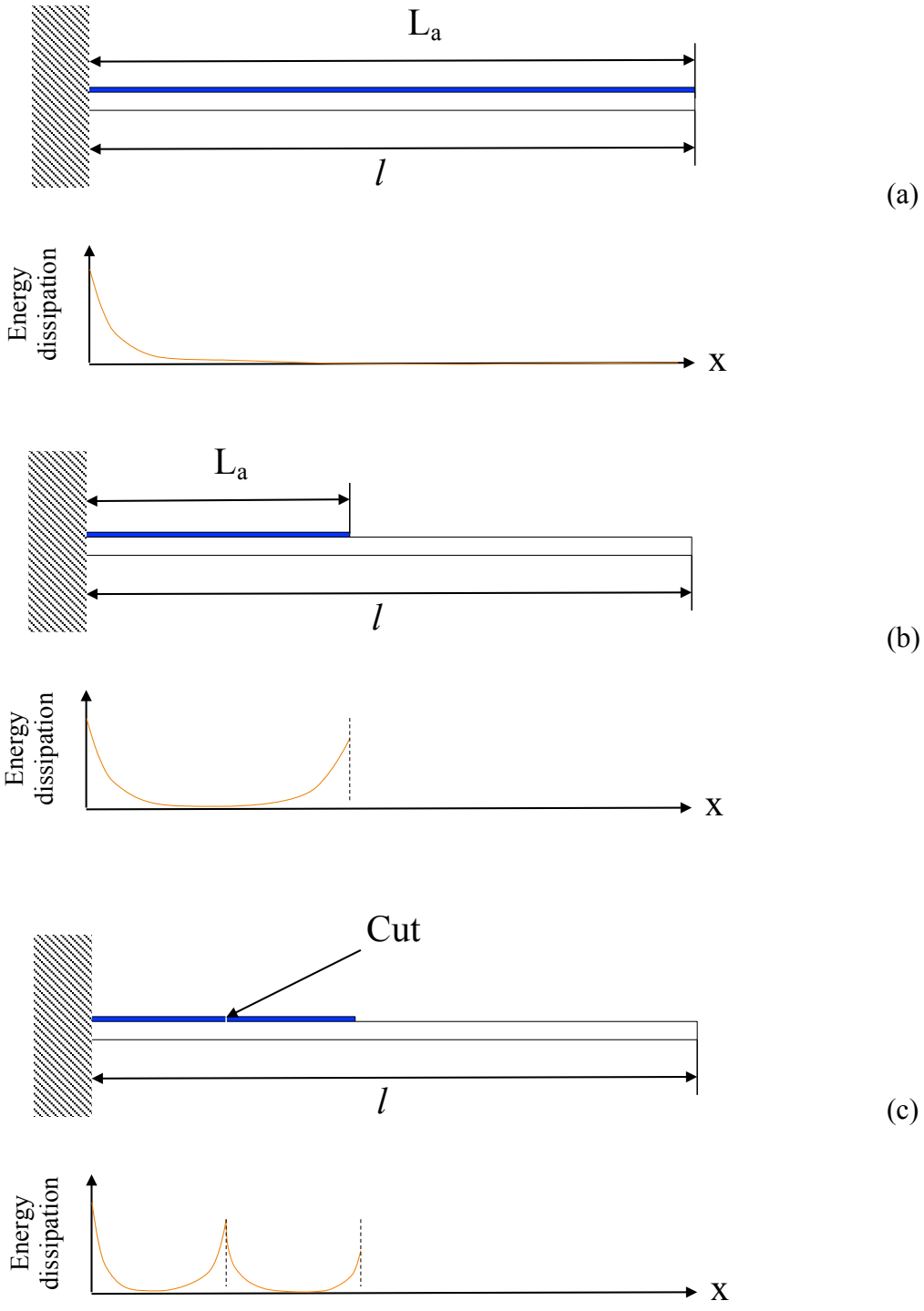

Figure 4.18: Schematic illustration of cantilever beam showing only the upper damping layer: a) fully covered. b) continuous partially covered. c) discretized partially covered.

The theoretical analysis was performed over a cantilever beam with the same geometrical and material properties as beam 3. Figure 4.19 illustrates the shear stress distribution of a cantilever beam with a continuous damping layer of 450 mm long. We observe that most of the shear stress is distributed near the clamped end, located at x = 0, within the first 100 mm of the beam.

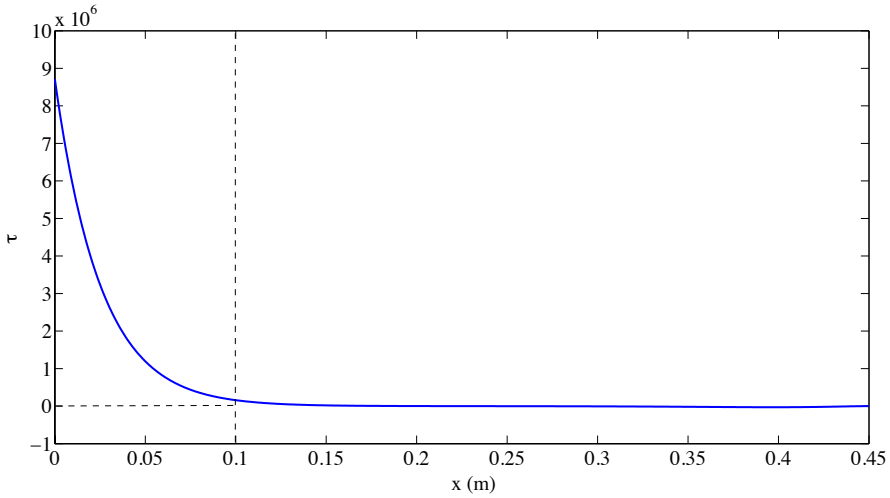

Figure 4.19: Shear stress distribution of a cantilever beam at its fundamental vibration mode.

Experimentally we determined the logarithmic decrement of the beam 3 without damping tapes, so we can predict the loss coefficient or the logarithmic decrement of additional configurations such as, L_a= 450 mm, L_a =100 mm, L_a =150 mm, and L_a =200 mm. Also we considered the discretized configurations for each of these partially covered configurations and the fully covered configuration. Table 4.6 shows estimates of the damping ratio from the Plunkett and Lee method.

Table 4.6: Optimization of damping layer length for 3M 425 damping tape.

L_a [m]	$r = L_a/SL$	ζ	$\% \zeta$	*% Mass decreased*
*0.45	21.8	0.0040	-	-
0.1	4.9	0.0070	61.3%	
0.05	2.4	0.0072	63.3%	78%
0.025	1.2	0.0048	10.7%	

La [m]	*r = La/SL*	*ζ*	*% ζ*	*% Mass decreased*
*0.45	21.8	0.0040	-	-
0.15	7.3	0.0066	52.2%	
0.075	3.6	0.0088	95.0%	67%
0.038	1.8	0.0072	66.5%	

L_a [m]	$r = L_a/SL$	ζ	$\% \zeta$	*% Mass decreased*
*0.45	21.8	0.0040	-	-
0.2	9.7	0.0060	38.7%	
0.1	4.9	0.0088	95.0%	56%
0.05	2.4	0.0091	110.5%	

*Full length

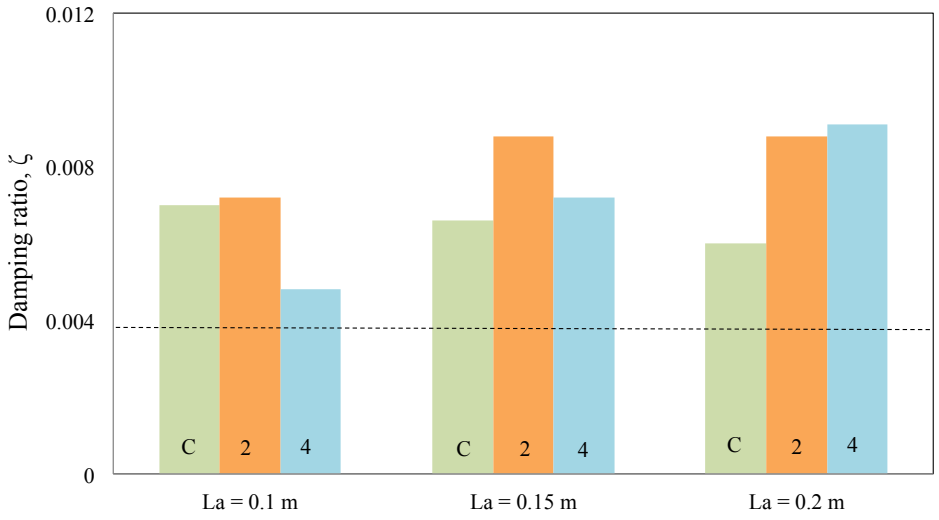

Figure 4.20: Theoretical damping ratio comparison between a partial coverage configuration with continuous length (C) L_a and two and four segments (2, 4), and a full coverage configuration of 0.45 m (dashed line).

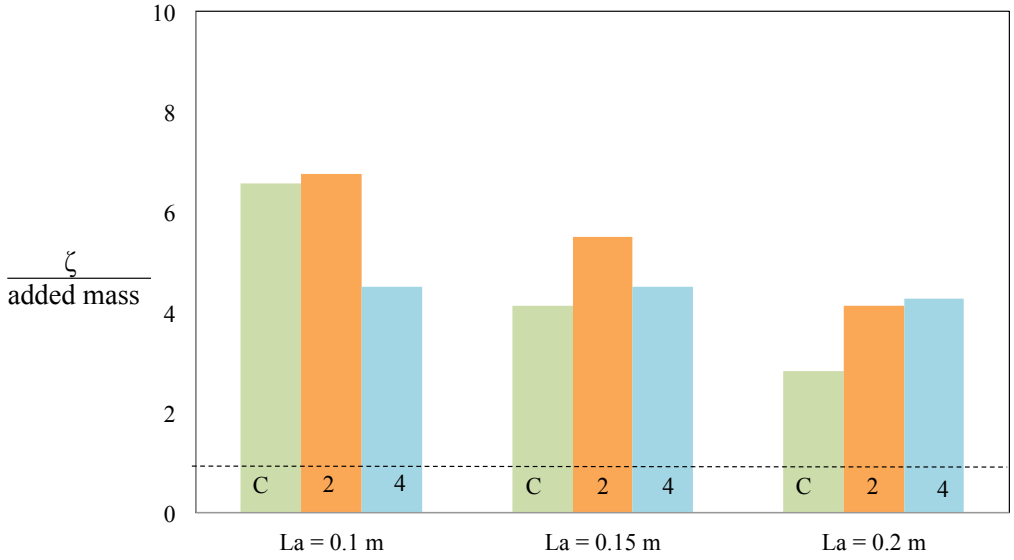

Figure 4.21: Theoretical damping ratio/added mass comparison between a partial coverage configuration with continuous length (C) L_a and two and four segments (2, 4), and a full coverage configuration of 0.45 m (dashed line).

We observe that locating damping layers of 0.1 m from the clamped end over a 0.45 m long beam, provides an improvement of the damping ratio of 61.3% and discretizing the new layer into 0.05 m segments leads to 66% increase of the damping ratio compared to the 0.45 m layer. On the other hand, if we consider an adhesive layer, $L_a = 0.15$ m and discretized it to segments of 0.075 m we obtain an increase of 95% with respect to the fully covered configuration. Similarly, if we consider a $L_a = 0.2$ m the effect of discretizing this new layer to 4 segments will lead to 110% increase. Figure 4.20 shows that the optimal configuration would be a partially covered beam with $L_a = 0.15$ m and two segments, since this configuration provided a relatively higher damping ratio compared to the full coverage configuration and relatively large mass reduction. Figure 4.21 shows the damping ratio over the added mass for each configuration compared to the full covered beam (dashed line). We observed that for $L_a = 0.1$ m, and two segments we obtain the highest damping ratio/ added mass value. This configuration may reduce the added weight to the structure and save material and cost of the surface treatment. The theoretical enhancement found in this section could be of industrial interest since we observe a decrease in the amount of damping material needed to considerably increase the damping of the beams.

4.4 Natural frequency shift due to the damping layer.

Adding the surface treatment to the beam also caused the natural frequency to change slightly. This is reasonable since we are adding mass and stiffness to the system, in addition to damping. To quantify this shift we used the LabVIEW power spectrum function. The power spectrum is a measure the power distribution in the frequency domain, (Meirovitch, 2010). The frequency shift due to the added damping layer as shown in Figure 4.22, for beam 4 with continuous and discretized 3M 425 damping tape. It is observed that the higher frequencies correspond to configurations that introduce more stiffness to the system for the same added weight. As the damping layer was discretized into smaller segments, the stiffness added by the aluminum backing decreases, so for the same mass of the damping layer, the frequency tends to decrease.

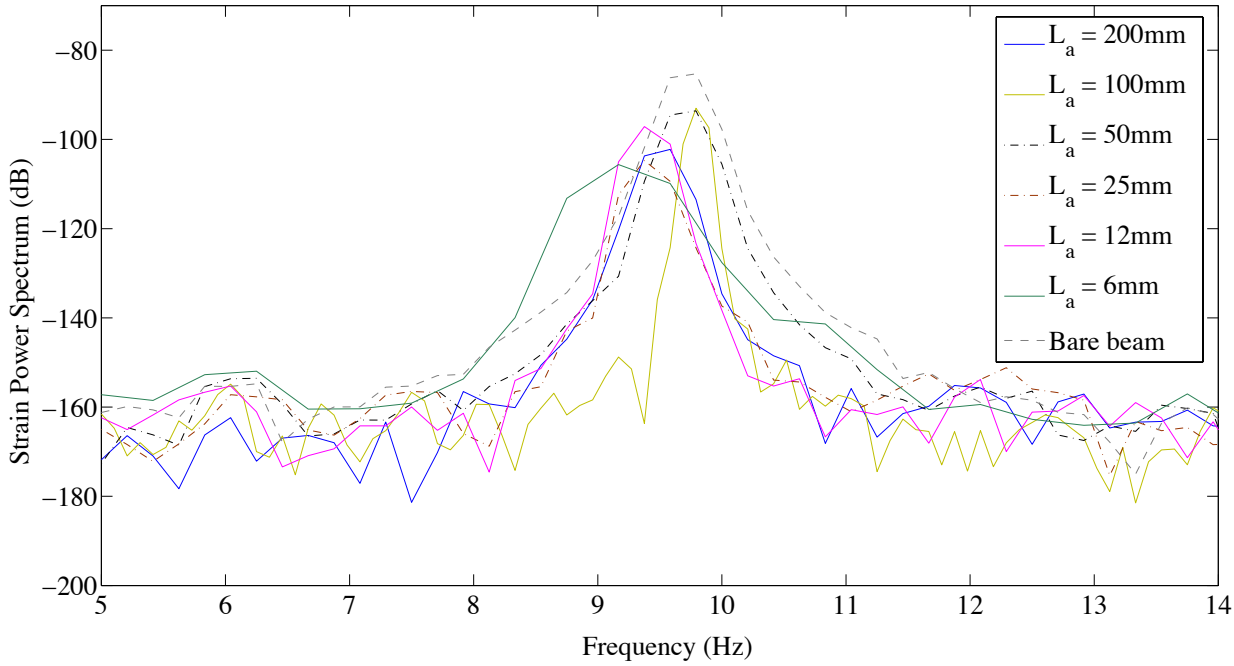

Figure 4.22: Natural frequency shift on sample 4 using tape 3M 425 for different length of constraining layer and the bare beam

This frequency shift slightly affects our previous experimental validations, since we have assumed that the first natural frequency of the system and the mode shapes were the same as the bare specimen. To have an idea of how critical the frequency could be, Figure 4.23 shows the loss coefficient predicted from the Plunkett and Lee approach, as a function of the frequency using tan δ of the master curve given in Figure 2.19. The frequency dependence of the VE material properties affects the loss coefficient of the structure with the damping layer. Note, that modifying the natural frequency of the structure could enhance or lower the damping properties of the surface treatment.

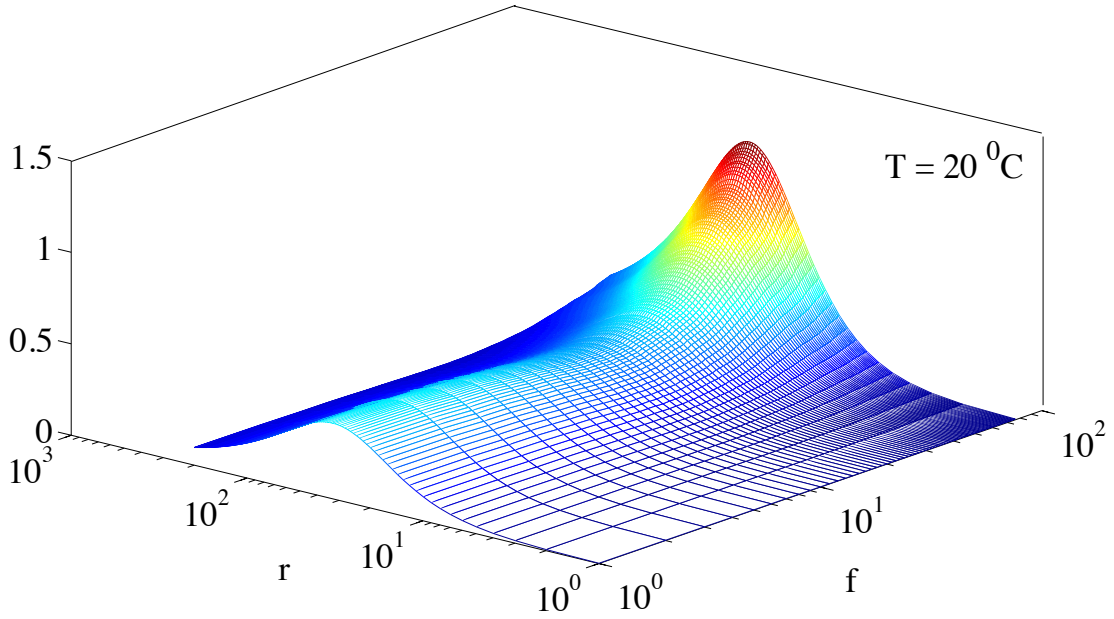

Figure 4.23: Frequency dependence of the loss coefficient maximum values at T_{ref} = 20 ^{o}C.

4.5 Summary

The optimal length of the discretization segments as related to the shear lag distance was experimentally observed. When the length of the segments is near the optimal value, the damping ratio obtained experimentally from the discretized damping treatment exhibited the highest measured value. The damping ratio percentage increase was obtained for different damping tapes and experimental beams. We considered the damping ratio increase between the continuous layer configuration and the maximum damping ratio obtained experimentally with discretized damping layers; results allowed us to observe that the thickness of the backing material of the tape affects the energy dissipation. Additionally, experimental loss coefficients for different discretization lengths and damping tapes were obtained from equation (4.14); theoretical loss coefficients were obtained from the Plunkett and Lee approach. With these experimental and theoretical values a comparison was performed and discussed. We found that as the discretization length decreased, the experimental values differed from the theoretical values. A theoretical analysis was performed to investigate configurations to optimize the damping layer length as an alternative to the added weight of more damping tape. To this end, we considered different damping layer lengths located near the clamped end of cantilever beams

where the strain was higher. The theoretical results showed that applying a surface treatment of partial length might increase the beams' damping and decrease the additional weight (and cost) compared to the full continuous damping layer configuration. Finally, the natural frequency shifts caused by the damping tapes were recorded and shown in Figure 4.22; Figure 4.23 showed that the loss coefficient obtained with a given damping treatment might change depending on the oscillatory motion frequency.

Chapter 5 Nonlinear Analysis of Cantilever Beam with Damping Treatment

5.1 Methodology for studying beams undergoing parametric excitation

In previous chapters we investigated the linear damping of a cantilever beam with discretized damping layers on each side. We also confirmed optimal values as predicted by Plunkett and Lee method, (Plunkett & Lee, 1970) for the length of damping layer segments that maximized the energy dissipation. Furthermore, using Plunkett and Lee formulation, we confirmed that optimal values are functions of the mechanical properties of the viscoelastic layer, which are functions of temperature and frequency, and the stiffness of the constraining layer.

To expand the analysis of structures with damping layers, we focus in this chapter is focused on studying the problem of cantilever beams with damping tapes subjected to parametric excitation which will caused large deflections of the structure so the performance of the damping tapes under these conditions could be analyzed. When structural elements are subjected to large deflections, the linear models used to study the response due to different types of loadings may not be accurate. In general, as the amplitude of the oscillation increases, nonlinear effects become important. To accurately understand the dynamic response of a mechanical system under more general loading conditions, it is essential to consider nonlinearities present in the system in the analytical model (Malatkar, 2003).

This chapter is divided into two components, the first stage is to carry out experiments with different adhesive segment length to shear lag distance ratios, r, as defined in Chapters 3 and 4. The second part corresponds to observations of an effective decrease of the deflection amplitudes with the damping tapes and the identification of nonlinear parameters such as the nonlinear

damping, cubic nonlinearities and parametric forcing parameters. These values are analytically validated for each configuration using the methodology given by Fung (Fung, 1998).

5.1.1 Types of structural nonlinearities

For structures where the nonlinear effects need to be considered, Nayfeh and Mook (Nayfeh & Mook, 2008) defined several sources of structural nonlinearities. This section briefly described nonlinearities expected in structural elements:

1. *Geometric nonlinearities* are attributed to large deflections of structures or nonlinear stretching of the structure. In general, structures undergoing large deformations show nonlinear strain displacement and curvature-displacement relations. Geometric nonlinearities result from changes in the potential energy of the system. Some types of geometric nonlinearities are:

    a. *Cubic geometric nonlinearities*: equations of motion with cubic nonlinearities are associated with many physical systems such as the vibration of strings, beams, plates, etc.

    b. *Quadratic geometric nonlinearities*: may arise from initial static deflection of the structure. It is known that an initial deflection of nonlinear beams affects the natural frequencies. So, governing equations originally containing only cubic nonlinearities need to include quadratic nonlinearities when initial displacement of the structure is present. This would happen to slender structures that are very common in engineering design; in such cases considering quadratic nonlinearities become important. Sato, Saito and Otomi addressed the influence of gravitational forces on the parametric resonance of a vertical cantilever beam with a lumped mass. They proved analytically that the shift in the natural frequency of the structure was related to static deflection (Sato, Saito, & Otomi, 1978).

2. *Inertial nonlinearities,* result from concentrated or distributed masses along the structure. Kinetic energy changes are the cause of these nonlinearities in the system.

3. *Material nonlinearities* are attributed to nonlinear stress-strain relationship of certain materials.

4. *Damping,* velocity dependent forces are also called damping forces or just damping. Nayfeh and Mook defined nonlinear damping mechanisms of structural systems such as hysteretic damping, air damping, etc (Nayfeh & Mook, 2008).

   a. *Air damping,* when an immersed body moves though a fluid at high Reynolds numbers, the flow separates and the drag force is nearly proportional to the square of the velocity. For moderate Reynolds number (commonly used nondimesional number use in fluid mechanics related to the velocity of a body), the damping force lies between linear and quadratic forms. Baker, Woolam and Young considered air drag forces with the form (Baker, Woolam, & Young, 1967):

$$F_D = \frac{1}{2}\rho_{air} C_D A V|V|$$

   where ρ_{air} is the density of the air, C_D is a drag coefficient taken to be 1.28 for a rectangular cross section, A is the area normal to the flow, and V is the instantaneous velocity at a point along the length of the beam.

   b. *Structural damping,* arises when materials are cyclically stressed, causing internal energy dissipation within the material itself due to internal mechanisms. In metals, dislocation slip may contribute to this internal dissipation. Researchers have found that for metals such as aluminum or steel, this internal energy dissipation is not function of frequency or strain rate. But, it is proportional to the square of the vibration amplitude. In the aim of obtaining approximate solutions of structural damping, it can be equated to an equivalent linear model using viscoelastic energy dissipation principles, (Thomson, 1996).

$$\frac{W}{cycle} = \beta\varepsilon^2$$

$$\frac{W}{cycle} = \pi\varepsilon^2 E''(\omega_o)$$

$$E''(\omega_o) = \omega_o c_{eq}$$

$$c_{eq} = \frac{\beta}{\pi\omega_o}$$

where ω_o is the natural frequency and β is a characteristic damping parameter for every specific material with units of force/displacement. A full list of this parameters was compiled by (Lee, 1966).

5.1.2 Nonlinear analytical models

As mentioned before, a linear model is sufficient when dealing with small deflections. But, as the amplitudes of the deflections increase, for accurate modeling, the analysis should include nonlinearities. Next, we consider a cantilever beam of length *l* subjected to a base excitation z (t) as shown in Figure 5.1.

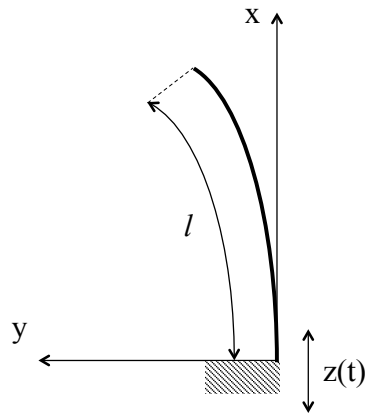

Figure 5.1: Schematic illustration of a cantilever beam subjected to base excitation, z (t).

We will consider the solution for the nonlinear system when the excitation frequency, $\Omega \approx 2\omega_1$. Zavodney and Nayfeh developed the equation of motion of a cantilever beam with a lumped mass using Euler-Bernoulli theory (Zavodney & Nayfeh, 1989). Bordanaro also developed the

equations of motion of a cantilever beam under parametric base excitation, but using energy methods. Bordanaro derived the potential and kinetic energy of the system considering the effects of the lumped mass and large deflections due to the parametric excitation with excitation frequency of $\Omega \approx 2\omega_1$ (Bordonaro, 2009). In this work we will consider the solution for the model subjected to parametric excitation frequency,

$$\Omega = 2\omega_1 + \Psi^2 \sigma \tag{5.1}$$

where σ is a frequency-detuning parameter, which is scaled with the parameter, Ψ^2 to indicate the very small difference between the excitation frequency and twice the first natural frequency. Further, Nayfeh and Mook addressed cases where the excitation frequency Ω is near other harmonics of the system, for example, $\Omega \approx 2\omega_2$, $\Omega \approx \omega_1 + \omega_2$ (Nayfeh & Mook, 2008).

In general, for our experimental model, we will consider a variation of the Duffing and Mathieu oscillators that includes damping forces, geometric nonlinearities and parametric excitations parameters to model the strain amplitude of a cantilever beam subjected to base parametric excitation (Fung, 1998):

$$\frac{d^2u}{dt^2} + \omega_1^2 u + 2\mu_1 \frac{du}{dt} + \mu_2 \frac{du}{dt}\left|\frac{du}{dt}\right| + \alpha_3 u^3 + \delta\left(\frac{du}{dt}\right)^2 = \eta_2 uf\cos(\Omega t + \tau_e) \tag{5.2}$$

where $\omega_1^2 u$ is the linear restoring force, ω_1 is the first linear undamped natural frequency of the system and, the cubic geometric and inertial restoring forces are $\alpha_3 u^3$ and $\delta (du/dt)^2 u$, respectively. The linear and nonlinear damping forces are, $\mu_1 du/dt$ and $\mu_2 du/dt\,|du/dt|$. The parameter η_2 considers the harmonic parametric excitation. The parameters, f, Ω, and τ_e are the forcing amplitude, frequency and phase, respectively (Fung, 1998). Equation (5.2) is equivalent to the equations of motion found by Zavodney and Nayfeh, and Bordanaro (Zavodney & Nayfeh, 1989) (Bordonaro, 2009). Nayfeh and Mook, (Nayfeh & Mook, 2008) presented a full

synthesis of other nonlinear models addressing other types of nonlinearities not considered in (5.2).

5.1.3 Approximate solutions to nonlinear models

Proper modeling of the response of nonlinear systems is important for the reliable prediction and control of that response. Common techniques for nonlinear systems modeling aim to identify relevant physical phenomena governing such response. There are two types of identification methods: nonparametric and parametric identification. Nonparametric identification is used to quantify the dynamics of a system without making any assumptions about the dynamics. Nonparametric identification seeks to determine the functional representation of the system to be identified. Some common nonparametric procedures are the Volterra series, the Wiener Kernel approach and the expansion of the restoring forces in a series of orthogonal sets of functions such as with Chebyshev polynomials (Nayfeh, 1985). On the other hand, parametric identification assumes a model for the dynamics and the goal is to identify the parameters in that model. This technique includes direct approaches, statistical quasilinearization, filtering, and estimation methods (Fung, 1998).

In 1985, Nayfeh proposed an approach to exploit nonlinearities in structural elements. By observing the response of a parametrically excited system with $\Omega \approx 2\omega_n$, a model was proposed and an approximate solution was given through the method of multiple scales. The solution proposed by Nayfeh used the values of the excitation and response amplitude to obtain nonlinear parameters of the proposed model (Nayfeh, 1985). Approximate solutions were found for the case when $\Omega \approx 2\omega_1$. In 1998, Fung extended the methodology proposed by Nayfeh in 1985, and used experimental measurements of the response and excitation values along with the phase quantity, γ to identify nonlinear parameters. In this thesis it is not our attempt to include a careful description of the nonlinear identification methodology. On the other hand we are focused on the results of such identification, but we will briefly summarize the method in the next section.

5.1.4 Methodology of nonlinear identification

Compared to the method proposed by Nayfeh (Nayfeh, 1985), the method given by Fung, (Fung, 1998), included measurement of phase relations. In comparison with amplitude measurements, measuring phase is more complicated. Time and frequency domain analysis are often employed to quantify the phase characteristics of a system. In 1993, Hajj et al. used a higher order spectral moments, namely the bispectrum, to obtain a phase relations between different frequency components (Hajj, Miksad, & Powers, 1993).

In this work we calculate the nonlinear phase quantity, γ, from the following phase relationship given by Fung:

$$\gamma = \Psi^2 \sigma t + \tau_e - 2\psi$$

where τ_e, is the excitation phase, ϕ is the phase of the response. As defined in equation (5.1), Ψ is a parameter that indicates the relative contributions of the nonlinear effects to the response of the structure, and σ is a frequency detuning parameter. The term $\Psi^2 \sigma t$ carries a small time variation caused by how far the excitation frequency Ω is away from twice the first natural frequency, $2\omega_1$. Considering this term as a very small quantity, we can assume that γ is constant and is given by:

$$\gamma = \tau_e - 2\psi = \text{constant}$$

and,

$$\gamma = \tau_e \quad \text{when} \quad \psi = 0$$

We calculated values of γ from experimental steady state measurements through linear interpolation. Considering the superposition of the harmonic excitation and response, we located the point at which the amplitude of the response, *a*, is zero as shown by a red dashed line in Figure 5.2. The point p_1 and p_2 are taken to be known angles from the excitation harmonic waves. In this example, $p_1 = 0$ and $p_2 = 90°$ and are used to complete the linear interpolation and determine the angle γ.

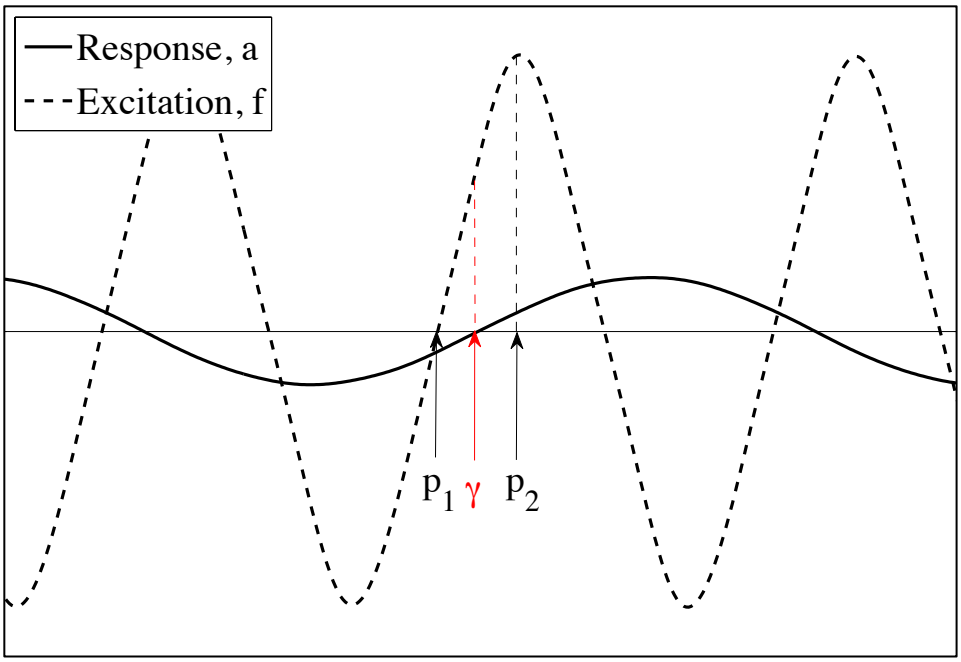

Figure 5.2: Typical experimental results from parametric excitation test with $\Omega \approx 2\omega_1$, of cantilever beams and interpolation parameters to calculate the phase angle γ, to perform nonlinear parameter identification.

From Figure 5.2 we can also obtain the amplitudes of the excitation and response time series for every steady state oscillation recorded during the experiments. By observing the steady state response and the methodology proposed by Fung (Fung, 1998), the multiple scales method leads to the following linear relationship between a and $f \sin \gamma$. Also, linear relationship were obtained between a^2 and $f \cos \gamma$:

$$a = \frac{\eta_e}{\frac{4}{3\pi}\mu_2\omega_n^2} f \sin\gamma - \frac{\mu_1}{\frac{4}{3\pi}\mu_2\omega_n^2} \qquad (5.3)$$

$$a^2 = -\frac{\eta_e}{\alpha_e} f \cos\gamma - \frac{1}{2}\frac{\omega_n \sigma}{\alpha_e}$$

These results are the key point from the method derived by Fung. As shown in Figure 5.3, plots of a vs. $f \sin \gamma$ and a^2 vs. $f \cos \gamma$ result in linear relationships. Finally, through the least squares method, we obtain the values of the slope and intercept of the lines to calculate nonlinear parameters from equation (5.2).

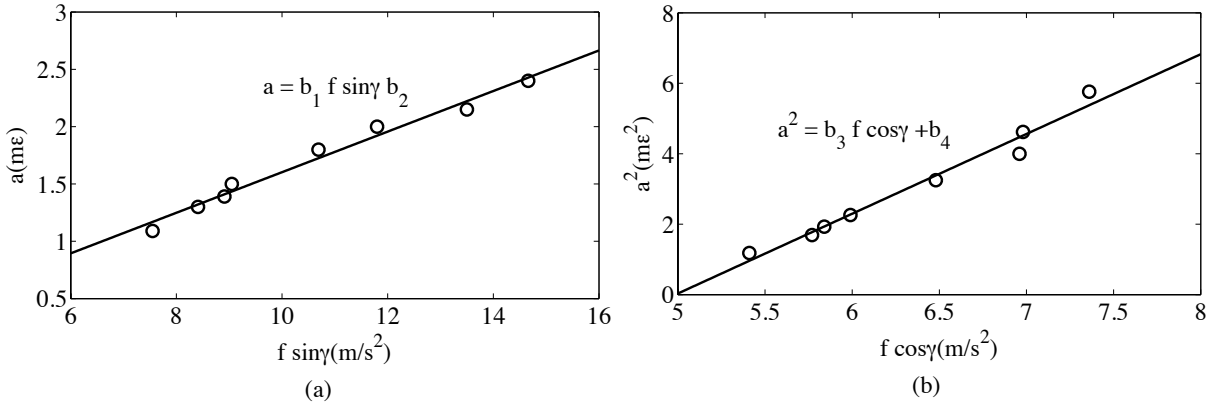

Figure 5.3: Typical plots of linear relationship between a) a vs. $f \sin \gamma$ and b) a^2 vs. $f \cos \gamma$.

Notice that equations (5.3) contain linear parameters such the linear damping, μ_1, and ω_1, the undamped natural frequency. This methodology assumes that the linear damping is calculated from linear identifications techniques such as free response tests equivalent to the tests performed for Chapter 4. The free response of the system is dominated by linear parameters of the system; considering weak nonlinearities, the importance of linear restoring and damping forces allows for independent identification of the linear parameters.

Summary of the steps for the nonlinear identification:

1. Identify linear damping, μ_1, through conventional linear system identification technique.
2. Measure the excitation amplitude, f, and frequency.
3. Measure the response amplitude, a, over a range of observed steady state oscillations.
4. Obtain the nonlinear phase difference between the response and the excitation, γ.
5. Plot the experimentally measured a vs. $f \sin \gamma$. Carry out linear fitting to obtain the parameters of such linear equation.
6. Plot the experimentally measured a^2 vs. $f \cos \gamma$. Carry out linear fitting to obtain the parameters of such linear equation.

7. Perform nonlinear system identification and obtain the parameters of the assumed nonlinear model.

5.1.5 Experimental setup and procedure for nonlinear test of the parametrically excited cantilever beam

The experimental sample considered for the nonlinear characterization consists of a 1095 HI steel beam attached to a steel-mounting clamp. The Young's modulus of the beam is 200 *GPa* and the density is 7500 kg/m^3. The width and thickness of the beam are 12.7 and 0.85 mm, respectively. The length of the beam is 270 mm between the tip of the beam and the top of the mounting clamp. Figure 5.4, shows the experimental set up. The base of the mounting plate is attached to a modal shaker that will induce the parametric excitations to the beam.

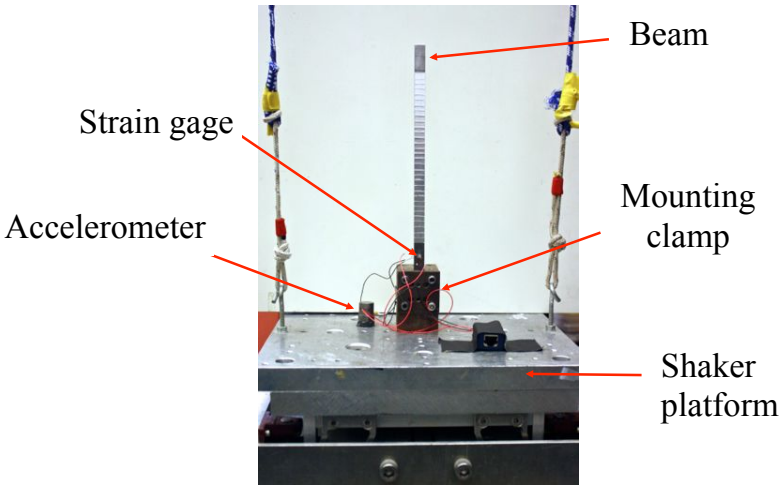

Figure 5.4: Cantilever beam in the mounting plate over the shaker platform prior parametric excitation.

The amplitude of the excitation is measured using an accelerometer attached to the top of the shaker platform, and the response is recorded using strain gages. The parameters of the accelerometer and strain gages are listed in Table 5.1. 3M 425 damping tapes was considered for these experiments, properties of this tapes are given in Table 4.1.

Table 5.1: Properties of the strain gage and accelerometer for nonlinear tests.

	Strain gage	*Accelerometer*
Designation	MM WK-06-125AB-350	PCB piezoelectronics 353B33
Gage factor	2.02 ± 1%	--
Resistance (Ω)	350 ± 0.3%	--
Sensitivity (*mV/g*)	--	103.4

The bare steel beam was firmly clamped to the mounting clamp as shown in Figure 5.5. We proceeded with the identification of linear parameters as described on section 5.1.4. Once the natural frequency and the damping ratio of the bare steel beam were obtained, the undamped natural frequency and linear damping were calculated using:

$$\omega_{d1} = \omega_1 \sqrt{1-\zeta^2} \qquad (5.4)$$
$$\mu_1 = \zeta \omega_1$$

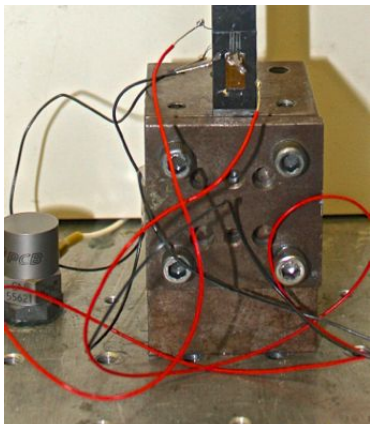

Figure 5.5: Experimental sample attached to the mounting clamp.

Once the undamped first natural frequency and the linear damping were obtained from the free vibration test and equations (5.4), we induced parametric excitation to the cantilever beam near twice its natural frequency in accordance with equations (5.1) and (5.2). Then we recorded the steady state oscillation of the bare beam for different excitations amplitudes. Once we saved the

data for the bare beam, we removed the cantilever beam from the mounting plate and bonded 200 mm long layers of the damping tape 3M 425 on both sides of the beam as shown in Figure 5.6. The excitation frequency was set to 19.4 Hz and the amplitude of the shaker was varied between 5 to 15 m/s^2. Higher amplitudes were not possible for safety reasons, as the deflections of the beam became extremely large.

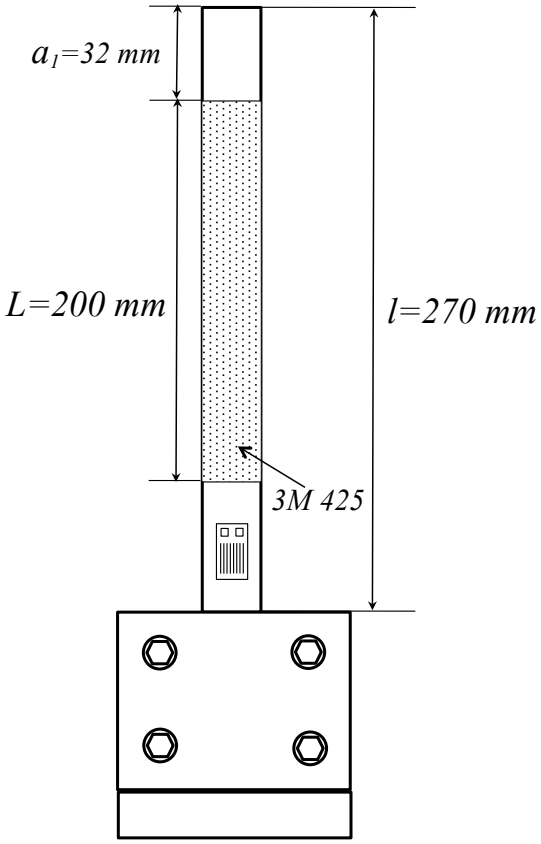

Figure 5.6: Schematic of the steel cantilever beam with the continuous 200 mm layers of 3M 425 damping tape.

We repeated the procedure as with the bare beam and obtained the linear damping and the first undamped natural frequency of the steel beam with the damping tape on each side. As mentioned in Chapter 3, when we added the damping tapes to the structure, the damped first natural frequency changed slightly due to the effects of the added mass and stiffness. Therefore, the parametric excitation frequency will also change for the tests with the damping tape. It is important to take this into account because of the considerations made from equations (5.1) and

(5.2). For the beams with the surface treatment, the excitation frequency was set to 19.3 ± 3 Hz, and the excitation amplitude was set from 7 to 20 m/s^2. Once the steady state oscillations were recorded for different forcing amplitudes, the damping tape layers were discretized into equal segments, as shown in Figure 5.7.

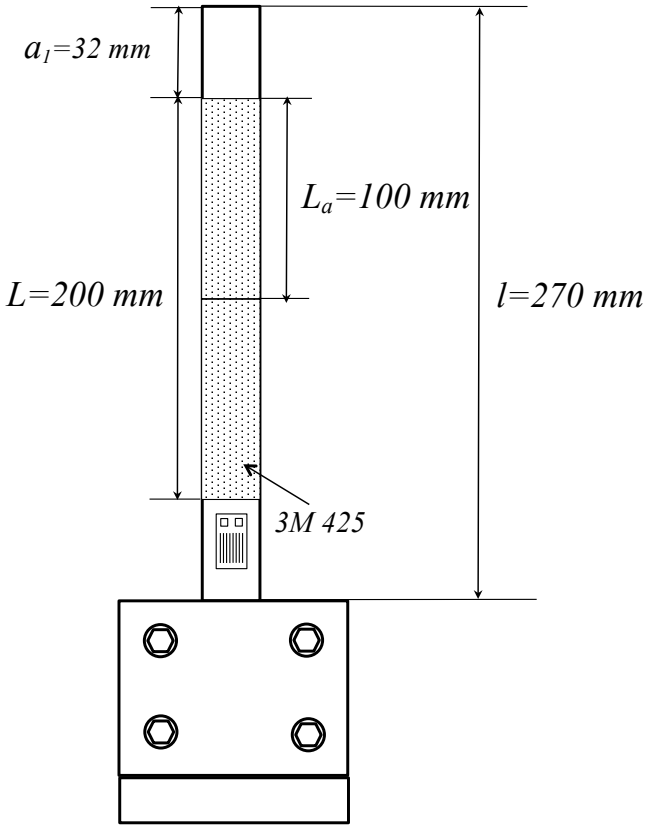

Figure 5.7: Diagram of the cantilever beam with a discretized 3M 425 damping layer L_a=100 mm.

The first segment was made at 100 mm from the beginning of the damping tapes, or the middle of the damping layers; following cuts were made to obtain discretized length L_a, of 50 mm, 25 mm, 12 mm, and finally 6 mm. The cuts were made after the steady state oscillating data were recorded for each case, similar to the procedure explained for the bare steel beam and the beam with continuous layers of 3M 425.

5.2 Results of parametric excitation for steel cantilever beam.

In this section, we show the experimental results from the parametric excitation test explained in the prior section. This section is organized in two main components. First, we show the response amplitude versus excitation amplitude for the different L_a. Then, we show the results of the nonlinear identification performed for each case. We also explain the statistical method used to trace the propagation of the error coming from the least squares method and equations (5.3).

5.2.1 Response amplitude and excitation amplitude behavior

Experimental data obtained for different damping tape length ratios, *r,* are summarized in this section. Figure 5.8 and Figure 5.9 show the time histories recorded for each case of *r*. Figure 5.10 shows a more general overview of results, plotting the amplitude of the excitation versus the amplitude of the response during the parametric excitation of the steel cantilever beam. We included the loss factor values measured experimentally and analytically compared with the Plunkett and Lee method (Plunkett & Lee, 1970). We observe that the response amplitude decreases for the *r* values with high loss factors with the exception of the case of r = 8.3 corresponds to the value and L_a = 200 mm. For the same excitation amplitude, this configuration showed a higher amplitude than the configuration for r = 4.1 which is near the optimum value found with formulations given in Chapter 3. The other cases of *r* considered for the tests, showed smaller loss factor and therefore higher response amplitude.

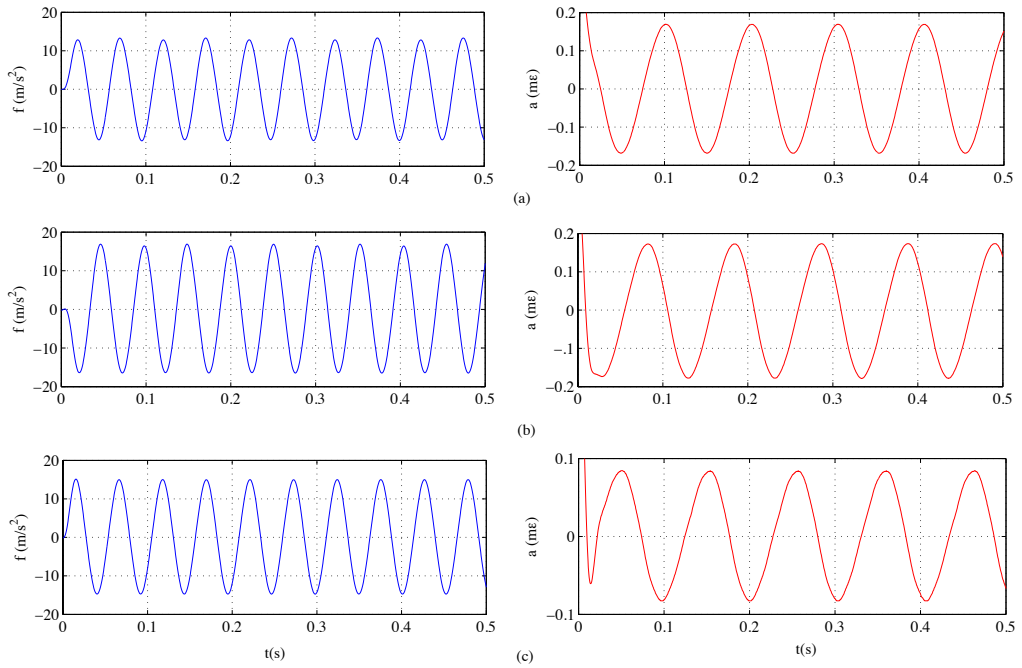

Figure 5.8: Time histories of the excitation and response for: a) $r = 8.3$, b) $r = 4.1$, and c) $r = 2.0$, respectively.

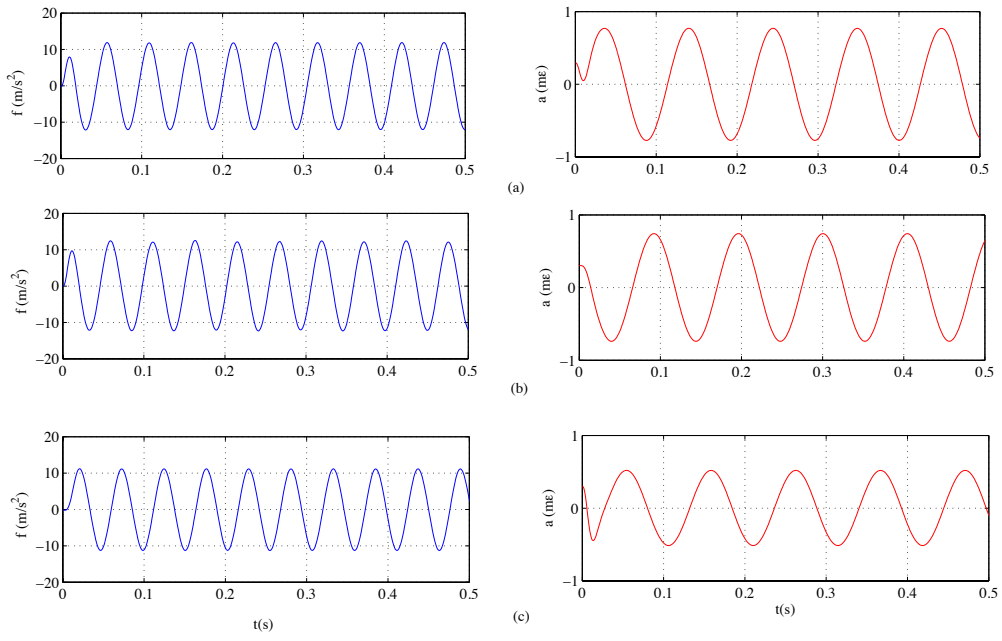

Figure 5.9: Time histories of the excitation and response for: a) $r = 1.0$, b) $r = 0.5$, and c) $r = 0.2$, respectively.

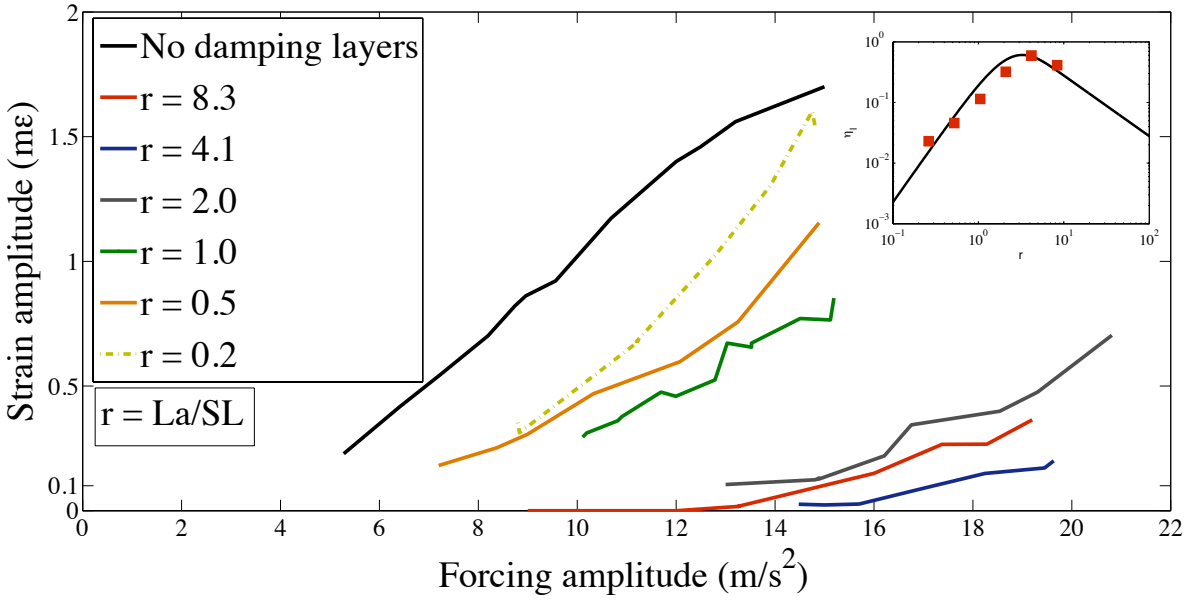

Figure 5.10: Response amplitude vs. forcing amplitude for different *r* using tape 3M 425.

Each data set in Figure 5.10 correspond to the same damping layer discretized for the different *r* values. For the same forcing amplitude, data collected for $r = 4.1$ showed the lowest response amplitude; this is the same *r* value that gives the highest linear damping. The inset in Figure 5.10 shows the experimental results of free vibration tests performed before each parametric excitation tests (red dots) and the loss coefficient predictions made from the analysis given in Chapter 3 (black line). As the linear damping assumes values that are close to the linear damping value of the bare beam, the effect of the damping layers decreased. We observe that the amplitude of the response increased to values near the response of the bare beam and higher than the response of optimal *r* value, as shown in Figure 5.11.

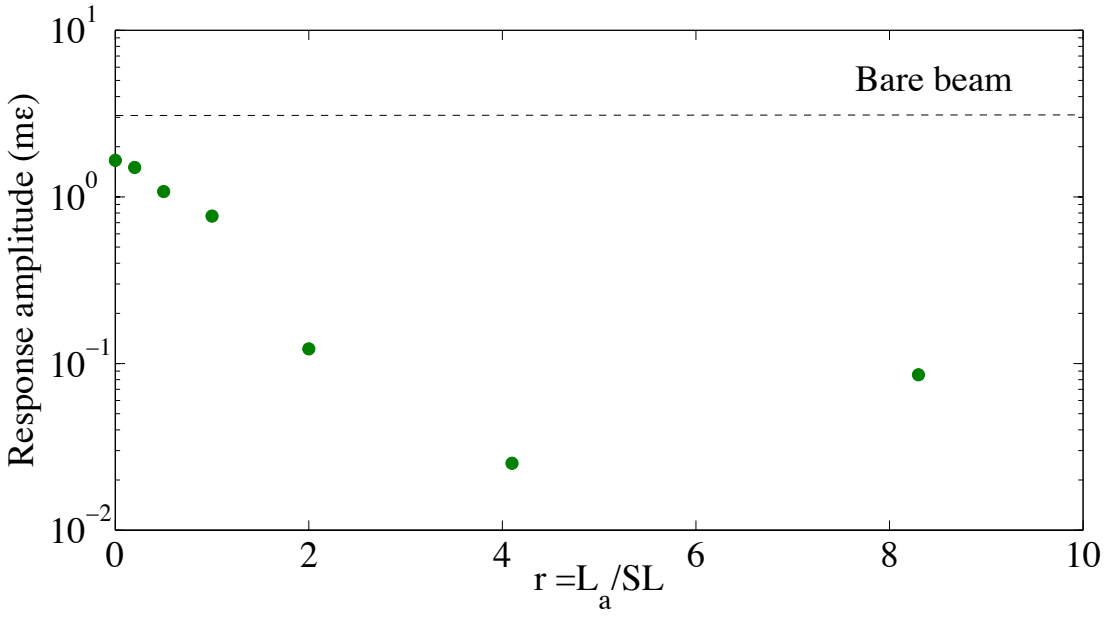

Figure 5.11: Response amplitude vs. r for forcing amplitude of 14.5 m/s^2.

5.2.2 Nonlinear parameters identification

Adding damping layers to the structure helped to diminish the amplitude of the deflection, as expected. In this section we will study the effect of the damping tape to the nonlinear parameters governing the equation (5.2).

Table 5.2: Summary of identified nonlinear parameters from the steel cantilever with different r of tape 3M 425

	No damping layers	*200 mm*	*100 mm*	*50 mm*	*25 mm*	*12 mm*	*6 mm*
Ω (Hz)	19.40	19.70	19.60	19.15	19.00	19.20	18.90
μ_1 *(Hz)*	0.0266	0.0626	0.0662	0.0473	0.0336	0.0288	0.0271
η_2 $(m\varepsilon^{-1})$	10.422	9.034	16.477	16.734	7.978	10.124	7.555
α_3 $(m\varepsilon^{-2}s^{-2})$	8.874	188.904	1320.662	182.286	23.031	38.922	9.485
μ_2 $(m\varepsilon^{-1})$	0.0102	0.0201	0.0294	0.0101	0.0108	0.0103	0.0043
ω_1 *(Hz)*	9.71	9.80	9.65	9.41	9.47	9.56	9.42

The parameters summarized in Table 5.2 were calculated from equations (5.3). Because this equations is based on the estimated slope and intercept of the a vs. $f \sin \gamma$ and, a^2 vs. $f \cos \gamma$ found from the least squares fits, the error propagation is difficult to obtain through conventional statistics methods due to the fact that equations (5.3) are function of each of the estimated values. In 1979, Efron introduced the "bootstrapping" method in order to manually estimate confidence intervals and prediction of error of estimate values from such complicated functions. The methodology used in this thesis to obtain the 95% confidence intervals of the identified nonlinear parameters is based on this statistic technique. The "bootstrapping" method consist of:

1. Resampling of the experimental data collected, in this case the values of a vs. $f \sin \gamma$ and a^2 vs. $f \cos \gamma$. Using the software R™, we pick random pairs from the original experimental values and create a new array.
2. Apply the least squares approach to obtain the slope and the intercept for each resample array.
3. Use the equations (5.3) to obtain the nonlinear parameters for each resample.
4. Manually obtain the 95% confidence interval for each nonlinear parameter from,

$$95\% \text{ Confidence interval} = \bar{x} \pm \frac{1.96\bar{\sigma}}{\sqrt{N}}$$

where, $\bar{x}$ and $\bar{\sigma}$ are the average and the standard deviation of the nonlinear parameters calculated for each resampled x-y array respectively, and N is the number of resamples.

This methodology was very helpful in the analysis of the identified parameter from the experimental measurements. In Figure 5.12, Figure 5.13, and Figure 5.14 we plot the mean values and their corresponding 95% confidence interval. Additionally, we show in Figure 5.13 and Figure 5.14 the loss factor for the different r values experimental and analytically obtained in order to compare the effect of the increase of the linear damping with the damping tapes to the identified nonlinear parameters.

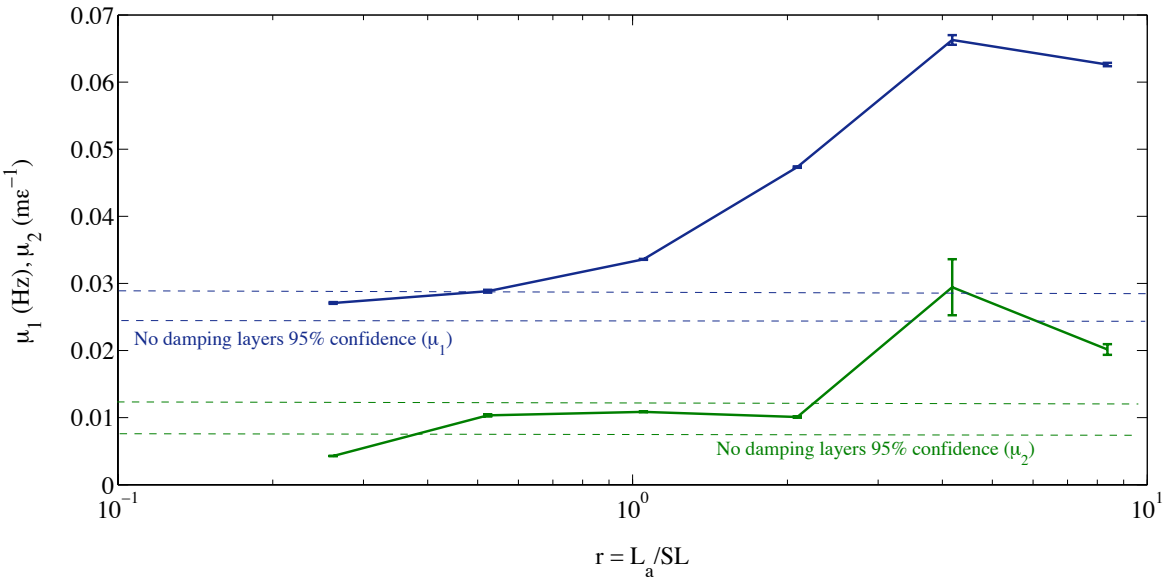

Figure 5.12: Linear and nonlinear damping vs. r, ratio of adhesive cut length to shear length for steel cantilever with adhesive 3M 425.

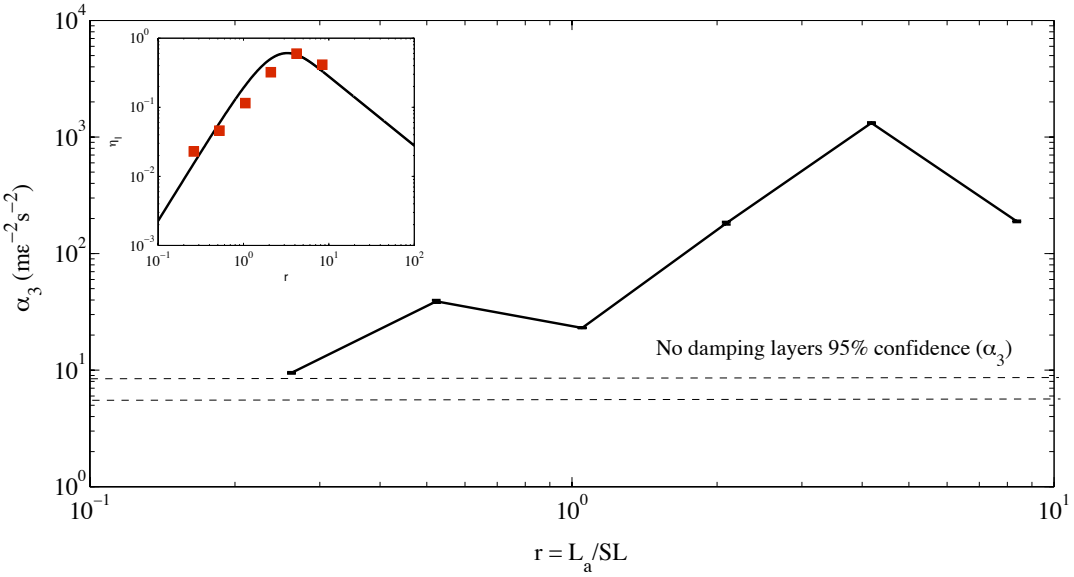

Figure 5.13: Cubic nonlinear parameter (α_3) vs. r, ratio of adhesive cut length to shear length for steel cantilever with adhesive 3M 425.

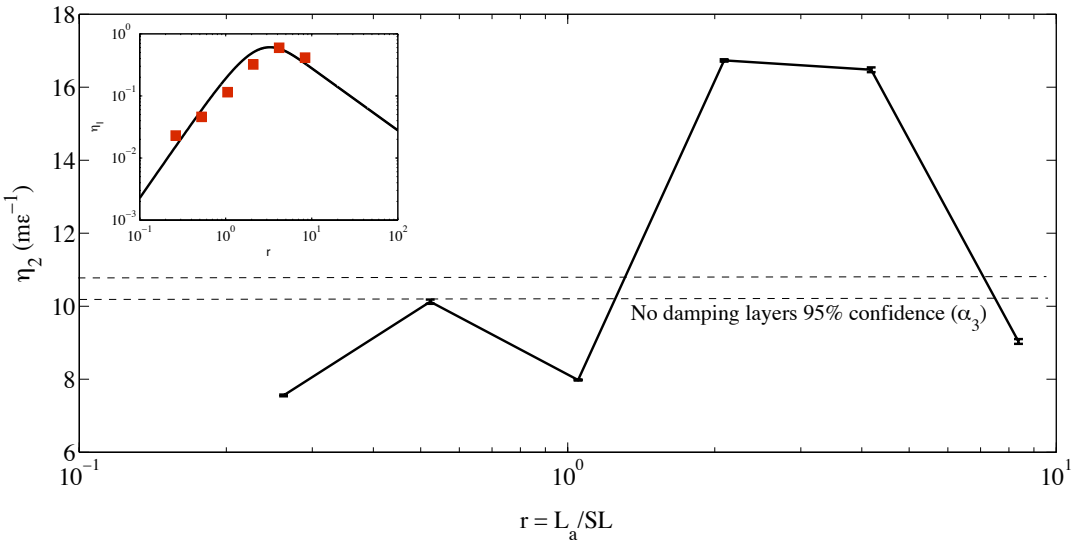

Figure 5.14 Parametric forcing parameter (η_2) vs. r, ratio of adhesive cut length to shear length for steel cantilever with adhesive 3M 425.

From Figure 5.12, we observe an increase in the nonlinear damping for configurations near the optimal value of *r* that resulted in maximum values of the linear damping. For the values away from this *r* optimal value, the identified nonlinear damping showed values within the 95% confidence interval of the nonlinear damping calculated for the bare beam, meaning that the damping layer did not significantly affect the nonlinear response of the beam for these cases. The nonlinear damping is related to air drag and structural damping. As such, we would expect that as we discretized the damping layer obtaining responses amplitudes near the values of the bare beam as shown in Figure 5.10, the velocities reached by the beam are similar as for the bare beam the nonlinear damping mainly attributed to the air drag, eventually would reach the values of the bare beam.

Figure 5.13 shows that, the cubic nonlinearities increased with the added layers compared to the bare beam. Since, cubic geometric nonlinearities arise from the potential energy of the structure, we would expect that the added mass and stiffness of the damping layer modified the potential energy of the beam so we observe a significant change with respect to the bare beam. Notice that, except for *r* = 0.2, the discretized damping layer showed an increased cubic nonlinearity. On the other hand, the parametric forcing parameter, that represents how effectively the

parametric excitation affected the dynamics of the beam, increased for r near the optimal value, and again, showed a drop when the beam had a continuous damping layer, similarly as for α_3 and μ_2, η_2.

5.2.3 Nonlinear parameter validation

To validate the identified parameters, we integrated equation (5.2) and simulate the response due to different forcing amplitudes comparable to those used in the experiments. The simulation was performed using a MATLAB routine, specifically using ODE45 function, based on the Runge Kutta method. The integration time step was set at 0.000504 s and the total integration time was set from 0 to 100 s. As a qualitative measure of the agreement between the mathematical model and the experimental data, in Figure 5.15 we show the response of the steady-state response for different forcing amplitudes.

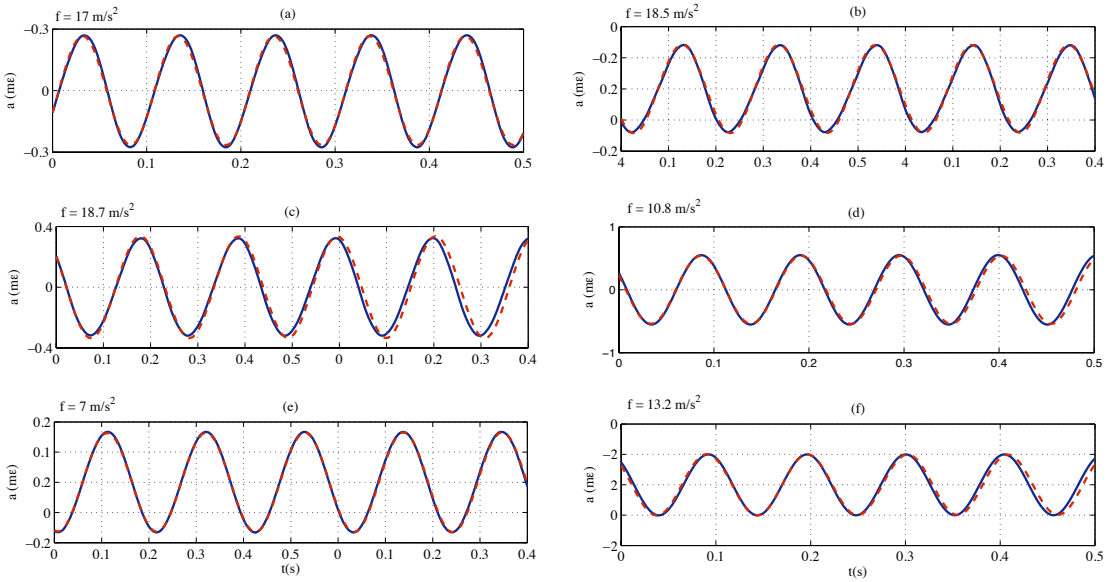

Figure 5.15: Comparison of the steady state time histories obtained experimentally (solid line) and analytically (dashed line) for the steel cantilever for (a) $r = 8.3$, (b) $r = 4.1$, (c) $r = 2.0$, (d) $r = 1.0$, (e) $r = 0.5$, (f) $r = 0.2$.

Figure 5.15, shows a relatively good agreement of the simulations using the identified parameters identified of Table 5.2 in equation (5.2) based on the procedure given by Fung (Fung, 1998).

5.3 Summary

The main results for this chapter included the confirmation of the effectiveness of the surface treatment reducing the amplitude of the harmonic response of the cantilever beam with different discretization length as showed in Figure 5.11. Additionally, nonlinear identification was performed to study the effects of the damping layers to the nonlinear parameters such as nonlinear damping, cubic nonlinearities, and forcing parameters were obtained for different discretization length. We observe a noticeable increase in the value of the cubic nonlinearities of the damped structure compared to the beam without damping layer. The nonlinear damping obtained was maximum for the damping tape configuration with highest linear damping, $r = 4.1$ except for the continuous damping layer. The nonlinear parameters were used with equation (5.2) to compare the simulated response and the experimental data, obtaining a good agreement as showed in Figure 5.15.

Chapter 6 Large Deflection Effects on Damping tape Response

6.1 Methodology to study large deflections effects on damping tapes

In this work, we focus on the effectiveness of discretized damping tapes and included a nonlinear analysis in order to investigate the effects of such damping layers on the nonlinear parameters of a structural element, but also to investigate the effects of large deformations on the damping tapes and on the dynamics of the beam undergoing such motion.

6.1.1 Buckling of thin films over an elastic substrate.

Constrained damping layers when used as a mechanism to damp vibrations can be as thought of as a thin stiff film over an elastic foundation. A problem arises when the axial forces experienced in the backing material of the tape reach a level where the instability of the film occurs, resulting in buckling as described by Parfitt and Lambeth (Parfitt & Lambeth, 1960). In such cases, the viscoelastic (PSA) layer experiences a different deformation regime. Before this regime the viscoelastic layer is subjected to shear deformation. Although there will always be peel stresses at terminus of the backing layers, but will be localized at the ends due to the rapid decay of BoEF stresses. When buckling occurs, the viscoelastic layer is also subjected to oscillatory out-of-plane strains throughout the buckled regions, which introduces another energy dissipation mechanism. As the axial load on the backing material reaches a critical value, the deformation of the stiff backing layer of the damping tapes could experience two types of deformation: wrinkling or buckle-delamination (Hetényi, 1971).

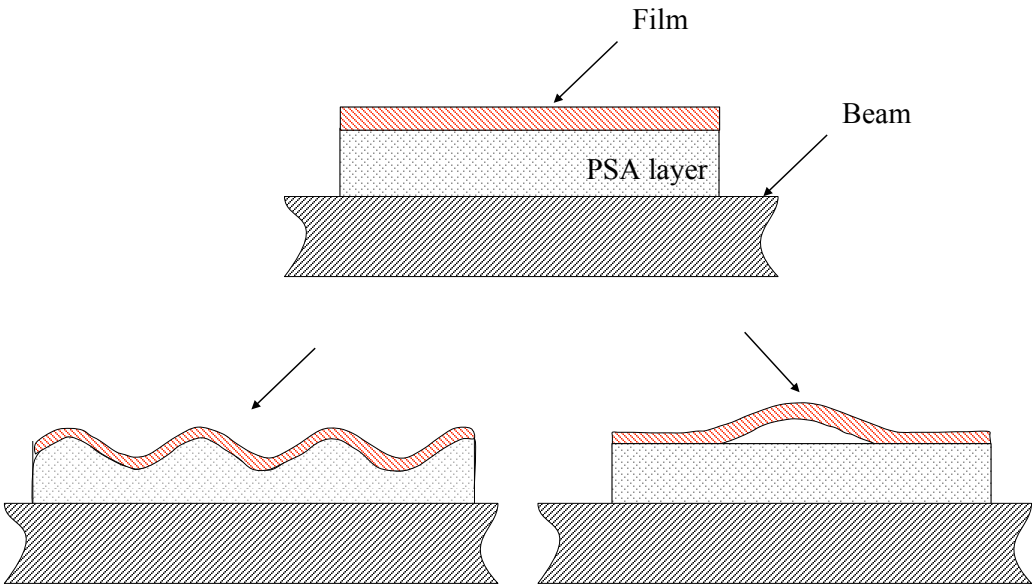

Figure 6.1: Schematic of the two considered buckling modes in thin films. a) buckling. b) delamination.

Figure 6.1 shows the two buckling modes of a thin film over an elastic substrate. These two buckling modes, are often observable macroscopically. Yet, one of the common problems is to determine which mode will govern the deformation of different systems. Huang considered the kinetic wrinkling of an elastic film on a viscoelastic substrate. He made a classification based on critical conditions at the elastic limits of the film and the glassy and rubbery states of the viscoelastic substrate. Applying linear perturbation analysis, Huang studied the kinetics of wrinkling in films subjected to large compressive stresses, and showed that depending on the stress level, the growth of buckling can have different dynamics (Huang, 2005).

Mei et al. observed that buckling delamination occurs often with relatively stiff substrates and wrinkling occurs only when the substrate is very soft. They presented a theoretical basis for predicting which deformation mode will prevail for different systems based on geometrical properties and mechanical properties of the substrate and the film (Mei, Huang, Chung, Stafford,

& Yu, 2007). Vella et al. studied the macroscopic delamination of thin films on elastic substrates. Performing controlled experiments at macroscopic scales to study the dimensions of these blisters (Figure 6.1b) in terms of material properties, they explained experimental results by using a combination of scaling and analytical methods. A method for determining the interfacial toughness was obtained and it was shown that, in order to avoid fatigue damage on the film, the thickness must be greater than a critical value, which was determined in the analysis (Vella, Bico, Boudaoud, Roman, & Reis, 2009). Audoly and Boudaoud studied different patterns that arise as a function of the biaxial residual stress in the film by considering appropriate boundary conditions used at the interface between the film and the substrate. A key point from their work included a linear analysis of the classical pattern consisting of straight stripes and identifying secondary instabilities leading to the formation of undulating stripes, or varicose, checkerboard or hexagonal patterns (Audoly & Boudaoud, 2008).

We introduce the possibility of buckling to our work since the large deflections caused by nonlinear oscillations of the cantilever beam under parametric deformation reached sufficiently large amplitudes that buckling formation was observed during the experiments.

6.1.2 Large deflection effect on the damping tapes stability.

Consider a cantilever beam, with symmetric damping tapes applied, subjected to parametric excitation as described in Chapter 5. When the amplitude of the excitation is high enough, large deflections of the cantilever beam are obtained. As the deflection amplitude increases, higher axial stresses are induced in the backing material of the damping tapes. At sufficiently high levels of strain, the backing material tends to buckle, resulting in an additional energy dissipation mechanism. Using the formulation presented in section 3.5, the value for critical load and strain amplitude measured by the strain gage was obtained. From equation (3.30) the value of the critical strain was found to be 83 με, and the buckle spacing frequency was 0.8 mm. From the time histories presented in Figure 5.8 and Figure 5.9, we observe that the recorded values of the strain amplitude are higher than the critical buckling strain. Above this level, we expect to observe buckling of the backing material of the 3M 425 damping tape. To investigate the effects of buckling of the damping tape, we performed additional free vibration tests subjected to different initial displacement conditions.

6.1.3 Free damped vibrations test with different initial displacement.

Because the critical strain value calculated is quite small, most of the experimental measurements involved at least a portion of the beam straining above this strain value, we investigated the effect of buckling formation on damping response by performing additional free vibrations test. These tests involved subjecting a cantilever beam to successively larger initial displacements, x_i, in order to induced buckling in the constraining layer of the damping treatment, as illustrated in Figure 6.2.

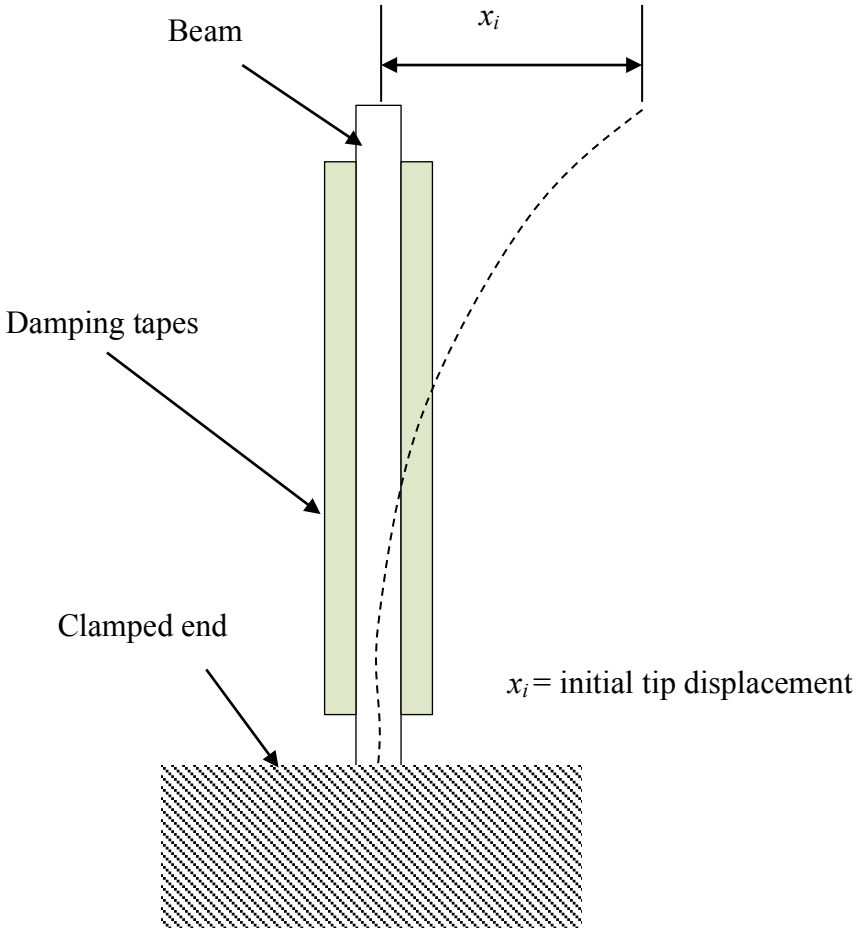

Figure 6.2: Schematic illustration of the initial displacement applied to the tip of a cantilever beam for free damped vibrations tests.

6.2 Results of large deflection effects on the performance of damping tapes

In Figure 6.3, the logarithmic decrement vs. strain amplitude is plotted. The cantilever beam is subjected to an initial displacement that results in increasing values of strain, but this plot allows for comparison of the damping as increasingly larger initial strains damp back to very small levels. Notice that as the initial displacement/strain increased, the value of the resulting logarithmic decrement also increased, suggesting permanent damage or change were occurring. The buckling effect could explain the notable increased energy dissipation remaining even when the vibration amplitudes had returned to lower amplitudes.

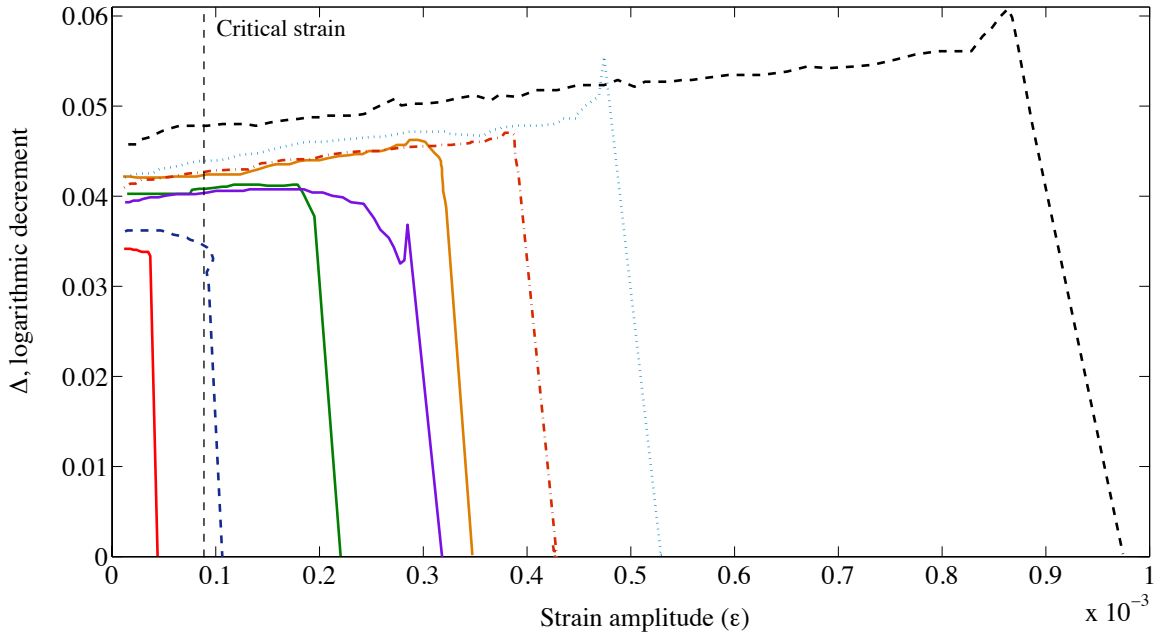

Figure 6.3: Logarithmic decrement measured from different initial displacement for L_a=200 mm and 3M 425 damping tape. The vertical dashed line denotes that the strain at the base of the cantilever has reached the critical strain at which buckling is predicted to occur.

The slight slope exhibited by a given measurements may be due to air and structural damping; but, as shown at a given strain amplitude, the logarithmic decrement remains higher when a specimen has been previously subjected to a higher strain amplitude. A possible explanation for this loading history effect is that the onset of buckling and the upward (from base to tip of

vibrating beam) expansion of the buckled regions with increasing tip displacement amplitude means larger affected areas of the constraining layers. Buckle patterns were evident in the beam at rest as shown in Figure 6.4. So permanent effects, perhaps due to very low yield stresses of the dead soft aluminum backing, may also affect the energy dissipation of the damping treatment.

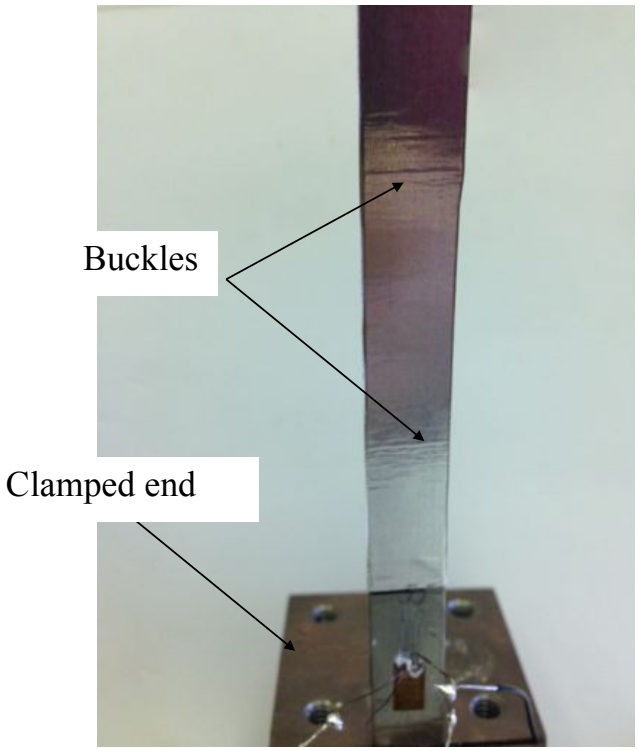

Figure 6.4: Buckling of backing material on 3M 425 damping tape.

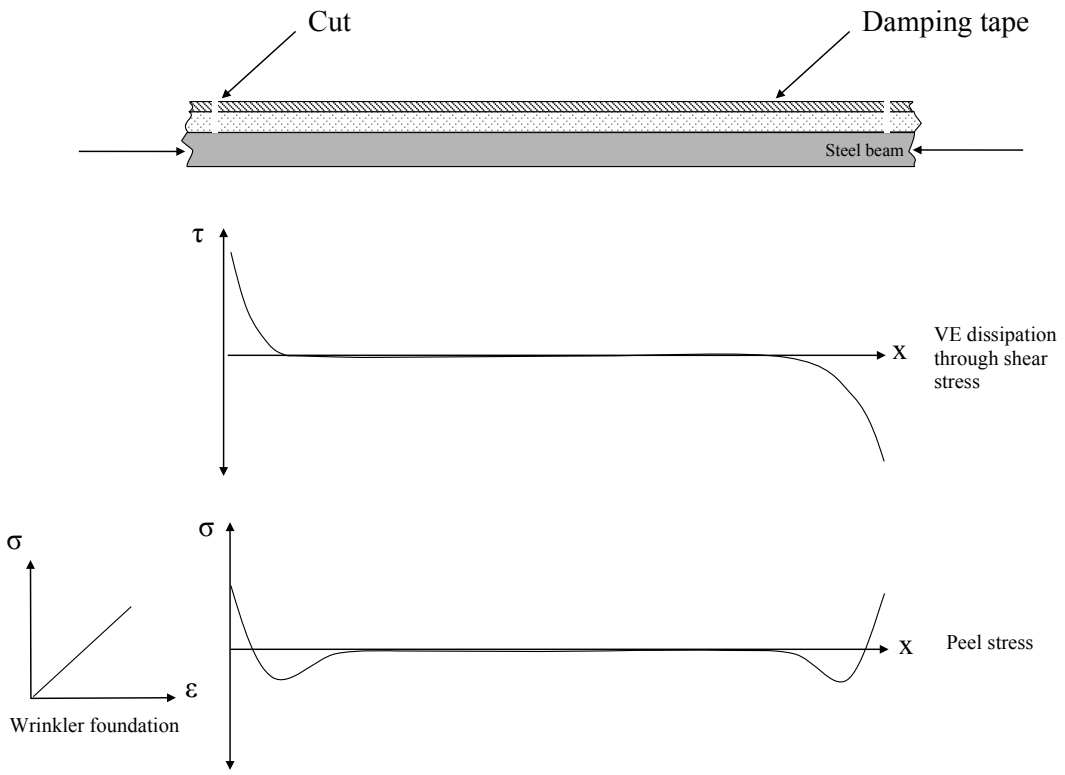

Figure 6.5: Diagram of the unbuckled damping tape over the steel beam and the shear and peel stresses distribution along the length of the damping layer.

Shear and axial stress distributions along the length of a damping layer segment when the strain level is below the critical buckling value are shown in Figure 6.5. In this case, the energy dissipation is often attributed to shear deformation of the viscoelastic layer, though localized peel stresses are also presented and the ends of the backing. Recovering from Chapter 3 the concept of a shear lag distance, as the characteristic distance associated with the transfer of axial load from one adherend to the other, implies that there is a spatial lag before the axial stress reaches equilibrium. From Figure 6.6, we notice that there appears to exist a length, x, above the lower edge of the damping tape where the beam surface strains are greatest, where buckles are not noticeable. Distance *x* (green) shown in Figure 6.6 can be related to the shear lag distance given in equation (3.5).

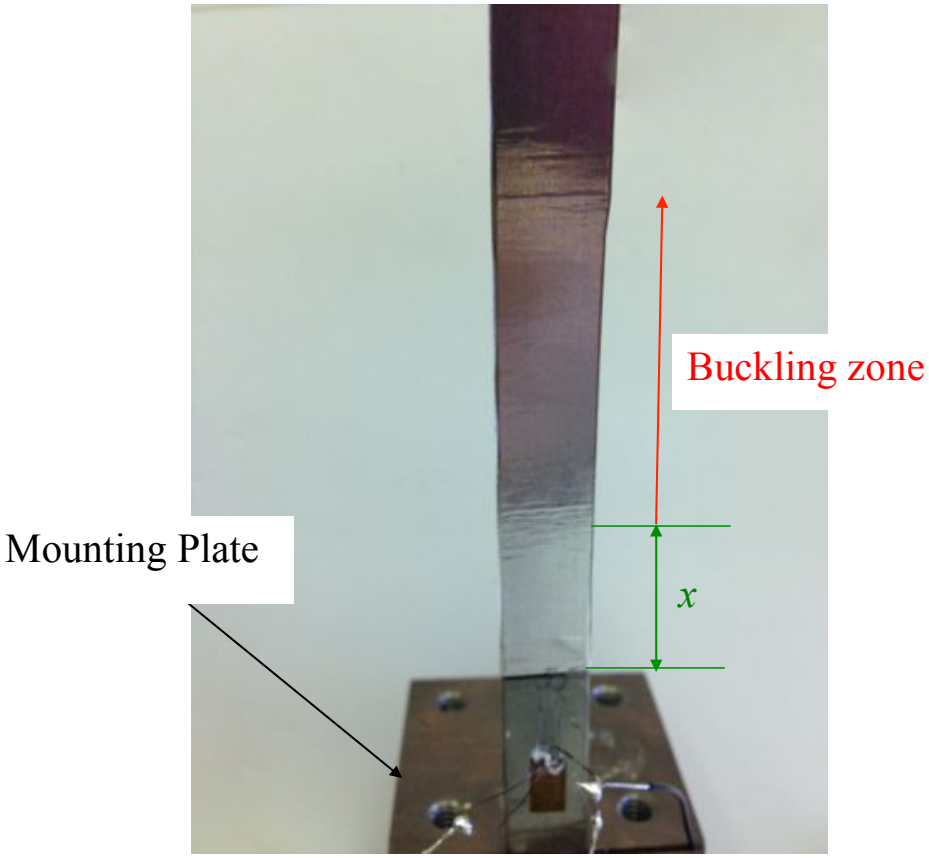

Figure 6.6: Buckling formation on experimental cantilevers related to the shear lag distance.

In 1991, Curtin extended Volkersen's shear lag model to fiber breakage in composites. This study is known as the "car-parking problem". Curtin defined a "recovery length", considering the characteristic length necessary to reintroduce stress into a cut adherend sufficient for failure to occur (Curtin, 1991). In this work we extended the analysis to discretized-damping layers. To this end, consider Figure 6.7a showing the shear lag distance (green), and the axial load (blue) in the constraining layer. For the regions where the axial load is higher than the critical buckling load (red), we can observe in Figure 6.7b the buckling zone, introducing an additional energy dissipation mechanism associated with out-of-phase stretching of the damping layer. Visual experimental results of the observed buckling zone are also shown in Figure 6.6.

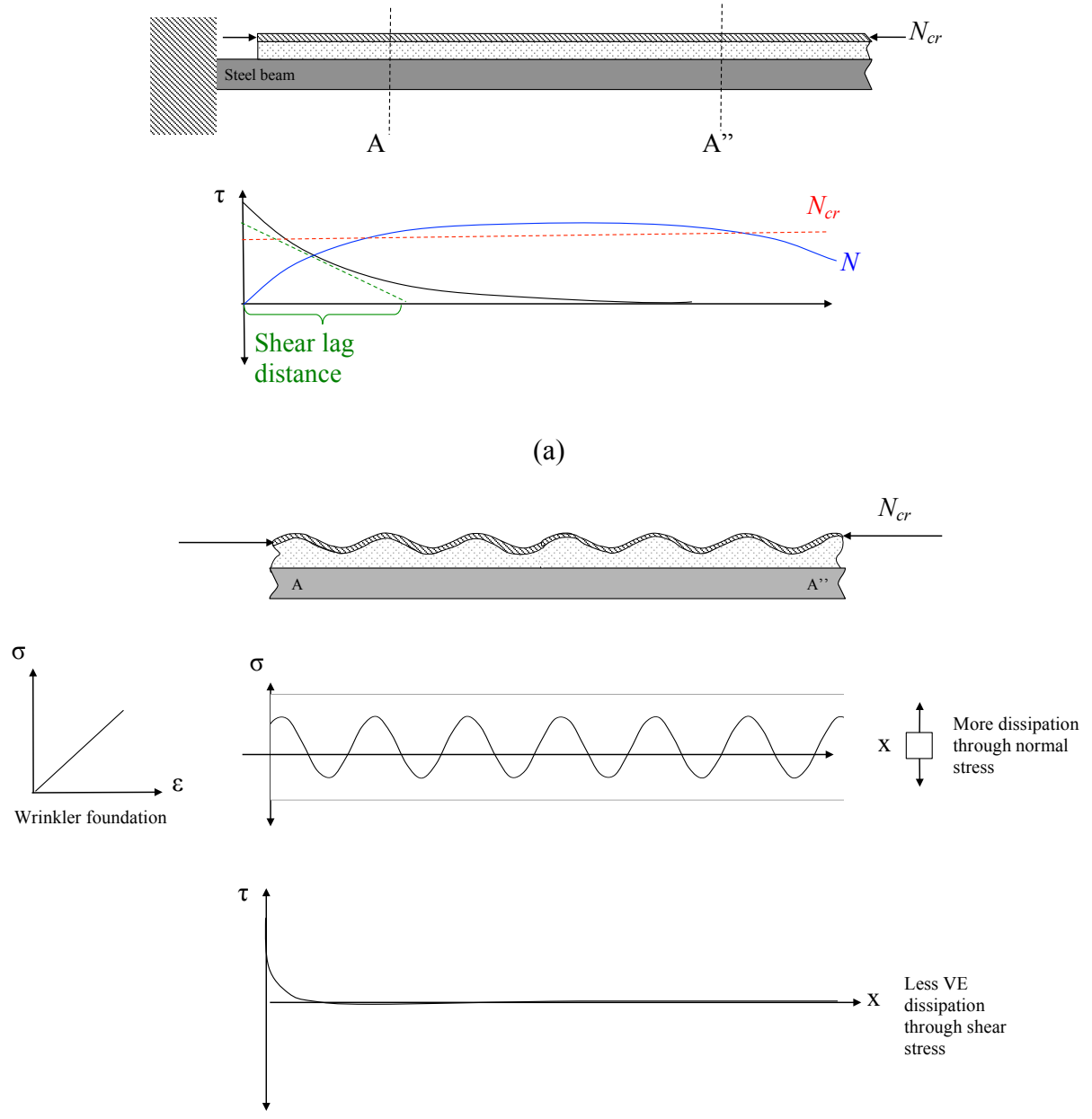

Figure 6.7: Diagram of the cantilever beam with damping tapes: a) shear stress distribution and normal load experienced by the constraining layer. b) shear and peel stress distribution along the damping layer.

Furthermore, it was experimentally observed that as the excitation amplitude increased and the axial load supported by the constraining layer gradually increased, the length where buckling may occur also increased; this is schematically shown in Figure 6.8.

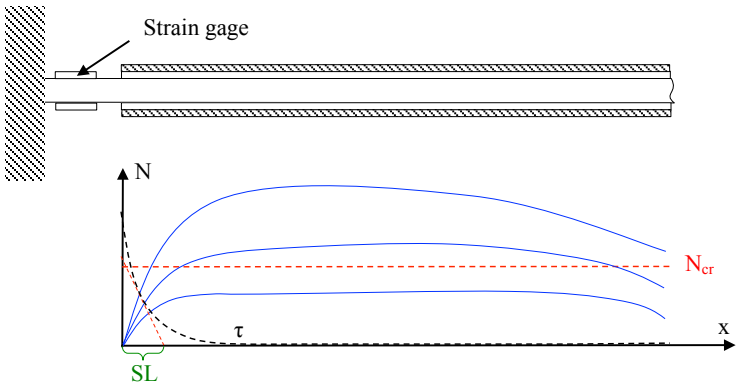

Figure 6.8: Schematic of increasing strain to a cantilever beam with damping tapes.

We extended the concept of "recovery length" (Curtin, 1991) to discretized-damping layers. Figure 6.9a shows a schematic illustration of such discretized damping layers with one cut, and Figure 6.9b shows the expected shear stress distribution, and the axial load to which the discretized constraining layer is subjected. Notice that discretizing a continuous layer into segments will reduce regions where axial load is above the critical buckling load thereby reducing the effective length where buckles are expected decreased. This may be caused by the increase in more lightly loaded ends with successive. This was confirmed through observation during experiments, and pictures were taken in order to illustrate the phenomena. Figure 6.10a shows the buckling of the backing material of the 3M 425 damping tape with a discretization length of 50 mm, this picture was taken when the beam was subjected to a strain amplitude higher than the critical buckling strain of 83 με. Figure 6.10b shows the buckling of the backing material of the 3M 425 damping tape with a discretization length of 25 mm, again this picture was taken when the beam was subjected to a strain amplitude higher than the critical buckling strain of 83 με.

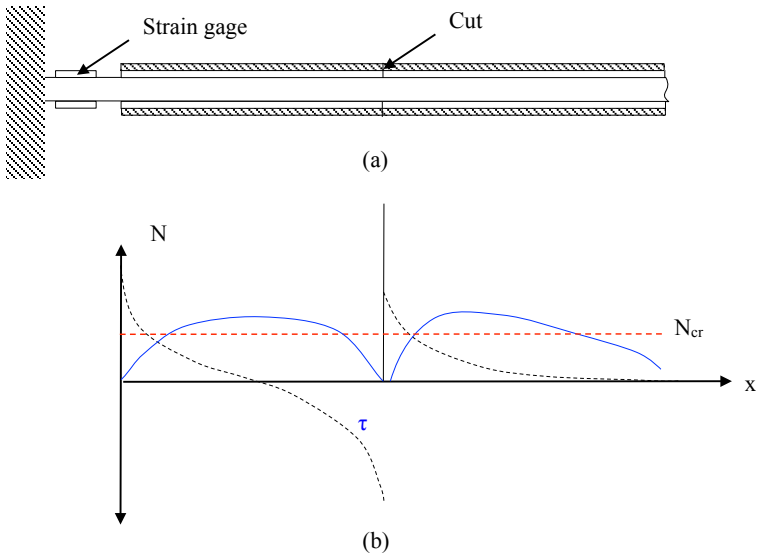

Figure 6.9: Schematic of experimental beam: a) discretized constrained damping layer with one cut. b) axial load and shear stress distribution for constrained damping layer with one cut.

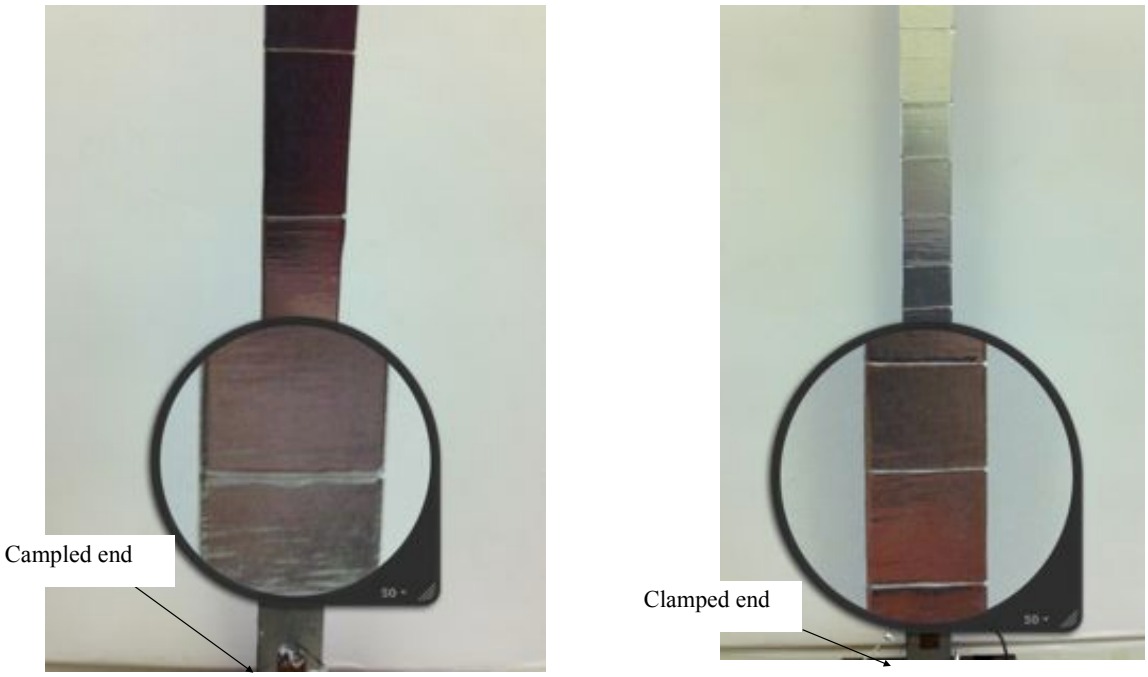

(a) (b)

Figure 6.10: Experimental visual results for: a) discretization length of 50 mm. b) discretization length of 25 mm.

Finally, Figure 6.11, shows the response amplitude vs. excitation amplitude for the different discretized damping tapes considered in this section. The critical buckling strain was determined to be 83 με. Notice the low value of the buckling strain compared to the strains measured during the experiments. This strain was experienced by the part of the beam near the clamped end and so, we may expect buckling there. Note that if plastically deformed buckles were present before the cuts were made, multiple effects could complicate this interpretation.

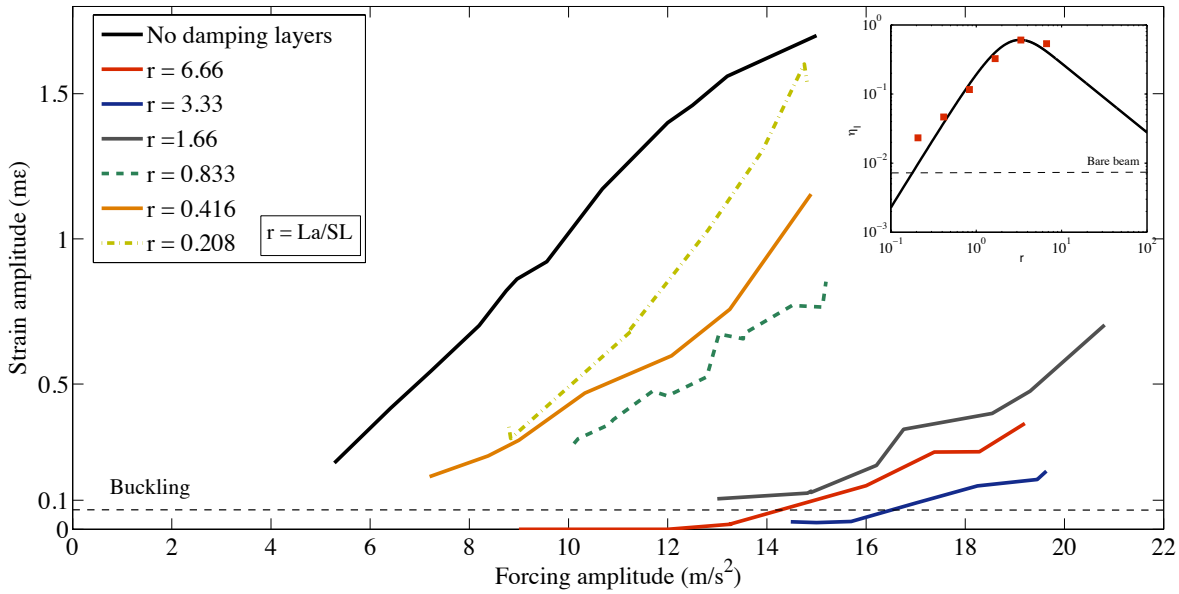

Figure 6.11: Forcing amplitude vs. response amplitude for different *r* using tape 3M 425.

6.3 Summary:

The buckling of the damping tape problem was addressed because of the relatively low values of strain needed to cause buckles within the backing layer of the considered damping layers. We obtained experimental data in Figure 6.3 for a continuous damping layer and different initial release amplitudes. These results showed up to a 28% permanent increase in the logarithmic decrement of the system after release from larger initial amplitudes. The inset showed in Figure 6.11 gives theoretical and experimental values of the loss coefficient of the beam for very small strains. Therefore, we did not expect an important difference between theoretical values found with the methods given in Chapter 3 and Chapter 4. Furthermore, we observed during forced vibration experiments that there was a characteristic length associated with the shear lag distance

where buckling of the backing layer was not expected but, as the loading during experiments increased, this length decreased allowing more buckling along the surface treatment as shown in Figure 6.8.

Discretized damping layers were also studied in this chapter. A decrease in the length of the buckling zone was observed when the segments of discretized damping layers were small. We concluded that this may be caused by an increase portion in the surface treatment acting as "recovery length", that we defined as a characteristics length of the damping layer needed to rebuild the stresses in a cut backing. The cuts then resulted in more lightly loaded ends as illustrated in Figure 6.9. Although we recognize that many experimental situations may complicate this interpretation, such as plastically deformed buckles before the new cuts were made, buckling appears to be a factor in damping tape behavior when sufficiently high strains are induced, suggesting the need for further study of this phenomenon.

Chapter 7 Conclusions

The purpose of this work was to investigate analytically and experimentally the effectiveness of discretized constrained damping layers. The viscoelastic material of damping tapes was characterized using a multiple layer quad shear specimen designed to enhance the shear deformation within the layers of the PSA tape following the methodology given by Yang et al. (Yang et al., 2007). The specimens were setup in the tensile film clamp of the DMA and a frequency sweep (0.1 Hz to 100 Hz) and temperature step (0 to 50 °C) were performed. The shear storage and loss modulus were calculated by analyzing the free body diagram of Figure 2.12 and the raw data of force and displacement recorded by the DMA results were obtained from equations (2.11). The values of tan δ were obtained directly from the DMA, and the master curves were constructed using the Time-Temperature Superposition Principle (TTSP) at a reference temperature of 20°C.

In Chapter 3 we introduced analytical tools to analyze the edge effect that causes an increased damping of the system within discretized damping layers. In this chapter we confirmed earliest results found by Plunkett and Lee (Plunkett & Lee, 1970). Following the methodology given by Plunkett and Lee it was showed theoretically, that discretized damping layers enhanced the energy dissipation compared to continuous damping layers when the segments length was near the optimal value but, as the length of the segments decreased from this optimal length, the ends effects became less important, resulting again in lower damping. The relation of this phenomenon to the shear lag distance from Volkersen's analysis was investigated and we confirmed that the optimal values of the length of segments were near 3.28 times the shear lag distance.

The experimental results from Chapter 4 confirmed the effectiveness of the discretized damping layer. Increased damping ratios were obtained when the discretization lengths were near the optimal value confirmed in this thesis. It was also experimentally observed that, as the

discretization length decreased from the optimal value for each damping tape, the damping decreased. Theoretical loss coefficients were also obtained from the Plunkett and Lee formulation (Plunkett & Lee, 1970). A comparison between experimental data and theoretical results were performed. A plateau of experimental data was observed in Figure 4.15 and Figure 4.16. We observed a relation of this plateau with the loss coefficient obtained for the bare beam. Also, the plateau might be related to a combined effect of air drag and structural damping during the motion of the beam. Additionally, in Chapter 3 we explained that, as the discretization length decreased, the capability of the constraining layer to induce shear deformation to viscoelastic layers decreased so the value of the plateau may be attributed to loss coefficient values of an unconstrained viscoelastic layer. Different behaviors of the plateau for different tapes and beams could be observed and the phenomenon could not be fully understood. We conclude that further investigation needs to be performed.

In Chapter 4, we also performed a theoretical analysis of partially covered cantilever beams. An enhancement of the damping ratio was found for several partially covered beams. We considered different damping layer lengths located near the clamped end of cantilever beams, where the strain is higher. The theoretical results showed that applying a surface treatment with length near the optimal value permit an increase of damping and decrease of added mass compared to continuous damping layers configuration. We consider that this is an alternative to overcome the added weight of thick damping tapes.

Chapter 5 introduced an analysis of structural elements with damping tapes undergoing large amplitude deflections. To this end, nonlinear resonance of a cantilever beam with damping tapes under parametric excitation was exploited. The objective was to study the effectiveness of such layers undergoing large amplitude conditions by comparing the time histories of the bare beam and the beam with the surface treatment. It was confirmed that viscoelastic layers successfully damped the amplitude of the response for the same amplitude of excitation. We also studied differences between nonlinear parameters of the undamped and damped beams. Identification of nonlinear parameters such as the nonlinear damping, cubic nonlinearity and the parametric forcing parameter for different discretization length was performed. We observed an increase in the nonlinear damping for the configurations near the optimal value of r that maximized the

linear damping. The cubic nonlinearities increased with the added layers and different *r* values compared to the bare beam. Additionally, we validated the identified nonlinear parameters by integrating the equation of motion for cantilever beams under parametric excitation near the first natural frequency of the beam.

Chapter 6 included an analysis of the effect of large deflection on the backing material of the damping tapes. We observed that as the amplitude of the response increased buckles near the clamped end of cantilever beams might appear introducing an additional energy dissipation mechanism. To further analyze this phenomenon, we performed free damped vibrations test realizing the tip of the beam at different amplitudes each time. We observed up to a 28% increase of the logarithmic decrement compared to those tests performed with small initial amplitude. A possible explanation of these results was that the onset of buckling and the upward expansion of the buckled regions with increasing tip displacement amplitude means larger affected areas of the constraining layers. Buckle patterns were evident after the tests, so permanent effects, perhaps due to the very low yield stresses of backing, may also affect the energy dissipation of the damping treatment.

We also observed less buckling as the damping layer was discretized. A possible explanation given was that each segment made to the surface treatment will discretize the shear stress distribution of the damping layer and therefore the axial load supported by the constraining layer. According to the analysis performed in this work, this results in more lightly axially loaded ends of damping tapes segments (Curtin, 1991), so less length of the surface treatment is available for buckling formation. The characteristic length at the ends of each surface treatment segment needed to build up stresses was defined as “recovery length”.

In conclusion, this work had analyze the dynamics of cantilever beams that allowed to confirmed the enhancement of the linear damping as the damping layers were discretized near the optimal value as define by Plunkett and Lee. Also, the amplitude of the beam under parametric excitation also decreased when discretizing the damping layer near this value. Therefore, this work has shown successfully the effectiveness of discretized-damping layers subjected to these two regimes.

7.1 Future work

Proposals for future improvements on the material characterization include the following:

1. Use refined standards to build the quad shear experiment to achieve a better bonding between the aluminum plates and the damping tape layers.
2. Test the quad shear sample at higher rates and lower temperatures to obtain complete master curves showing the transition zone for the adhesive.
3. Compare data obtained through the DMA tests performed with available data for the same damping tape, in order to show the accuracy of the method.

Future work in the field of the analytical model used to compared experimental and theoretical data include:

1. Develop accurate mode shapes for the beam with the damping layer and the discretized layer.
2. Develop finite element models of a cantilever beam with constrained damping layer to compare with experimental data.
3. Investigate carefully what causes the disagreement between theoretical and experimental values of the loss coefficient as the segments length is decreased.

The nonlinear study and the buckling investigation could be improved by:

1. Consider a more detailed analysis of the surface treatment as a thin layer over a soft substrate to obtain the critical buckling load.
2. Include surface analysis to accurately measure the size and frequency of the buckling zone.

References

3M. (2012a). 3M Metal Foil Tapes. In 3M (Ed.).

3M. (2012b). Damping tapes applications. 3M catalog.

Audoly, B., & Boudaoud, A. (2008). Buckling of a stiff film bound to a compliant substrate—Part I: Formulation, linear stability of cylindrical patterns, secondary bifurcations. *Journal of the Mechanics and Physics of Solids, 56*(7), 2401-2421.

Baker, W. E., Woolam, W. E., & Young, D. (1967). Air and internal damping of thin cantilever beams. *International Journal of Mechanical Sciences, 9*(11), 743-766.

Bordonaro, G. G. (2009). *Nonlinear System Identification of Physical Parameters for Damage Prognosis and Localization in Structures.* (PhD), Virginia Polytechnic Institute and State University.

Brinson, H. F., & Brinson, L. C. (2007). *Polymer engineering science and viscoelasticity*. New York: Springer.

Curtin, W. (1991). Fiber fragmentation in a single‐filament composite. *Applied physics letters, 58*(11), 1155-1157.

da Silva, L. F. M. (2011). *Handbook of adhesion technology*. Berlin: Springer.

Dillard, D. A. (2013). *Dynamic Behavior: Dynamic properties for steady state oscillatory behavior and viscoelastic damping.* Class Notes. Engineering Mechanics. Virginia Tech.

DiTaranto, R. (1965). Theory of vibratory bending for elastic and viscoelastic layered finite-length beams. *Journal of Applied Mechanics, 32*(4), 881-886.

Ferry, J. D. (1980). *Viscoelastic properties of polymers* (3rd ed.). New York: John Wiley & Sons.

Fung, J. (1998). *Parameter identification of nonlinear systems using perturbation methods and higher-order statistics.* (MS), Virginia Polytechnic Institute and State University.

Gere, J. M., & Goodno, B. J. (2009). *Mechanics of Materials.* . Independence, KY: Cengage Learning Inc.

Hajj, M., Miksad, R., & Powers, E. (1993). Fundamental–subharmonic interaction: effect of phase relation. *Journal of Fluid Mechanics, 256*, 403-426.

Hannah, R. L., & Reed, S. E. (1992). *Strain Gage Users' Handbook*. London: Springer.

Hetényi, M. (1971). *Beams on elastic foundation: theory with applications in the fields of civil and mechanical engineering*. Ann Arbor: University of Michigan Press.

Huang, R. (2005). Kinetic wrinkling of an elastic film on a viscoelastic substrate. *Journal of the Mechanics and Physics of Solids, 53*(1), 63-89.

Kerwin, E. M. (1959). Damping of Flexural Waves by a Constrained Viscoelastic Layer. *The Journal of the Acoustical Society of America, 31*(7), 952-962.

Lee, L. T. (1966). A graphical compilation of damping properties of both metallic and non-metallic materials. Wright-Patterson Air Force Base, Ohio: DTIC Document.

Malatkar, P. (2003). *Nonlinear vibrations of cantilever beams and plates.* (PhD), Virginia Polytechnic Institute and State University.

Mei, H., Huang, R., Chung, J. Y., Stafford, C. M., & Yu, H.-H. (2007). Buckling modes of elastic thin films on elastic substrates. *Applied physics letters, 90*(15), 151902.

Meirovitch, L. (2010). *Fundamentals of vibrations*. Boston: Waveland Press.

Micro-Measurements. (2010). Precision Strain Gages and Sensors. In V. P. Group (Ed.).

Micro-Measurements. (2011). Strain Gage Installation with M-Bond 200 Adhesive.

National-Instruments. (2006). Strain Gage Configuration Types.

Nayfeh, A. H. (1985). Parametric identification of nonlinear dynamic systems. *Computers & structures, 20*(1), 487-493.

Nayfeh, A. H., & Mook, D. T. (2008). *Nonlinear oscillations*. Weinheim: John Wiley & Sons.

Parfitt, G. (1962). *The effect of cuts in damping tapes.* Paper presented at the 4th ICA Congress, Kopenhagen, Paper P.

Parfitt, G., & Lambeth, D. (1960). The Damping of Structural Vibrations (P. Department, Trans.): Ministry of Aviation.

Plunkett, R., & Lee, C. T. (1970). Length Optimization for Constrained Viscoelastic Layer Damping. *The Journal of the Acoustical Society of America, 48*(1B), 150-161.

Sato, K., Saito, H., & Otomi, K. (1978). The parametric response of a horizontal beam carrying a concentrated mass under gravity. *Journal of Applied Mechanics, 45*(3), 643-648.

Sperling, L. H. (2005). *Introduction to Physical Polymer Science*. New York: John Wiley & Sons.

TA-Instruments. (2010). TA Instruments Thermal Analysis. In T. Instruments (Ed.).

Thomson, W. (1996). *Theory of Vibration with Applications*. Cheltenham: CRC Press.

Ungar, E. (2000). Damping by viscoelastic layers. *Applied Mechanics Reviews, 53*(6), R33-R38.

Ungar, E., Ross, D., & Kerwin, E. (1960). *Damping of flexural vibrations by alternate visco-elastic and elastic layers*: Wright Air Development Center, Air Research and Development Command, U. S. Air Force.

Vella, D., Bico, J., Boudaoud, A., Roman, B., & Reis, P. M. (2009). The macroscopic delamination of thin films from elastic substrates. *Proceedings of the National Academy of Sciences, 106*(27), 10901-10906.

Volkersen, O. (1938). Die Nietkraftverteilung in zugbeanspruchten Nietverbindungen mit konstanten Laschenquerschnitten. *Luftfahrtforschung, 15*(1/2), 41-47.

Winkler, E. (1872). *Vorträge über Eisenbahnbau*. Prague: Universität Giessen.

Yang, H., Zhang, W., Moffitt, R. D., Ward, T. C., & Dillard, D. A. (2007). Multi-layer in-situ for evaluation of dynamic mechanical properties of pressure sensitive adhesives. *International Journal of Adhesion and Adhesives, 27*(7), 536-546.

Zavodney, L., & Nayfeh, A. (1989). The non-linear response of a slender beam carrying a lumped mass to a principal parametric excitation: theory and experiment. *International Journal of Non-Linear Mechanics, 24*(2), 105-125.